# FABRICATION OF NANO-LAMINATED SOFT MAGNETIC METALLIC ALLOYS THROUGH MULTILAYER ELECTRODEPOSITION: APPLICATION TO HIGH-FREQUENCY AND HIGH-FLUX POWER CONVERSION

A Dissertation
Presented to
The Academic Faculty

by

Jooncheol Kim

In Partial Fulfillment
of the Requirements for the Degree
Doctor of Philosophy in the
School of Electrical and Computer Engineering

Georgia Institute of Technology
August 2015

# FABRICATION OF NANO-LAMINATED SOFT MAGNETIC METALLIC ALLOYS THROUGH MULTILAYER ELECTRODEPOSITION: APPLICATION TO HIGH-FREQUENCY AND HIGH-FLUX POWER CONVERSION

Approved by:


Dr. Mark G. Allen, Advisor
School of Electrical and Computer Engineering
*Georgia Institute of Technology*

Dr. Andrew F. Peterson
School of Electrical and Computer Engineering
*Georgia Institute of Technology*

Dr. Farrokh Ayazi
School of Electrical and Computer Engineering
*Georgia Institute of Technology*

Dr. Todd Sulchek
School of Mechanical Engineering
*Georgia Institute of Technology*

Dr. Maryam Saeedifard
School of Electrical and Computer Engineering
*Georgia Institute of Technology*


Date Approved: [July, 20, 2015]

*To my family, who I love.*

# ACKNOWLEDGEMENTS

Upon finishing the thesis, I would like to thank many people who have supported me.

First of all, I would like to express my sincere gratitude to my advisor, Dr. Mark G. Allen, for his strong support and guidance throughout my Ph.D. journey. His abundant knowledge and wisdom drove me to overcome many research obstacles and to become a professional researcher.

I would like to thank Dr. Farrokh Ayazi and Dr. Maryam Saeedifard for serving as thesis reading committee members. I would also like to thank Dr. Andrew F. Peterson and Dr. Todd Sulchek for serving on my thesis committee. I appreciate their advice and suggestions on my research.

I would like to thank all members in the MicroSensors and MicroActuators (MSMA) group at the Georgia Institute of Technology and University of Pennsylvania for their support, discussion, and friendship. Richard Shafer gave me a lot of technical support as a laboratory manager. His attitude on the experiments inspired me whenever I was losing my motivation for the research. I would like to thank Minsoo Kim for his valuable discussions and support. As my mentor and friend, he helped me to settle down into the microfabrication world from the beginning to the end of this Ph.D study. It was great to spend most of my Ph.D. time working with him. I would also like to thank Dr. Florian Herrault for this mentorship to successfully finish the ARPA-E project, and Seong-Hyok Kim and Seung-Joon Paik for their support and guidance to join this group. Although I cannot list them all one by one, I would like express my sincere appreciation to all MSMA members.

I would like to thank ARPA-E project members including Dr. Jeffery Lang and David Otten in MIT for their help for high-power converter test.

I would like to thank all of my friends in the Georgia Institute of Technology. Special thanks to Hypen_Nine (a group of my closest friends) and Dok-do United (a Korean student soccer club) for encouraging me whenever I felt alone.

Finally, I would like to express my deepest appreciation to my parents and two brothers for their endless support, sacrifice, prayer and love.

# TABLE OF CONTENTS


Page

ACKNOWLEDGEMENTS iv

LIST OF TABLES x

LIST OF FIGURES xi

LIST OF SYMBOLS AND ABBREVIATIONS xvi

SUMMARY xvii

CHAPTER

1 INTRODUCTION 1

1.1 Introduction 1

1.2 Background Theories 1

1.2.1 Switched-Mode DC-DC Converter 3

1.2.2 Inductor 6

1.2.3 Magnetic Core 8

1.2.4 Magnetic Core Losses 10

1.3 Research Objective 12

1.4 Contributions of This Research 16

1.4.1 Fabrication of Highly-Ordered, Nanoengineered Material 16

1.4.2 Reliable Characterization of Highly-Laminated Nano Structures 17

1.4.3 Ultracompact DC-DC Power Conversion using Nanolaminated Metallic Alloy 17

2 LITERATURE REVIEW 18

2.1 Soft Magnetic Materials 18

2.1.1 Screen Printed Ferrites 19

2.1.2 Electrodeposited Metallic Alloys 20

2.1.3 Sputtered Nanogranular Films 22

2.2 Microfabricated Inductors 23

2.2.1 Spiral Inductors 24
2.2.2 Strip-Line Inductors 25
2.2.3 Solenoid Inductors 25
2.2.4 Toroid Inductors 26
2.3 DC-DC Converters with Integrated Magnetics 27
2.3.1 DC-DC Converters with Integrated Magnetics – using Ferrite Cores 27
2.3.2 DC-DC Converters with Integrated Magnetics – using Thin Film Cores 30
2.3.3 DC-DC Converters with Integrated Magnetics – using Metallic Alloy Cores 31
2.3.4 Commercial DC-DC Converter Modules 32
2.4 Advantages and Challenges of Integrated Magnetics 33
3 NANOLAMINATED MAGNETIC METALLIC ALLOY CORES 34
3.1 Introduction 34
3.2 Permalloy and CoNiFe Thin Films 35
3.2.1 Electrodeposition of Permalloy and CoNiFe Thin Films 35
3.2.2 Properties of Permalloy and CoNiFe Thin Films 36
3.2.3 Comparing Properties of Permalloy and CoNiFe Thin Films 38
3.3 Sequential Electrodeposition for Multilayer Magnetic Structures 39
3.4 Fabrication of Nanolaminated Magnetic Cores 42
3.4.1 SU-8 Support Approach 43
3.4.2 Surface-Tension-Driven Assembly 45
3.4.3 Comparison of Two Fabrication Techniques 53
3.5 Characterization of Nanolaminated Magnetic Cores 53
3.5.1 Low Flux Characterization 56
3.5.2 High Flux, High Frequency Characterization 60
3.5.3 Decomposition of Magnetic Losses 65
3.5.4 System Level Characterization 77
3.6 Anisotropic Nanolaminated CoNiFe Core 83

3.6.1 Fabrication of Anisotropic Nanolaminated CoNiFe Cores 83

3.6.2 Characterization of Anisotropic Nanolaminated CoNiFe Cores 85

3.7 Conclusion 89

4 MICROFABRICATED INDUCTORS INTEGRATED WITH NANOLAMINATED MAGNETIC CORES 91

4.1 Introduction 91

4.2 Microfabricated Inductors using Core Drop-in Approach 92

4.2.1 Fabrication Process of Core Drop-in Approach 93

4.2.2 Characterization of Toroid Microfabricated Inductors 98

4.2.3 Solenoid Microfabricated Inductors using Core Drop-in Approach 105

4.3 Microfabricated Inductors using Direct Electrodeposited Winding Approach 107

4.3.1 Fabrication Process of Direct Electrodeposited Winding Approach 107

4.3.2 Characterization of Solenoid Microfabricated Inductors 109

4.4 Comparison of State-of-Art Microfabricated Inductors 110

4.5 Performance of Microfabricated Inductors in High Power DC-DC Converter 112

4.5.1 Power Converter Topology 112

4.5.2 Microfabricated Inductors Tested in Power Converter 114

4.6 Conclusion 117

5 ULTRACOMPACT DC-DC BUCK CONVERTER WITH NANOLAMINATED MAGNETIC CORES 119

5.1 Introduction 119

5.2 Design of Ultracompact DC-DC Converter 119

5.3 Development of Ultracompact DC-DC Converter 122

5.3.1 Nanolaminated CoNiFe Core Inductor Preparation 122

5.3.2 Fabrication of Ultracompact Converter on PCB 123

5.4 Characterization of Ultracompact DC-DC Converter 124

5.5 Comparison of Ultracompact DC-DC Converter with Other Converters 129

6 CONCLUSION 135

6.1 Summary of Conducted Research 135

6.2 Suggestions for Future Research 137

6.2.1 Applications Where the Nanolaminated Magnetic Core is Most Suitable 137

6.2.2 More Geometries of Core and Inductor 139

6.2.3 Improved Magnetic Material 140

6.2.4 Surface-Tension-Driven Assembly 141

6.2.5 Magnetic Domain Characterization 142

6.2.6 Correlation between Each Characterization Stages 142

6.2.7 Other Applications using Nanolaminated Metallic Alloys 143

REFERENCES 144

# LIST OF TABLES


Page

Table 2.1: Soft magnetic materials used as inductor core 18

Table 2.2: Review of DC-DC converters with integrated magnetics 27

Table 2.3: Commercial DC-DC buck converter modules with integrated inductors 33

Table 3.1: Electrodeposition conditions for permalloy and CoNiFe 35

Table 3.2: Properties and composition of electrodeposited CoNiFe 37

Table 3.3: Properties of water and Novec 1700 at 23°C 51

Table 3.4: SU-8 support approach and surface-tension-driven assembly 53

Table 3.5: Properties of commercial ferrites 77

Table 3.6: Comparison of nanolaminated permalloy and CoNiFe cores 82

Table 4.1: Comparison of temporary and permanent core embedding approaches 97

Table 4.2: Parameters of integrated inductor with nanolaminated cores 99

Table 4.3: Summary of microfabricated inductors with nanolaminated CoNiFe cores 110

Table 5.1: Converter specification 120

Table 5.2: Comparison of inductors with nanolaminated CoNiFe core 123

Table 5.3: Components utilized for ultracompact DC-DC buck converter 123

Table 5.4: Comparison of converter power loss with estimated core loss 128

Table 5.5: Properties of the ultracompact DC-DC converter 129

Table 5.6: Performance of DC-DC converters with integrated magnetics 130

Table 6.1: Applications where DC-DC converter is used 138

# LIST OF FIGURES

Page

Figure 1.1: Schematics of a typical DC-DC buck converter 3

Figure 1.2: DC-DC buck converter waveforms in steady-state operation 5

Figure 1.3: Schematic of an N-turn inductor 6

Figure 1.4: Hysteresis loop of soft magnetic materials 9

Figure 1.5: Comparison of eddy current flow in non-laminated core and laminated core 14

Figure 1.6: Overview of thesis structure 15

Figure 2.1: Typical feature of microfabricated inductor with ferrites 19

Figure 2.2: Laminated NiFe core 21

Figure 2.3: Cross-section of laminated nanogranular film 22

Figure 2.4: Racetrack-shaped microfabricated inductor 24

Figure 2.5: Schematic of a typical V-groove inductor 25

Figure 2.6: Schematic of typical microfabricated inductors with magnetic cores 26

Figure 2.7: A prototype DC-DC converter having a spiral inductor with ferrite core as a substrate 28

Figure 2.8: Integrated DC-DC converter 29

Figure 2.9: DC-DC converter with LTCC inductor substrate 30

Figure 2.10: Monolithic DC-DC converter using thin film inductor 30

Figure 2.11: DC-DC converter using microfabricated inductors with electrodeposited permalloy cores 31

Figure 2.12: Integration of inductor and IC in commercial DC-DC converter modules 33

Figure 3.1: Saturation flux density and coercivity of 1-µm-thick CoNiFe film as a function of deposition current density. 37

Figure 3.2: Measured B-H hysteresis curves 38

Figure 3.3: Schematic of automated sequential electrodeposition system 40

Figure 3.4: Saturation flux density and coercivity of CoNiFe/copper multilayer as a function of number of laminations 41

Figure 3.5: Surface topology of electrodeposited CoNiFe films 42

Figure 3.6: Fabrication of nanolaminated magnetic core using SU-8 support approach 43

Figure 3.7: Images of nanolaminated magnetic cores fabricated through SU-8 support approach 45

Figure 3.8: Fabrication sequence for surface-tension-driven assembly of nanosheet 46

Figure 3.9: Images of nanolaminated CoNiFe cores fabricated through surface-tension-driven assembly 48

Figure 3.10: Schematic of two parallel laminations possessing liquid in between them 49

Figure 3.11: Measured contact angle of DI water and Novec 1700 polymer droplets on CoNiFe film 50

Figure 3.12: Assembly of CoNiFe sheets in a given length of 15 mm 51

Figure 3.13: Assembly percentage with varying number of CoNiFe laminations in a 15 mm space 52

Figure 3.14: Test inductors 54

Figure 3.15: In situ characterization of nanolaminated magnetic cores 57

Figure 3.16: Characterization of test inductors with nanolaminated CoNiFe cores with varying number of laminations 59

Figure 3.17: Schematic of the HFHF core loss characterization setup 61

Figure 3.18: Measured power loss per unit volume at high peak flux densities at low MHz frequency 63

Figure 3.19: Volumetric power losses of a nanolaminated permalloy and CoNiFe cores at 1 MHz as a function of flux density 65

Figure 3.20: Schematic of analytically modeled magnetic lamination 66

Figure 3.21: Measured power loss per unit volume over operation frequency up to 0.5 T flux density 75

Figure 3.22: Comparison of eddy-current loss with hysteresis loss at 1 MHz as a function of flux density 76

Figure 3.23: Image of a DC-DC converter evaluation board with a 36-turn inductor with nanolaminated magnetic core 78

Figure 3.24: Comparison of commercial inductor and a nanolaminated core with penny 78

Figure 3.25: Converter efficiency and switching frequency as a function of output power 79

Figure 3.26: Comparison of power converter performance tested with a nanolaminated permalloy core inductor and a nanolaminated CoNiFe core inductor 80

Figure 3.27: Schematic of in-field sequential electrodeposition system 84

Figure 3.28: Images of anisotropic nanolaminated CoNiFe cores and test inductors 84

Figure 3.29: Measured inductance of test inductors and ratio of effective permeabilities of nanolaminated CoNiFe cores 86

Figure 3.30: Total volumetric power losses of nanolaminated CoNiFe cores at 1 MHz as a function of peak flux density 87

Figure 3.31: Converter evaluation board with replaced resistor and test inductor 88

Figure 3.32: Experimental results of DC-DC converter performance tested with an anisotropic, nanolaminated CoNiFe core inductor 89

Figure 4.1: Conceptual approach for microfabricated inductor with drop-in core 92

Figure 4.2: Drop-in cores 94

Figure 4.3: Core integration approaches 94

Figure 4.4: Optical images of fabricated additional layers 96

Figure 4.5: Microfabricated toroidal inductors integrated with nanolaminated CoNiFe cores 98

Figure 4.6: Characterization of 50-turn-integrated inductors with nanolaminated magnetic cores as well as an air core inductor by means of temporary core embedding approach 103

Figure 4.7: Characterization of 30-turn-integrated inductors with nanolaminated magnetic cores as well as an air core inductor by means of permanent core embedding approach 105

Figure 4.8: 10-turn microfabricated solenoid inductor with an anisotropic nanolaminated CoNiFe core 106

Figure 4.9: Characterization of a microfabricated solenoid inductor with nanolaminated CoNiFe core 106

Figure 4.10: Fabrication sequence of microfabricated solenoid inductor with laminated CoNiFe core 108

Figure 4.11: Optical images of a microfabricated solenoid inductor with laminated CoNiFe core 109

Figure 4.12: Measured inductance quality factor of a 9-turn solenoid inductor with a CoNiFe core comprising 2000 layers of 1-µm-laminations 109

Figure 4.13: Comparison of microinductors with electroplated magnetic cores 111

Figure 4.14: A merged two-stage conversion architecture having a switched capacitor first stage that provides voltage pre-regulation and transformation, and a high-frequency magnetic stage that provides fine regulation of the output 112

Figure 4.15: Schematic of the switched-capacitor pre-regulator/transformation stage with bootstrap diodes 113

Figure 4.16: Schematic of the second magnetic-based regulation stage designed to operate at high frequency 114

Figure 4.17: Image of converter circuit board integrated with a microfabricated inductor 114

Figure 4.18: Experimental measurements of 50-turn toroidal inductor tested in power converter 115

Figure 4.19: Experimental measurements of 10-turn solenoid inductor tested in power converter 116

Figure 4.20: Experimental measurements of 9-turn solenoid inductor tested in power converter 117

Figure 5.1: DC-DC buck converter schematic diagram 119

Figure 5.2: Schematic diagram of the converter circuit simulated with LTspice 121

Figure 5.3: Simulation result from the circuit diagram in Figure 5.2 121

Figure 5.4: Inductance and quality factor 122

Figure 5.5: Images of ultracompact DC-DC converter 124

Figure 5.6: Captured waveforms from the oscilloscope 125

Figure 5.7: Measured efficiency and switching frequency as a function of input voltage 125

Figure 5.8: Output power versus inductance density of DC-DC converter with integrated magnetics 131

Figure 5.9: Converter efficiency versus switching frequency of DC-DC converter with integrated magnetics 133

# LIST OF SYMBOLS AND ABBREVIATIONS

| | |
|---|---|
| $B_s$ | Saturation Flux Density |
| $H_c$ | Magnetic Coercivity |
| $L$ | Inductance |
| $Q$ | Quality Factor |
| $C$ | Capacitance |
| $R_{core}$ | Magnetic Core Loss |
| $R_{cu}$ | Copper Loss in Inductor Windings |
| $R_{cap}$ | Capacitor Loss |
| $P_{V,tot}$ | Volumetric Power Loss of Core |
| $P_{V,eddy}$ | Volumetric Eddy-Current Losses |
| $P_{V,hyst}$ | Volumetric Hysteresis Losses |
| $k_{eddy}$ | Eddy-Current Loss Density Coefficient |
| $k_{hyst}$ | Hysteresis Loss Density Coefficient |
| $\delta$ | Skin Depth |
| $a$ | Lamination Thickness |
| $\omega$ | Angular Frequency |
| $\sigma$ | Conductivity |
| $\rho$ | Resistivity |
| $\mu_r$ | Relative Permeability |
| $N$ | Number of Inductor Turns |

# SUMMARY

The objective of this proposed research is to design, fabricate, characterize and test nanolaminated soft magnetic metallic alloy cores that operate at high frequency (> 1 MHz) and high flux (> 0.1 T) for high power (> 10W) ultracompact DC-DC power conversion. Driven by the demand for multi-functional and smaller portable electronic devices, DC-DC converter miniaturization is of great interest. Examination of such converters shows that the physical size of magnetic components is typically the limiting factor in miniaturization. In order to reduce the physical size of these magnetic components, both increases in switching frequency as well as improvements in the performance of magnetic materials at these frequencies can be attempted. Soft magnetic metallic alloys such as NiFe and CoNiFe possess superior magnetic properties (i.e., higher saturation flux density and lower coercivity) than the conventional ferrites that are typically used in these applications. However, the high conductivity and corresponding eddy-current losses at high operating frequencies limit the ultimate useful thickness of such metallic alloys to their skin depth (~ 3 μm at 10 MHz), which may not be sufficient for high power handling (> 10 W).

In order to simultaneously achieve both high power handling and suppressed eddy-current losses, development of nanolaminated cores comprising alternating layers of sufficiently thin magnetic material and insulating material is required. This structure prevents electrical connection between the magnetic layers, thereby suppressing the formation of eddy currents. Sufficient thickness for higher power application can then be achieved by stacking multiple magnetic and insulating layers to form nanolaminated magnetic cores.

In this research, in order to realize such nanolaminated magnetic cores for high frequency and high power conversion, the following key tasks have been accomplished: 1) electrodeposition of metallic alloy materials such as NiFe, CoNiFe, and anisotropic CoNiFe; 2) development of new fabrication technologies to realize nanolaminated cores based on metallic alloy electrodeposition; 3) reliable characterization of the structural, magnetic, and electrical properties of the nanolaminated metallic alloy cores; 4) development of microfabricated inductor windings to integrate the nanolaminated cores; 5) demonstration of high-frequency and high-flux ultracompact DC-DC power conversion using inductors integrated with nanolaminated metallic alloy cores.

By achieving these tasks, nanolaminated cores comprising tens to hundreds of layers of metallic alloy films ($Ni_{80}Fe_{20}$ and $Co_{44}Ni_{37}Fe_{19}$) has been developed. The fabricated nanolaminated core consists of sufficiently thin nanolaminations (100 – 1000 nm) that can suppress eddy currents in the MHz range, while simultaneously achieving the overall magnetic thickness (35 – 2000 μm) such that substantial power can be handled. The nanolaminated metallic alloy cores were further integrated into microfabricated inductors using CMOS-compatible fabrication processes. Finally, an ultracompact DC-DC buck converter with the nanolaminated metallic alloy cores has been developed on PCB having footprint of 14 × 7.1 $mm^2$. The input voltage of the converter varied from 30 to 70 V and the output voltage was fixed at 20 V. The converter operated with output power of approximately 11 W and the switching frequencies of 0.7 – 1.4 MHz, demonstrating conversion efficiency of 94.2% at 30 V input and 80.8% at 60 V input.

# CHAPTER 1

# INTRODUCTION

## 1.1 Introduction

The ever-increasing demand for multifunctional and smaller portable electronic devices is driving the development of miniaturized DC-DC converters [1 - 3]. Such converters are utilized to shift voltage levels in electronic systems with high efficiency. There are multiple applications for such converters. For example, state-of-the-art portable smart phones and tablet PCs feature multiple components, such as the display panel, MEMS sensors, data storage devices, and cameras, which may require different operating voltage levels. Miniaturizing these converters reduces the overall size of the portable devices. Hence, there have been increasing efforts to shift from conventional power supply manufacturing, which typically assembles discrete power supply modules and components, toward integrated DC-DC power supplies, namely power supplies in package (PSiP) and power supplies on chip (PSoC), using semiconductor and microfabrication technologies.

## 1.2 Background Theory

Modern portable electronic devices including smart phones and tablet PCs, are becoming smaller but at the same time having more functions that require development of efficient DC-DC converters. As an efficiency alternative to a linear regulator, where the difference between the input and output voltage is continuously dissipated as wasted energy, switched-mode DC-DC converters are of great interest. Switched-mode DC-DC converters typically comprise active semiconductor devices (e.g., power MOSFETS and controllers) and passive components (e.g., inductors, capacitors and resistors) for voltage

regulation [4, 5]. The active semiconductor device operates as a switch by being on/off (e.g., saturation/cutoff for a BJT or MOSFET) to maintain an average output voltage, resulting in high conversion efficiency.

In general, there are two types of switched-mode DC-DC converters: 1) switched-capacitive converters; and 2) switched-inductive converters. The switched-capacitive converter, also known as inductorless converter or charge pump, operates without magnetic components (i.e., inductors). Instead, it transfers power from the supply to the load by charging and discharging capacitors. The absence of the magnetic component can enable easy monolithic integration and minimized EMI (electromagnetic interference); however, it suffers from inherent power losses and large numbers of switches that result in lower power density and lower efficiency. Applications of the switched-mode DC-DC converter include use in RS-232 data signals that require both positive and negative voltages for logic levels, and in flash memory circuits where relatively high voltages are needed to erase stored information [4].

In contrast, the switched-inductive converter uses inductors as an energy storage component to transfer power from the input to the load, usually resulting in high conversion efficiency. Switched-inductive converters are the dominant DC-DC converters in modern portable devices, especially when the power density and efficiency are critical [5, 6]. Typically, the inductor occupies the largest volume of the converter and is often integrated with magnetic material to increase its inductance density. Hence, there have been increasing efforts to develop advanced yet compact inductors and magnetic cores for DC-DC converter miniaturization.

In the following sub-chapters, basic theories of the switched-mode inductive DC-DC converter, inductor, and magnetic material are presented.

### 1.2.1 Switched-Mode DC-DC Converter

Figure 1.1 shows a circuit diagram of a typical switched-mode DC-DC buck converter. When switch *S*1 closes (and *S*2 opens), current flows through the inductor and into the load, charging the inductor by increasing its magnetic field and increasing $V_{out}$. When $V_{out}$ reaches the desired value, *S*1 opens and *S*2 closes. Current continues to flow in the inductor as the magnetic field decreases and the inductor discharges. Before the current in the inductor falls to zero, *S*2 opens and *S*1 closes and the cycle is repeated. The ratio of $V_{out}$ to $V_{in}$ is adjusted by controlling the duty cycle (*D*) of *S*1 (i.e., the converter duty cycle). If the switches, inductor, and other components are ideal (i.e., lossless), the conversion efficiency is 100%. In reality, there are several types of losses including switching loss, conduction loss, and magnetic loss, that prevent attainment of ideality.

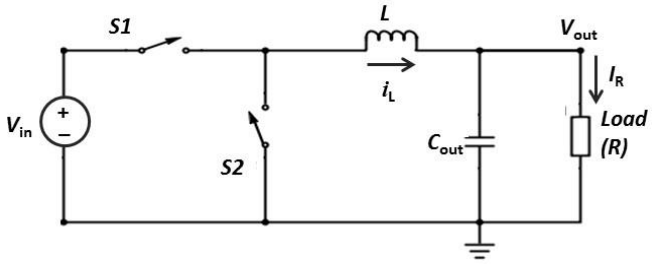


(a)

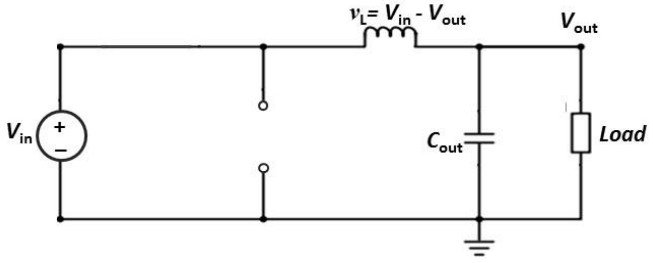


(b)

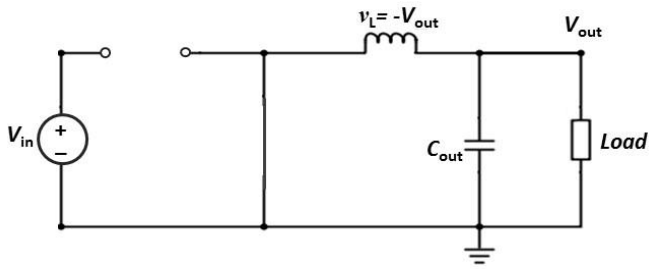


(c)

Figure 1.1 (a) Schematic of a typical DC-DC buck converter. (b) Equivalent circuit for *S*1 closed. (c) Equivalent circuit for *S*1 open.

In steady-state operation, the switching period is *T*; therefore, *S*1 is closed for time *DT* and open for time *(1-D)T*. When *S*1 is closed as shown in Figure 1.1 (b), the voltage across the inductor becomes:

$$v_L = V_{in} - V_{out} = L\frac{di_L}{dt} \tag{1.1}$$

The derivative of the inductor current is a positive constant, meaning that the inductor current increases linearly when *S*1 is closed. When *S*1 is open as shown in Figure 1.1 (c), the voltage across the inductor becomes:

$$v_L = -V_{out} = L\frac{di_L}{dt} \tag{1.2}$$

In this case, the derivative of the inductor current is a negative constant, meaning that the inductor current decreases linearly when *S*1 is open. Typical inductor voltage and current waveforms are illustrated in Figure 1.2. For steady-state operation, the net inductor voltage in a switching period (*T*) must be zero, which can be expressed as:

$$\langle v_L \rangle_T = \frac{1}{T}\int_0^{DT} v_L dt + \frac{1}{T}\int_{DT}^{T} v_L dt = 0 \tag{1.3}$$

Combining with equations (1.1) and (1.2), this becomes:

$$\mathrm{D}(V_{in} - V_{out}) + (1-D)(-V_{out}) = 0 \tag{1.4}$$

Therefore, the ratio of the output voltage to the input voltage is the same as the duty ratio:

$$\frac{V_{out}}{V_{in}} = D \tag{1.5}$$

The duty ratio of the switch is set by a feedback loop that compares the output voltage to a reference voltage.

The DC component of the inductor current ($I_L$) is the same as the output current at the load ($I_R$), since the DC component of the current through the output capacitor must be zero:

$$I_L = I_R = \frac{V_{out}}{R} \tag{1.6}$$

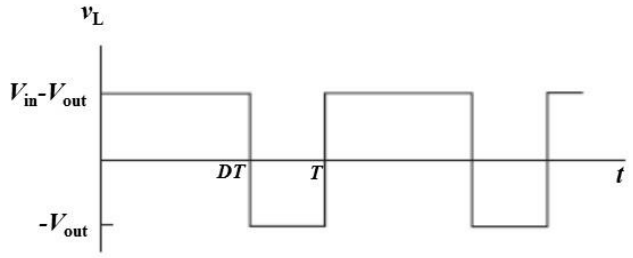


(a)

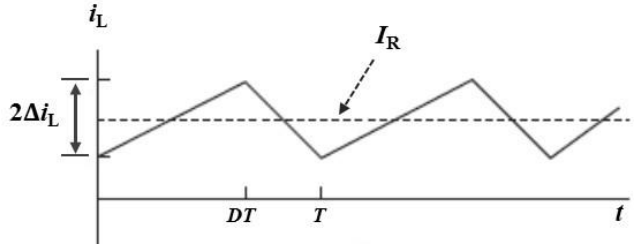


(b)

Figure 1. 2 DC-DC buck converter waveforms in steady-state operation. (a) Inductor voltage, and (b) inductor current.

From the inductor current waveform shown in Figure 1.2 (b), the slope of the increasing current when *S*1 is closed can be expressed as:

$$slope = \frac{di_L}{dt} = \frac{2\Delta i_L}{DT} \tag{1.7}$$

Combing with equation (1.1), this becomes:

$$\frac{2\Delta i_L}{DT} = \frac{V_{in}-V_{out}}{L} \tag{1.8}$$

Therefore, the ripple current ($\Delta i_L$) flowing in the inductor is expressed as:

$$\Delta i_L = \frac{(V_{in}-V_{out})\cdot D}{2\cdot L\cdot f_{sw}} \tag{1.9}$$

Also, the required inductance for a DC-DC buck converter is:

$$L = \frac{(V_{in}-V_{out})\cdot D}{2\cdot \Delta i_L\cdot f_{sw}} \tag{1.10}$$

where $f_{sw}$ is the switching frequency ($1/T$), indicating that the required inductance decreases with increasing switching frequency.

### 1.2.2 Inductor

Currently, the passive elements (e.g., inductors and transformers) are the largest elements in the switching converters and challenging to integrate, thereby impeding the realization of monolithic solutions for power conversion systems. Increasing converter switching frequency results in physical size reduction of passive components, since the required values (i.e., inductance and capacitance) of such components are inversely proportional to the switching frequency [7]. An inductor is a circuit element that consists of a conducting wire and a core (e.g., air-core or magnetic core) as shown in Figure 1.3.

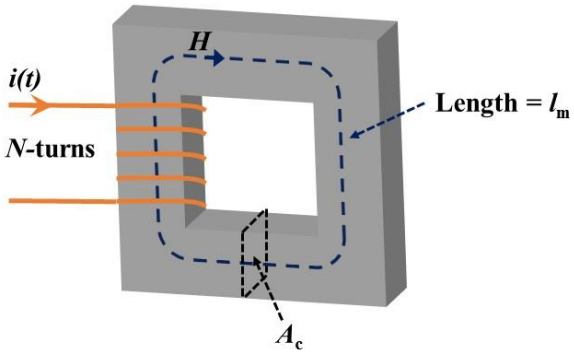


Figure 1.3 Schematic of an N-turn inductor.

When a current flows in a one turn winding, the induced magnetic field in the closed path, *C*, is expressed by Ampere`s law:

$$\oint_C H(t) \cdot dl = I(t) \tag{1.11}$$

where *H(t)*is the magnetic field strength [A/m], *dl* is the differential element of the curve *C*, and *I(t)* is the total current [A] passing through the winding. For a uniform magnetic field and *N*-turn winding,

$$H(t) \cdot l_m = Ni(t) \tag{1.12}$$

where $l_m$ is the magnetic path length [m].

When a time-varying magnetic flux passes through a conductive path, the relation between the induced voltage and the flux follows Faraday`s law:

$$v(t) = \frac{d\Phi(t)}{dt} = A_c \frac{dB(t)}{dt} \tag{1.13}$$

where *Φ(t)* is the magnetic flux passing through the loop [Wb], *v(t)* is the voltage induced by the flux, *B(t)* is the magnetic flux density [T] and $A_c$ is the enclosed cross-sectional area of the conductive path [$m^2$]. For a winding of N turns,

$$v(t) = N\frac{d\Phi(t)}{dt} = NA_c \frac{dB(t)}{dt} \tag{1.14}$$

The relationship between magnetic flux and magnetic field strength is expressed by the constitutive relationship for the material through which the flux flows. For a linear magnetic material, this can be expressed as:

$$B(t) = \mu H(t) \tag{1.15}$$

where $\mu$ is the permeability of the magnetic material, which is further expressed as:

$$\mu = \mu_0 \mu_r \tag{1.16}$$

where $\mu_0$ is the permeability of vacuum, $4\pi \times 10^{-7}$ [H/m], and $\mu_r$ is the relative permeability of the material (e.g., $\mu_r = 1$ for air).

Combining equations (1.14) and (1.15) yields:

$$v(t) = \mu N A_c \frac{dH(t)}{dt} \tag{1.17}$$

Combining with equation (1.12):

$$v(t) = \frac{\mu N^2 A_c}{l_m} \frac{di(t)}{dt} = L \frac{di(t)}{dt} \tag{1.18}$$

Therefore, the inductance $L$ is expressed as:

$$L = \frac{\mu N^2 A_c}{l_m} = \frac{N^2}{\frac{l_m}{\mu A_c}} = \frac{N^2}{\Re} \tag{1.19}$$

where $\mathrm{R}$ is the reluctance of the magnetic core material [$H^{-1}$]. For an inductor with magnetic core and air-gap, the formula to calculate the inductance is:

$$L = \frac{N^2}{R_{mag} + R_{air-gap}} = \frac{N^2}{\frac{l_m}{\mu_r \mu_0 A_c} + \frac{l_g}{\mu_0 A_c}} \tag{1.20}$$

where $\mu_r$ is the relative permeability of magnetic core material, and $l_m$ and $l_g$ are the length of magnetic path and air-gap, respectively [m].

### 1.2.3 Magnetic Core

Although use of magnetic cores enables inductor miniaturization (because the relative permeability exceeding unity allows a particular inductance to be achieved in a smaller geometric volume), such use can result in frequency-dependent core losses (e.g., hysteresis and eddy-current losses) as well as magnetic saturation, that limits the power handling capacity and efficiency of the converters [8, 9]. A hysteresis loop (Figure 1.4) is often used to understand the magnetic properties of soft magnetic materials. The soft magnetic materials represent magnetic materials that are easily magnetized and demagnetized with low coercivity. The hysteresis loop is a closed double-valued

magnetization curve caused by the energy loss in the magnetic material due to magnetization in every cycle.

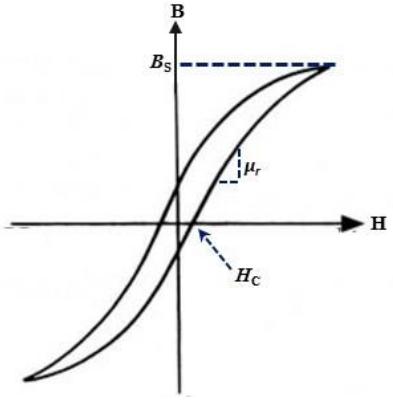


Figure 1.4 Hysteresis loop of soft magnetic materials.

In the hysteresis loop of magnetic materials, important intrinsic magnetic properties for inductor core materials include saturation flux density ($B_s$), coercivity ($H_c$), and relative permeability ($\mu_r$).

For typical toroid-shape inductive components, the maximum energy that can be stored in a closed magnetic field is expressed as:

$$E = \frac{1}{2}Li^2 = \frac{1}{2}L\left(\frac{N\Phi}{L}\right)^2 = \frac{1}{2}\cdot\frac{\Phi^2}{\mu}\cdot\frac{l}{A} = \frac{1}{2}\frac{B_S^2}{\mu}\cdot A\cdot l \tag{1.21}$$

where $i$ is the applied current [A], $\Phi$ is the peak magnetic flux [Wb], $B_s$ is the saturation flux density [T], $\mu$ is the permeability [H/m], $N$ is the number of winding turns, and $l$ and $A$ are the average circumference and cross-sectional area of the toroid [m and $m^2$]. Thus, the ultimate achievable energy density from a magnetic core becomes [9]:

$$E_d = \frac{1}{2}\cdot\frac{B_S^2}{\mu} \tag{1.22}$$

Consequently, the ultimate achievable power from a magnetic core at a given frequency can be estimated as:

$$P_{\text{core}} = E_{\text{d}} \cdot V_{\text{core}} \cdot f = \frac{B_S^2 \cdot V_{\text{core}} \cdot f}{2 \cdot \mu} \tag{1.23}$$

where $V_{\text{core}}$ is the volume of the magnetic core [$m^3$], and $f$ is the operation frequency [Hz]. Therefore, high saturation flux density is critical for such inductor cores to preserve required power in a reduced device dimension, improving the ultimate achievable miniaturization of inductive components.

From equations (1.19) and (1.22), it should be noted that the inductance is proportional to the relative permeability ($\mu_{\text{r}}$) of the magnetic core, while the energy density is inversely proportional to the relative permeability. Hence, reducing $\mu_{\text{r}}$ of the magnetic core generally allows a higher energy density, while the inductance becomes smaller. Alternatively, increasing $\mu_{\text{r}}$ of the magnetic core can achieve a higher inductance, but with a lower energy density. It is worth noting that effective ways to increase the energy density while maintaining high relative permeability (and therefore high inductance per unit volume) are increasing the saturation flux density ($B_{\text{s}}$) and/or increasing the thickness of the magnetic core [2].

### 1.2.4 Magnetic Core Losses

Magnetic core losses of inductors are important for high efficiency DC-DC power conversion, and there have been a large number of studies analyzing these losses. The detailed analysis of magnetic loss is discussed in chapter 3.3.3; a brief introduction is provided here. Magnetic core losses are induced when the magnetic material is exposed to an external magnetic field. Typically in the literature, the magnetic core losses are separated into (at least) two categories: 1) hysteresis losses and 2) eddy-current losses.

The hysteresis loss is the energy consumed to change the alignment direction of magnetic domains. Magnetic domains are the portions of a magnetic material that are

magnetized in the same direction. The hysteresis loss refers to the area enclosed by the static hysteresis loop shown in Figure 1. 4, and the volumetric magnetic hysteresis energy loss can be expressed as [9, 10]:

$$P_{\mathrm{V,hyst}} = \oint_{one-cycle} HdB \tag{1.24}$$

Such loops are typically measured at low frequency, and the loop area can become larger as the frequency increases. Thus, there can be changes in effective coercivity and permeability as frequency increases. However, assuming that the shape of the hysteresis loop throughout the entire frequency range of interest is invariable, the volumetric magnetic hysteresis loss at the operation flux density and frequency can be estimated as [10]:

$$P_{\mathrm{V,hyst}} = f * \oint HdB \tag{1.25}$$

where the cyclic integral is taken around the B-H loop and *f* is the frequency at which the loop is traversed. Therefore, desirable characteristics of magnetic metallic alloys for use as an inductor core should include a low coercivity to minimize the magnetic hysteresis losses.

Eddy current losses are induced by time-varying magnetic flux existing inside the magnetic core. This time-varying flux generates voltage differences within sections of the core. If the magnetic core material is also electrically conducting, eddy currents arise within the material from these voltage differences due to Ohm's law. These eddy currents oppose the changing magnetic field, resulting in deterioration of the magnetic properties. Further, the eddy current can generate tremendous heat through the Joule effect, resulting in difficulties in designing the magnetic core.

The power loss arising from the eddy current is given by:

$$P_e = i_e^2(t)R = \frac{v_e^2(t)}{R} \tag{1.26}$$

The induced voltage $v_e(t)$ is proportional to the derivative of the flux density:

$$v_e(t) = A_c \frac{dB(t)}{dt} \tag{1.27}$$

The magnitude of the induced voltage is proportional to the excitation of frequency *f*. Therefore, the eddy current loss is proportional to $f^2$, which would become a serious problem in high frequency. In order to suppress the eddy-current flow, thickness of the magnetic material needs to be less than the skin depth ($\delta$) of the material:

$$\delta = \sqrt{\frac{1}{\pi\mu\sigma f}} \tag{1.28}$$

where $\sigma$ is the conductivity of the magnetic material [S/m]. Thus, as the converter switching frequency increases, the skin depth of the material decreases. Typically, the skin depth of soft magnetic material (e.g., NiFe) is approximately 3 μm at 10 MHz, a reasonable upper bound in operation frequency for today's switching converters [11].

### 1.3 Research Objectives

In summary, desirable characteristics of magnetic materials for use as an inductor core for DC-DC power conversion include: 1) high saturation flux density to allow high power density operation of devices; 2) low coercivity to minimize intrinsic magnetic hysteresis losses; 3) appropriate relative permeability to improve inductance density; 4) minimized eddy-current losses at high frequency operation; 5) fabrication simplicity and integration availability with ICs.

Currently, ferrite cores are often used for high frequency operation, due to their high resistivity (> 1e9 μΩ·cm), resulting in large skin depths and therefore low eddy-current losses. However, their low saturation flux density (< 0.3 T) limits operating flux

levels and therefore the ultimate achievable degree of miniaturization. Also, the high sintering temperature (> 900°C) utilized during the typical ferrite manufacturing process is not CMOS-compatible.

Magnetic metallic alloys, such as permalloy ($Ni_{80}Fe_{20}$) and CoNiFe, that are deposited using CMOS-compatible processes (e.g., sputtering and electrodeposition) have been widely researched due to their superior magnetic performance (i.e., high saturation flux density and low coercivity) over conventional ferrites. However, their high conductivity and corresponding small skin depth and large eddy-current losses have typically limited their useful thickness to a few microns (~ 3 μm) at high frequency (~ 10 MHz), which is not sufficient for high power handling (> 10W).

In order to simultaneously achieve both large magnetic volume and suppressed eddy-current losses for metallic alloys, *lamination* is a promising solution. Laminated cores are structured alternating layers of sufficiently thin magnetic material (e.g., less than the skin depth of the material) to suppress eddy currents, and insulating material that prevents interlayer electrical current flow that would otherwise allow the eddy currents to re-establish, resulting in an overall core magnetic thickness that is sufficient for high power handling. Figure 1.5 compares the eddy current flow in a laminated core where the single lamination thickness (*a*) is less than the skin depth and a non-laminated core where the core thickness exceeds the skin depth. Although the lamination technique is widely utilized in low frequency, macro-scale applications (e.g., line power transformers) by simply stacking alternating magnetic sheets and insulating layers, it is challenging to realize such laminated structures in the submicron scale for high frequency (> 1 MHz) operation. Sputtering can be used to develop laminated cores comprising tens of layers of thin (< 200 nm)

laminations, due to its capability to deposit both magnetic materials (e.g., CoZrO [12] and CoFe [13]) and high resistivity insulating material (e.g., $SiO_2$); but its relatively slow deposition rate and internal stress restrict the total achievable core thickness. Typically, the total magnetic thickness of the sputtered core is less than 10 µm [12, 14].

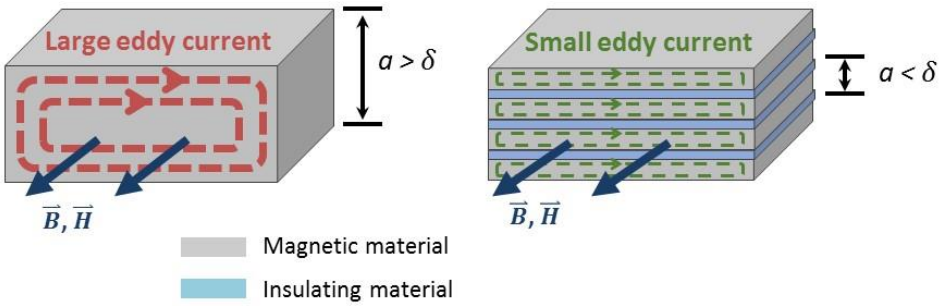


Figure 1.5 Comparison of eddy current flow in non-laminated core and laminated core.

The objective of this research is to develop nanolaminated magnetic metallic alloy cores based on sequential electrodeposition. In the proposed nanolaminated metallic alloy cores, sufficiently thin nanolaminations (100 - 1000 nm) can suppress eddy currents in the MHz range, while the overall magnetic thickness (35 - 2000 µm) enables substantial power handling. This approach, which exploits the superior magnetic properties of metallic alloys while suppressing eddy currents through the use of nanolaminations, is expected to satisfy the aforementioned requirements for DC-DC converter inductor cores. To realize miniaturized power inductors, the nanolaminated cores are integrated with low resistance microfabricated windings. Finally, the microinductors with nanolaminated cores are utilized for ultracompact, high frequency (> 1 MHz) and high power (> 10 W) DC-DC power conversion.

Figure 1.6 shows an overview of this thesis structure ranging from nanolaminated magnetic core fabrication through microfabricated inductor development to DC-DC converter demonstration.

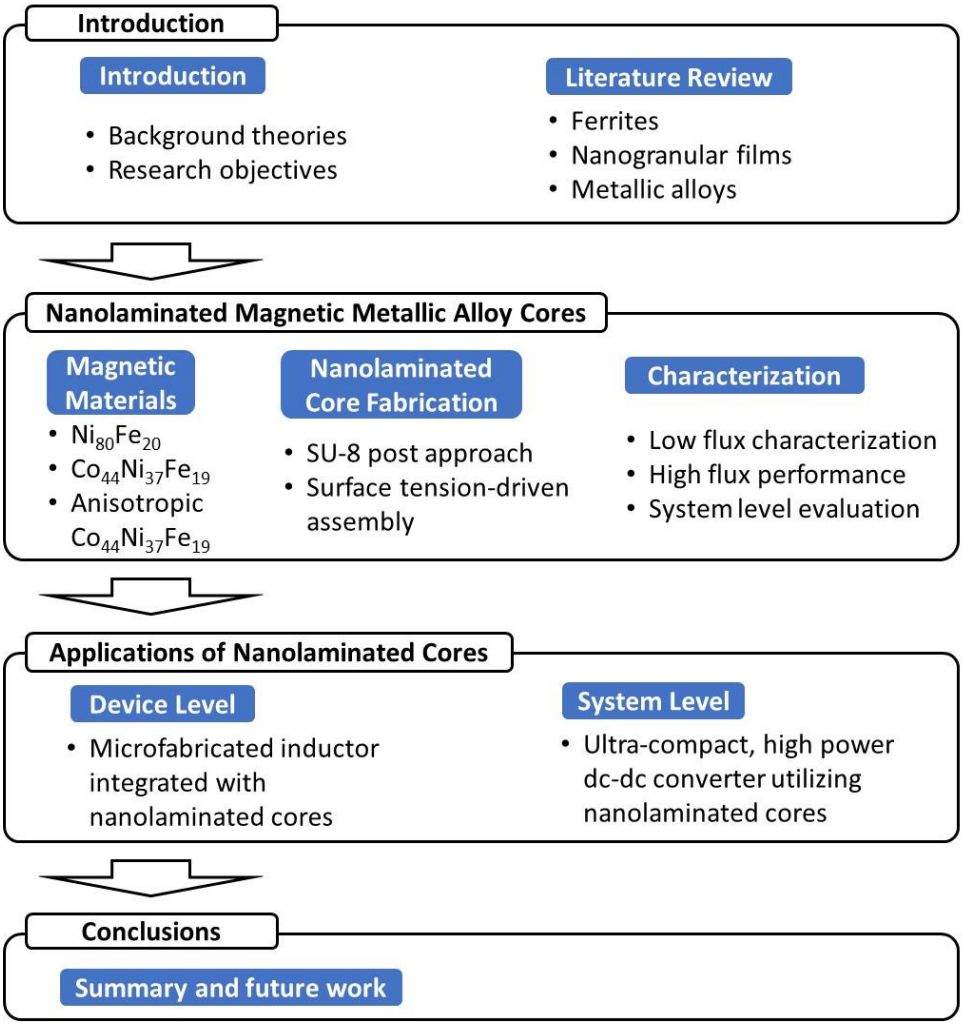


Figure 1.6 Overview of thesis structure.

Chapter 1 and 2 present background theories, a motivation for this research, and literature survey from related fields. Chapter 3 presents fabrication and characterization of nanolaminated magnetic cores. Electrodeposition of permalloy ($Ni_{80}Fe_{20}$), $Co_{44}Ni_{37}Fe_{19}$, and anisotropic $Co_{44}Ni_{37}Fe_{19}$ thin films was studied and nanolaminated magnetic cores comprising tens to hundreds of insulated magnetic stacks with single layer thicknesses less than 500 nm were fabricated based on an SU-8 post approach as well as a new approach, surface-tension-driven assembly. For the characterization of the nanolaminated magnetic

cores, three types of characterizations (low flux characterization, high flux characterization, and system level characterization) were performed. Chapter 4 presents fabrication and characterization of microfabricated inductors integrated with the nanolaminated magnetic cores. Two microfabrication techniques (core drop-in approach and direct winding approach) were developed for realization of the inductors with the nanolaminated magnetic cores. Using the microinductors and the nanolaminated magnetic cores, ultracompact DC-DC converters that operate at high switching frequency (> 1 MHz) and high output power (> 10 W) were designed and developed on PCB (printed circuit board) with other commercial components (e.g., switch, capacitors and resistors) in chapter 5. Finally, chapter 6 concludes this thesis.

## 1.4 Contributions of This Research

The proposed research is expected to have three main contributions: 1) fabrication of highly-ordered, nanoengineered materials, 2) reliable characterization of highly-laminated magnetic nanostructures, and 3) ultracompact DC-DC power conversion utilizing inductors based on nanolaminated metallic alloys.

### 1.4.1 Fabrication of Highly-Ordered, Nanoengineered Material

The fabrication techniques described in this research demonstrate bulk volumes of nanoengineered material that consists of highly-stacked alternating metallic alloys and insulating layers with single layer thicknesses in the nano range. The fabricated material enables utilization of the superior magnetic properties of metallic alloys (e.g., high saturation flux density and low coercivity) as well as suppression of eddy-current flows in nano sheets. This fabrication technique is expected to be applicable for further applications in areas where bulk, nanoengineered materials are of interest including anisotropic thermal conductors and high surface area capacitors.

### 1.4.2 Reliable Characterization of Highly-Laminated Nano Structures

During the research, it is found that reliable characterization of the laminated structures comprising large number of layers with nano-scale single layer thickness is very critical since it is challenging to visualize the nano-laminations without damaging the structures. The characterization methods introduced in this research range from low flux *in situ* characterization through high flux characterization to system level evaluation, and will provide methodical and effective characterization approaches for materials comprising large numbers of nanolaminations.

### 1.4.3 Ultracompact DC-DC Power Conversion using Nanolaminated Metallic Alloys

The demonstration of ultracompact DC-DC converters using nanolaminated metallic alloy cores allows the ultimate verification of the nanolaminated core performance as an energy conversion material. Further, this demonstration will provide a guideline for more advanced CMOS-compatible integration techniques for power supplies on chip (PSoC) and power supplies in package (PSiP).

# CHAPTER 2

# LITERATURE REVIEW

## 2.1 Soft Magnetic Materials

Soft magnetic materials (e.g., ferrites, magnetic powders, and metallic alloys) are widely used and researched for electrical energy storage/transfer elements in switched power conversion [11 - 30]. Since the early 1990s, these magnetic materials have been used as integral parts of micro-magnetic devices for integration into passive components, such as inductors and transformers. Table 2.1 summarizes the typical characteristics of magnetic materials for use in inductor cores. Note that commercial ferrites are also included. These magnetic materials can be categorized by deposition method into: 1) screen printed ferrite; 2) sputtered thin film (i.e., nanogranular film); and 3) electrodeposited metallic alloy.

Table 2.1 Soft magnetic materials used as inductor core (×: not used, o: used)

| Deposition Method | Material | Bs [T] | Hc [Oe] | $\mu_r$ | $\rho$ [μΩ·cm] | Lami-nation |
|---|---|---|---|---|---|---|
| Screen printing | NiZnCuFe [15] | 0.23 | 17.5 | 25 | 1e8 | × |
| | NiZnCuFe [15] | 0.46 | 4.1 | 120 | 1e8 | × |
| | MnZnFe [16] | 0.25 | 40 | 6 | 3e8 | × |
| | NiZnCu [17] | 0.22 | 42.8 | 28 | 1e8 | × |
| | 4f1 [18] | 0.32 | 2 | 80 | 1e6 | × |
| | 67 TOTOID [19] | 0.23 | 3.5 | 40 | 1e6 | × |
| Sputtering | CoZrO [12] | 1.3 | 1 | 80 | 600 | o |
| | CoZrTa [20, 21] | 1.52 | 0.4 | 300 | 100 | × |
| | CoFeSiO [22, 23] | 1.1 | N/A | 250 | 100 | o |
| | CoFe [13] | 1 | N/A | 200 | 2200 | o |
| | $Ni_{80}Fe_{20}$ [14, 24] | 1 | 1 | 1000 | 20 | o |
| Electro-deposition | $Ni_{80}Fe_{20}$ [25, 26] | 0.8 | 3 | 2000 | 20 | × |
| | $Ni_{45}Fe_{55}$ [27] | 1.5 | 0.5 | 150 | 45 | × |
| | CoFeCu [28] | 1.46 | 2.8 | 400 | 30 | × |
| | NiFeMo [29] | 1.07 | 0.1 | 2200 | N/A | × |
| | CoNiFe [30] | 2.2 | 10 | 250 | 30 | × |

### 2.1.1 Screen Printed Ferrites

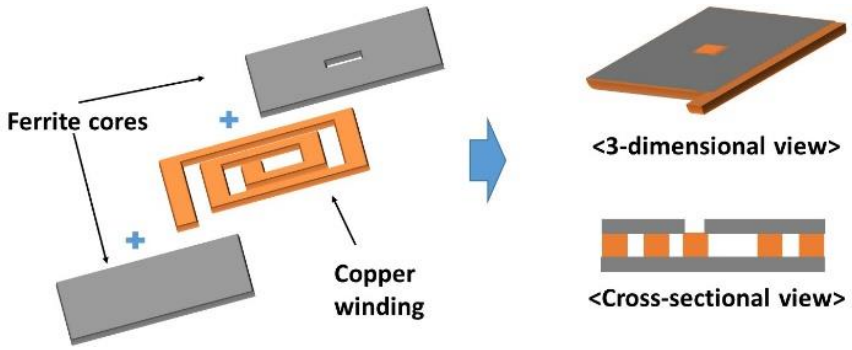


Figure 2.1 Typical feature of microfabricated inductor with ferrites.

Screen printing is an ideal deposition method for non-metallic ferrite cores including NiZn, MnZn, and their composites. Since 1993 [31], ferrites have been researched for high frequency power electronic applications due to their inherent low electrical conductivity, resulting in negligible eddy current losses at high frequency (i.e., over 1 MHz). Generally, microfabricated inductors with ferrite cores feature a spiral winding geometry surrounded by layers of ferrite material with thickness from a few microns to millimeters as illustrated in Figure 2.1. For example, a planar inductor with NiZnCu ferrite core was developed with a size of $5 \times 5$ mm$^2$ on silicon wafer in 2009 [17]. NiZnCu ferrite was fabricated by high temperature sintering at 800 °C and 4.5-turn spiral windings were sandwiched between 1-μm-thick NiZnCu ferrite plates. Due to the high resistivity of the ferrite core, the inductor exhibited a quality factor of 50 at 2.3 MHz and 20 at 10 MHz. Ferrites are also the most widely used magnetic material with discrete windings in the commercial market for surface mountable power inductors operating at the high frequency range [18, 19]. However, there are still two major challenges for this material to be further miniaturized and integrated to the chip scale: 1) high sintering temperature, which prevents monolithic integration of the material into power-chip

circuitry; and 2) relatively low magnetic saturation flux density, resulting in low energy density device.

### 2.1.2 Electrodeposited Metallic Alloys

Electrodeposition and sputtering are attractive deposition techniques for the development of magnetic components due to their CMOS-compatibility, batch-fabrication, and ease of precise patterning via photo-lithography, enabling the possible realization of PSiP (power supply in package) and PSoC (power supply on chip) for miniaturized and integrated dc-dc converter systems [2].

Electrodeposition has been widely used to deposit binary or ternary metallic alloys with various compositions exhibiting saturation flux density higher than 1 T and coercivity lower than 2 Oe as shown in Table 2.1. An alloy of 80%-nickel and 20%-iron has been utilized as a classical recording head since the beginning of magnetic recording in the mid 1930s [32]. Later, in the 1990s, nickel-iron alloys with different compositions were developed and researched as an inductor core material [33] due to their low coercivity, high saturation flux density and permeability, and nearly zero-magnetostriction (i.e., unchanged magnetic properties by induced mechanical strain). These nickel-iron alloys are either permalloy ($Ni_{\sim 80}Fe_{\sim 20}$) or orthonol ($Ni_{\sim 50}Fe_{\sim 50}$) thin films, and exhibit saturation flux density of 0.9 - 1.4 T and coercivity of 1 - 2 Oe. In order to improve the magnetic properties, several soft magnetic materials have been researched and developed by exploiting other metallic components including cobalt, copper and molybdenum. J.W. Park *et al*. [28] electrodeposited thin film alloys of cobalt, iron, and copper that achieved a saturation flux density of approximately 1.5 T. Taylor *et al*. [29] electrodeposited a thin film alloy of nickel, iron, and molybdenum that demonstrated a low coercivity of 0.3 Oe and a high

permeability of 2200. In 1998, Osaka *et al*. introduced electrodeposition of CoNiFe films [34] that simultaneously exhibit high saturation flux density (~ 2 T) and low coercivity (< 2 Oe). Since then, this CoNiFe material has been widely studied due to its superior magnetic properties [35, 36]. It has been also attempted to utilize the CoNiFe material in power electronics applications [30].

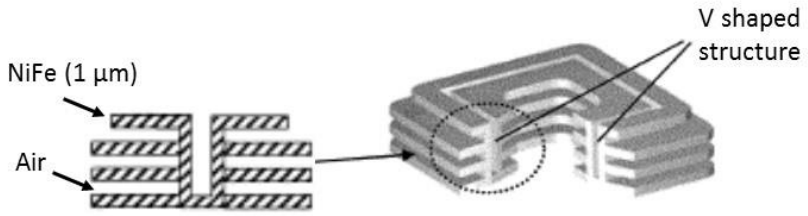


Figure 2.2 Laminated NiFe core [11].

In spite of their outstanding magnetic properties (i.e., high saturation flux density and low coercivity) and CMOS-compatible fabrication, the high conductivity of metallic alloys can cause eddy-current losses during high frequency operation (> 1MHz), limiting the achievable overall core thickness for high power handling. Thus, there have been many attempts to realize laminated magnetic cores based on electrodeposition [11, 37]. However, since electrodeposition is typically performed with low resistivity (e.g., less than 50 μΩ·cm) materials, it is challenging to realize highly-laminated structures (i.e., alternating layers of metallic alloy and insulating film). In 2003, J.Y. Park *et al.* [11] fabricated a laminated NiFe core based on manual sequential electrodeposition of NiFe films (Figure 2.2) for reducing eddy currents in the MHz operating regime while simultaneously preserving large total magnetic cross-sectional area. However, the labor-intensive approach impedes reliable fabrication of laminated cores with a large number of layers and precisely controlled sub-micron single layer thickness.

### 2.1.3 Sputtered Nanogranular Films

Recently, researchers have developed nanogranular magnetic alloys using sputtering to achieve both high saturation flux density and high resistivity for high frequency operation [12 - 14, 20 - 24]. These sputtered nanogranular films include CoZrTa, CoFe, and CoZrO. Due to the advantage of depositing a wide range of materials including $SiO_2$, the nanogranular films are often deposited with oxide layers as a multilayer as shown in Figure 2.3 [22].

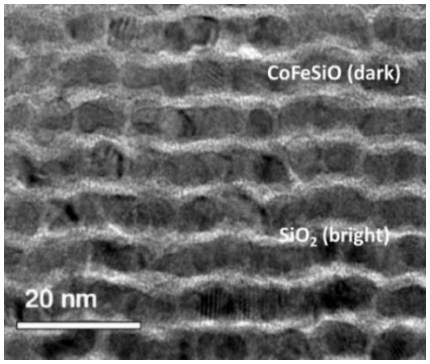


Figure 2.3 Cross-section of laminated nanogranular film (CoFeSiO-6nm / $SiO_2$-1nm) [22].

The high resistivity and uniform film thickness in the nano-range enables these nanogranular films to be utilized up to GHz frequency range. In 2002, a multilayer nanogranular magnetic thin film for GHz operation was fabricated using inductively coupled RF sputtering [13]. With a single layer thickness of 6 nm, the multilayer structure exhibited a constant permeability of 200 and a high resistivity of 2.2 mΩ·cm at up to 2 GHz. In 2009, Gardner *et al*. developed an on-chip inductor integrated into a 90 nm CMOS process using copper metallization and a nanogranular CoZrTa magnetic material [21]. The integrated magnetic material exhibited a saturation flux density of 1.52 T and resistivity of 100 μΩ·cm. The fabricated inductor showed a high inductance density of 1700 nH/mm$^2$ and quality factor of 8 at 40 MHz. In 2013, microfabricated V-groove inductors with

multilayer CoZrO film were fabricated for very high frequency operation [12]. The sputtered magnetic CoZrO exhibited a saturation flux density of 1.3 T and resistivity of 600 μΩ·cm. The fabricated inductor showed a high quality factor that exceeded 50 at 100 MHz.

The sputtering process for nanogranular film deposition requires a vacuum environment and is relatively slower than other deposition methods (e.g., electrodeposition), resulting in a long deposition time and high fabrication cost. Also, the induced internal stress during the multilayer deposition may cause mechanical stability issues [38]. Therefore, these nanogranular films are not been widely at overall core thicknesses beyond tens of micrometers; yet, significant overall thickness (> 30 μm) is required for high power (> 10 W) handling capability.

### 2.2 Microfabricated Inductors

In combination with advanced magnetic core materials that can operate in high frequency regimes, current-carrying windings are required to realize inductive components. Advanced chip-scale inductors have been developed based on microfabrication technology for the realization of PSiP and PSoC. The microfabricated inductors can be categorized into two winding approaches depending on the arrangement of windings with respect to the magnetic cores: 1) 2-dimensional winding where planar conductor coils are surrounded by magnetic cores; and 2) 3-dimensional winding where planar cores are wrapped by conductor coils. Typical structures using the first winding approach are spiral inductors and strip-line inductors. Structures using the second winding approach include toroid and solenoid inductors. In most cases, the conductor coil is fabricated by electrodeposition of copper though a lithographically-patterned photoresist.

### 2.2.1 Spiral Inductors

The spiral type structure is one of the most widely used winding schemes, mainly due to its high inductance density and fabrication simplicity. Typically, either circular or rectangular copper windings are surrounded by magnetic cores to improve inductance density and to minimize EMI as shown in Figure 2.1. Also, a racetrack-shaped spiral inductor has been studied to improve the high frequency performance of microfabricated inductors [27, 39]. The racetrack-shaped inductor is formed by stretching a circular spiral winding. In 2007, Wang *et al*. developed a racetrack-shaped inductor with an inductance density and peak quality factor of 38 nH/mm$^2$ and 5, respectively [39]. The inductor was fabricated by electrodeposition of $Ni_{45}Fe_{55}$ magnetic core to wrap the elongated portion of the electrodeposited copper winding so as to take advantage of the uniaxial anisotropy of the magnetic material as shown in Figure 2.4. The insulating layers were also added between windings and cores as well as between the inductor and silicon substrate.

In order to further improve the performance of spiral microfabricated inductors, it becomes important to increase the aspect-ratio of the copper windings (i.e., increase the winding thickness) to reduce DC resistance, while reducing the space between the windings for further miniaturization of the devices.

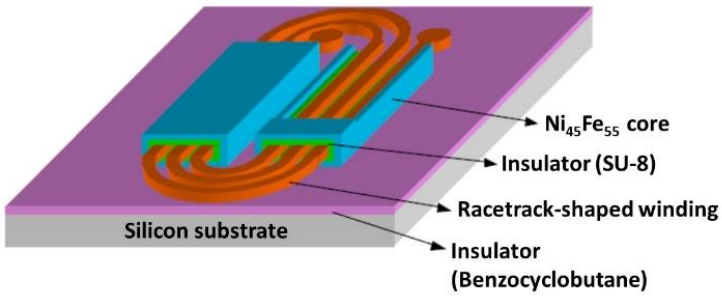


Figure 2.4 Racetrack-shaped microfabricated inductor [38].

### 2.2.2 Strip-Line Inductors

One of the simplest inductor geometries is a strip-line shape where the inductor consists of a single-turn winding and a magnetic material wrapped around the winding. The strip-line inductors typically possess very low winding resistance and use sputtered thin magnetic films for very high frequency application (> 20 MHz) [12, 18]. However, due to the limited inductance from the single-turn winding, researchers have focused on improving the inductance by overall magnetic thickness through lamination techniques. In 2013, microfabricated V-groove inductors with multilayer CoZrO film was fabricated (Figure 2.5), demonstrating an inductance of 3.4 nH up to 100 MHz with a peak quality factor over 50 at 100 MHz [12].

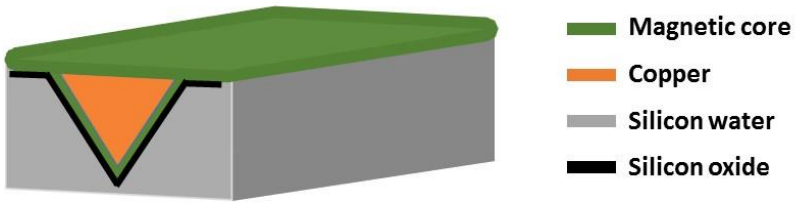


Figure 2.5 Schematic of a typical V-groove inductor [12].

### 2.2.3 Solenoid Inductors

Solenoid and toroid inductors use 3-dimensional coil geometries to wrap microfabricated windings around magnetic cores. A typical microfabricated solenoid inductor is a bar-type inductor that uses a bar-shaped magnetic core as shown in Figure 2.6 (a). In 2008, Lee *et al*. developed integrated solenoid inductors with a CoZrTa magnetic core, demonstrating inductance density over 200 nH/mm$^2$ up to 100 MHz with a peak quality factor of approximately 6 at 30 MHz [40]. The solenoid inductors can take advantage of an anisotropic magnetic core. However, the open magnetic path in the solenoid geometry is not able to fully utilize the magnetic cores (i.e., there is infinite air-

gap between the two ends of the core, thus the effective permeability of the core decreases), resulting in lower inductance density. Also, this geometry may not be completely free of EMI to components in close proximity.

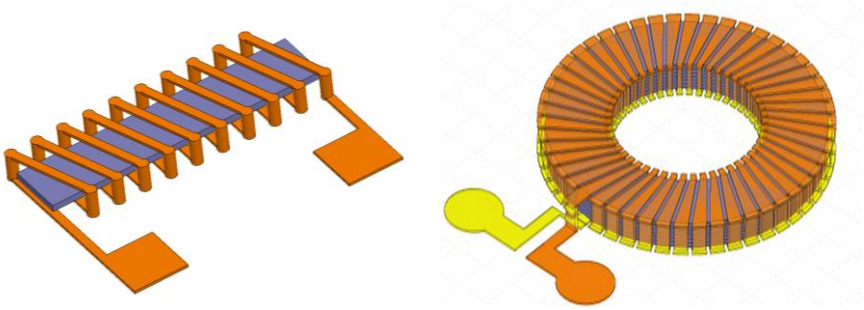

(a) (b)

Figure 2.6 Schematic of typical microfabricated inductors with magnetic cores. (a) solenoid inductor, and (b) toroid inductor

### 2.2.4 Toroid Inductors

Toroid inductors consists 3-dimensional windings wrapped around a toroidal magnetic core as shown in Figure 2.6 (b). In 2003, Park *et al*. developed a microfabricated toroid inductor integrated with laminated NiFe core, demonstrating an inductance of 2.3 μH and a peak quality factor of 9.2 at 3 MHz [11]. The toroidal design has the advantages of fully exploiting the high permeability magnetic core, possibly resulting in high inductance density and quality factor. However, inducing magnetic anisotropy to the magnetic core is difficult due to the core geometry.

From the microfabrication point of view, both solenoid and toroid windings are more challenging due to their complex 3-dimensional geometry compared to spiral windings. Also, methods to achieve high-aspect-ratio vertical winding structures should be researched in order to accommodate large volume magnetic cores for high power handling.

## 2.3 DC-DC Converters with Integrated Magnetics

Using the microinductors and magnetic cores stated above, there have been numerous attempts to realize power supply in package and power supply on chip solutions. Table 2.2 summarize reported DC-DC converters integrated with magnetic core inductors.

Table 2.2 Review of DC-DC converters with integrated magnetics

| Ref. | $P_{o\_density}$ [W/cm$^2$] | $P_o$ [W] | $\eta$ [%] | $f_{sw}$ [MHz] | $I_o$ [A] | $V_{in}$ [V] | $V_{out}$ [V] | $L_{\_density}$ [nH/mm$^2$] | L [nH] | $Q_{pk}$ | Core material | |
|---|---|---|---|---|---|---|---|---|---|---|---|---|
| [41] | 6.25 | 10 | 88 | 0.5 | 3 | 5 | 3.3 | 2.26 | 880 | N/A | MnZn | ↑ Sintered ferrite |
| [42] | 8.16 | 1 | 83 | 1.8 | 0.2 | 3.6 | 1.5 | 89.8 | 1100 | N/A | NiZn | |
| [43] | 6.25 | 10 | 90 | 0.5 | 3 | 5 | 3.3 | 4.75 | 1900 | N/A | MnZn | |
| [16] | N/A | 4 | 80 | 1 | 4 | 5 | 1 | 0.62 | 140 | 30 | MnZn | |
| [44] | 1.44 | 0.36 | 91 | 2 | 0.2 | 3.6 | 1.8 | 100 | 2500 | N/A | NiZnCu | |
| [45] | 2.04 | 16 | 78 | 1.3 | 16 | 5 | 1 | 0.13 | 100 | N/A | NiZn | |
| [46] | 4 | 0.36 | 80 | 6 | 0.5 | 3.6 | 1.8 | 43.3 | 390 | 10 | NiZn | |
| [47] | 16.78 | 24 | 80 | 5 | 20 | 12 | 1.2 | 0.17 | 24 | N/A | NiZn | ↓ |
| [48] | 10.42 | 0.6 | 90 | 2.8 | 0.3 | 3.6 | 1.8 | 277.8 | 1060 | 28 | NiZn | |
| [49] | 3.06 | 1.5 | 50 | 5 | 0.1 | 9 | 15 | 51.95 | 1000 | 10 | CoZrNb | Sputtered thin film |
| [50] | 1 | 1 | 83.3 | 3 | 0.35 | 4.5 | 3 | 60 | 960 | 4.3 | CoHfTa | |
| [12] | 36.26 | 3.3 | 86 | 11 | 1 | 7 | 3.3 | 8.02 | 3.4 | 22 | CoZrO | |
| [51] | 0.25 | 0.25 | 70 | 7 | 0.04 | 3 | 6.5 | 33.33 | 200 | 0.4 | NiFe | Electrodeposited metallic alloy |
| [52] | 1.38 | 1.9 | 71 | 2.2 | 0.2 | 7 | 12 | 35.09 | 2300 | 9.2 | NiFe | |
| [53] | N/A | 5 | 82 | 5 | 2.5 | 3 | 2 | 2.8 | 100 | 4 | NiFe | |
| [54] | 0.32 | 0.54 | 74 | 8 | 0.45 | 3.6 | 1.2 | 38.26 | 440 | 11.7 | NiFe | |
| [55] | N/A | 1.8 | 74 | 20 | 1 | 4.8 | 1.8 | N/A | 88 | N/A | NiFe | |

### 2.3.1 DC-DC Converters with Integrated Magnetics – using Ferrite Cores

Ferrite cores have been widely researched for high frequency DC-DC converter applications due to their high resistivity (and therefore suppressed eddy current losses). The ferrite cores used in this application are typically NiZn, MnZn, and their alloys. In

most cases, ferrite core inductors are used as a substrate of DC-DC converters to minimize the total inductor footprint.

In 2002, Manguel *et al*. fabricated a spiral type inductor using a ferrite core from Ferroxcube with an inductance density of 2.26 nH/mm$^2$ [41]. By stacking other components (such as capacitors and ICs) as shown in Figure 2.7, they developed a prototype DC-DC converter for 5 V input and 3.3 V output, demonstrating 88% converter efficiency at 3 A output current with a switching frequency of 500 kHz. Later in 2004, they improved an inductance density (4.75 nH/mm$^2$) and performed more analysis on the prototype DC-DC converter, including thermal analysis and loss analysis [43].

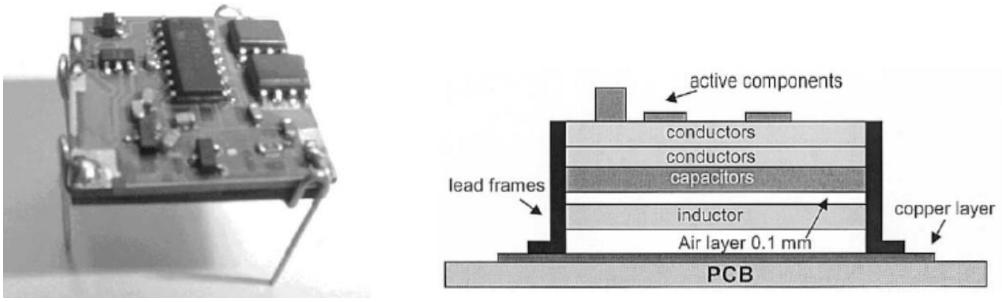


(a) (b)

Figure 2.7 A prototype DC-DC converter having a spiral inductor with ferrite core as a substrate [43]. (a) Images (20 x 20 x 4 mm$^3$), and (b) cross-section structure.

In 2003, Fuji Electric Company (Japan) published inductors on ferrite wafers as a substrate on which to mount an IC chip [42]. The size of the resultant DC-DC converter module is 3.5 × 3.5 × 1 mm$^3$ for 1 W maximum output power, demonstrating 83 % efficiency for 3.6 V input and 1.8 V output at 1.8 MHz switching frequency. Recently, in 2013, they published integrated DC-DC converter with a ferrite core inductor for a cellular phone application [48]. The size of the inductor is 2.4 × 2.4 × 1 mm$^3$ with an inductance of 1.06 μH. By wire-bonding the inductor with an advanced IC chip as shown in Figure 2.8,

the DC-DC converter operated with 90 % efficiency at 2.8 MHz switching frequency for 3.6 V input and 1.8 V output.

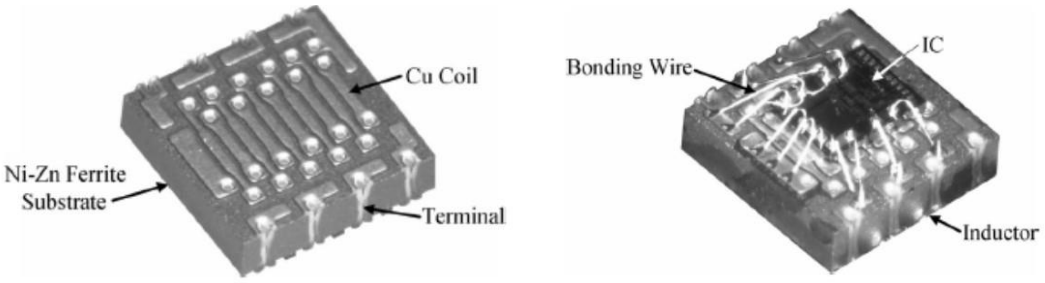


(a) (b)

Figure 2.8 Integrated DC-DC converter [48]. (a) Inductor with NiZn ferrite core, and (b) IC chip bonded to the inductor.

Low temperature co-fired ceramic (LTCC) ferrite cores have been researched by Kyocera Corporation [44] and Virginia Tech (Center for Power Electronics Systems) [45, 47] for miniaturized DC-DC converters. In 2006, Kyocera Corporation (Japan) reported an LTCC substrate with embedded high value inductor (> 1 μH) for miniaturization and low profile of a DC-DC converter [44]. A high inductance density of 100 nH/mm$^2$ is embedded into a 5 × 5 mm$^2$ LTCC substrate on which other component chips are mounted (Figure 2. 9 (a)). The DC-DC converter demonstrated 91 % efficiency at 2 MHz switching frequency for 3.6 V input and 1.8 V output.

The LTCC inductor substrates from Virginia Tech possess very low numbers of winding turns. Although it shows a very low inductance density, the inductor can operated with high output current, resulting in high converter power density. By integrating the LTCC inductor substrate with a GaN switch as shown in Figure 2.9 (b), 80 % efficiency at 5 MHz switching frequency with 12 V input and 1.2 V output has been achieved [47]. The maximum output current was 20 A, and the output power was 24 W.

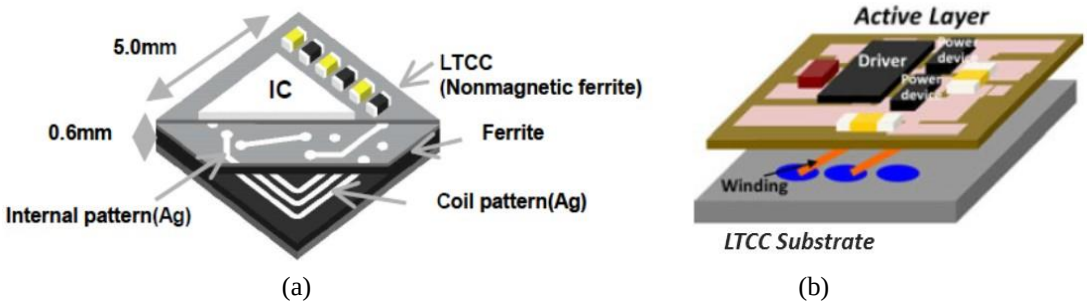


(a) (b)

Figure 2.9 DC-DC converter with LTCC inductor substrate from (a) Kyocera Corporation [44] and (b) Virginia Tech [47].

### 2.3.2 DC-DC Converters with Integrated Magnetics – using Thin Film Cores

In order to overcome the high sintering temperature and low saturation flux density of ferrite cores, thin film magnetic cores have been deposited using sputtering for DC-DC converters. In 1994, Toshiba Corporation reported a thin film inductor which consists of a spiral coil between top and bottom sputtered CoZrNb amorphous films with uniaxial magnetic anisotropy [49]. The inductor demonstrated a constant inductance of 1μH up to 10 MHz with peak quality factor of 10 at 10 MHz. A developed DC-DC boost converter (from 9 V to 15 V) using the thin film inductor size was 7 × 7 × 2 $mm^3$ (Figure 2. 10 (a)), demonstrating an efficiency of 50% at 5 MHz switching frequency and 1.5 W output power.

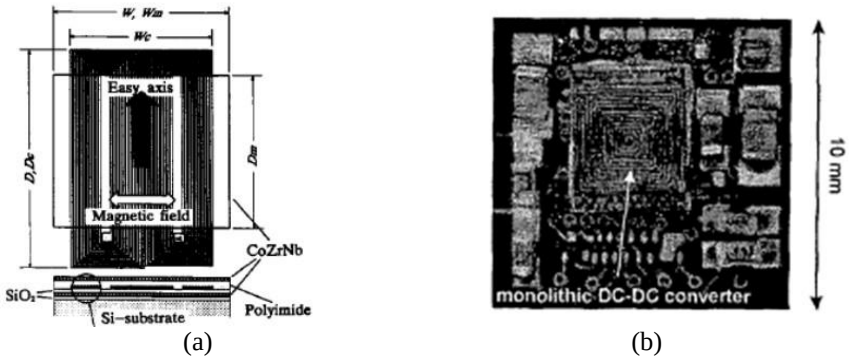


(a) (b)

Figure 2.10 Monolithic DC-DC converter using thin film inductor from (a) Toshiba Corporation [49] and (b) Fuji Electric Company [50].

Fuji Electric Company also reported a spiral inductor with sputtered CoHfTaPd core, demonstrating an inductance of 960 nH with peak quality factor of 4.3 at 3 MHz [50]. A developed DC-DC buck converter (from 3.5 - 5 V to 3 V) using the thin film inductor was 10 × 10 × 1.8 $mm^3$ (Figure 2. 10 (b)), demonstrating an efficiency of 83.3% at 3 MHz switching frequency and 1 W output power.

### 2.3.3 DC-DC Converters with Integrated Magnetics – using Metallic Alloy Cores

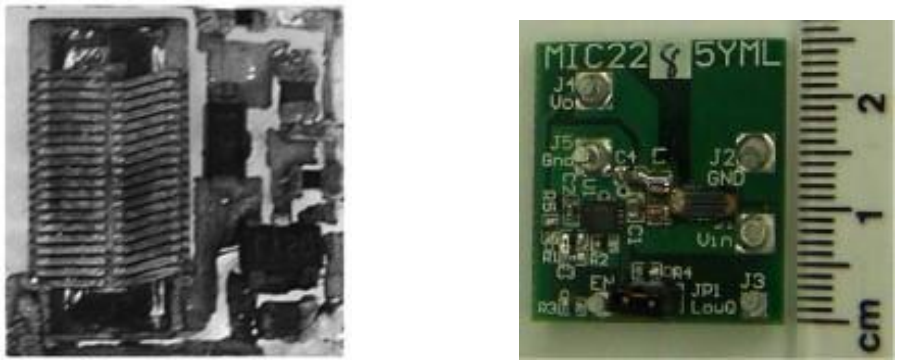


(a) (b)

Figure 2.11 DC-DC converters using microfabricated inductors with electrodeposited permalloy cores (a) Toroid inductor with laminated permalloy core [52] (b) Racetrack-shaped inductor with permalloy core [54].

As mentioned earlier, electrodeposited metallic alloys (e.g., NiFe) has been researched for low-profile DC-DC converters. In 2003, Srinivasan *et al*. developed a surface mounted DC-DC boost converter using micromachined toroid inductors with electrodeposited permalloy ($Ni_{80}Fe_{20}$) core, demonstrating 0.25 W output power with 70 % converter efficiency [51]. The converter boosted 3 V input to 6.5 V output at a switching frequency of 7 MHz, and size of the converter was 10 × 10 × 1 $mm^3$. Later in 2007, Galle *et al*. also presented a prototype DC-DC buck converter using a microfabricated spiral inductor with electrodeposited permalloy, demonstrating 80% efficiency at 5 MHz switching frequency [53]. It converted input voltage of 3 V to output voltage of 2 V with

output current of 2.5 A. In 2003, J.W. Park *et al*. used a laminated permalloy core to improve converter power density [52]. The magnetic core had 72 laminations of 1-µm-thick permalloy films. The inductor with the core exhibited an inductance of 2.3 µH with peak quality factor of 9.2 at 3 MHz. A DC-DC boost converter (from 7V to 12 V) using the inductor is shown in Figure 2.11 (a). The converter demonstrated 71% efficiency at 2.2 MHz switching frequency yielding 1.9 W output power.

The Microsystems Centre of Tyndall National Institute also reported racetrack-shaped microfabricated inductors with electrodeposited permalloy cores, demonstrating an inductor for use in DC-DC buck converters. In 2008, Wang *et al*. reported a 7-turn racetrack-shaped microinductor with 4.2-µm-thick permalloy core, demonstrating an inductance of 440 nH with peak quality factor of 11.7 at 5.5 MHz [54]. Operating the inductor with a commercially available 8 MHz buck converter (from 3.6 V to 1.2 V), 74% efficiency was achieved at 0.45 A load current. The racetrack-shaped inductor was also utilized in a 20 MHz DC-DC converter, demonstrating 74% efficiency for converting 4.8 V input to 1.8 V output [55]. The load current was 1 A and the output power was 1.8 W.

### 2.3.4 Commercial DC-DC Converter Modules

In addition to the research effort toward PSiP and PSoC, commercial DC-DC converter modules with integrated inductors were also developed as summarized in Table 2.3. In the converter modules, an inductor and IC chip are placed side by side (Figure 2.12 (a)), or the IC chip is stacked onto the inductor (Figure 2.12 (b)) to further reduce the surface area. The power densities of the commercial DC-DC converter modules exceed 10 W/cm$^2$, and the highest efficiencies are higher than 90% at switching frequencies that

exceed 1 MHz. Typically, these converter modules require several external surface-mount components (e.g., capacitors and resistors) to be operated.

Table 2.3 Commercial DC-DC buck converter modules with integrated inductors

| Name | $V_{in}$ [V] | $V_{out}$ [V] | $I_{out}$ [A] | $f_{sw}$ [MHz] | *Eff* [%] | Footprint [mm$^2$] |
|---|---|---|---|---|---|---|
| EN5312QI [56] | 2.4 – 6.6 | 0.8 – 3.3 | 0.1 – 1 | 4 | 65 – 92 | 5 × 4 |
| LM3218 [57] | 2.7 – 5.5 | 0.8 – 3.6 | 0.05 – 0.6 | 2 | 80 – 95 | 3 × 2.5 |
| LTM8022 [58] | 3.6 – 36 | 0.8 – 10 | 0.4 – 1 | 0.2 – 2.4 | 79 – 91 | 11.25 × 9 |
| MIC33050 [59] | 2.7 – 5.5 | 1 – 3.3 | 0.1 – 0.6 | 4 | 70 – 93 | 3 × 3 |

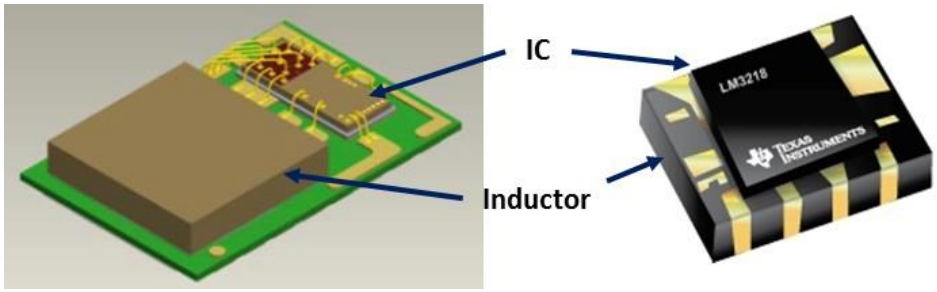


(a) (b)

Figure 2.12 Integration of inductor and IC in commercial DC-DC converter modules. (a) Altera (Enpirion) [60], and (b) Texas Instrument [57].

## 2.4 Advantages and Challenges of Integrated Magnetics

Form Chapters 1 and 2, it is found that the use of an appropriate magnetic material is critical to realize ultracompact DC-DC power converters. Use of such magnetic material together with advanced microfabrication technology for on-chip inductors can enable the realization of PSiP and PSoC. However, design of the microinductors with magnetic cores requires several considerations including the magnetic core saturation as well as frequency-dependent core losses. Therefore, it is still required to develop magnetic components that simultaneously enables both high power handling though high saturation flux density and high volume, and minimized magnetic losses at high operation frequency (> 1 MHz).

# CHAPTER 3

# NANOLAMINATED MAGETNIC METALLIC ALLOY CORES

In previous chapters, integrated magnetics approaches for DC-DC converters were reviewed. Electroplated metallic alloys exhibit excellent magnetic properties (e.g., high saturation flux density and low coercivity) compared to conventional ferrites. However, eddy-current losses preclude their use in many switching converter applications, due to the challenge of simultaneously achieving sufficiently thin laminations such that eddy currents are suppressed (e.g., 500 nm – 1000 nm for MHz frequencies), while simultaneously achieving overall core thickness such that substantial power can be handled (e.g., tens to hundreds of μm). As stated in chapter 1, *lamination* is a promising solution to simultaneously achieve both large magnetic volume and suppressed eddy-current losses for metallic alloys. In this chapter, fabrication and characterization of *nanolaminated ferromagnetic metallic cores* comprising tens to hundreds layers of metallic alloy film with submicron individual layer thickness are presented.

## 3.1 Introduction

In order to develop nanolaminated ferromagnetic metallic alloy cores, a CMOS-compatible fabrication approach based on automated sequential electrodeposition has been adopted and optimized for this application. Permalloy ($Ni_{80}Fe_{20}$) and $Co_{44}Ni_{37}Fe_{19}$ materials are utilized as the electrodeposited metallic alloys.

First, nanolaminated permalloy cores were developed to demonstrate the fabrication approach and core performance since electrodeposited permalloy has been widely used and is well-known as a magnetic core material [26 - 28]. Then, electrodeposited CoNiFe, an emerging magnetic material possessing advanced intrinsic

magnetic properties (i.e., higher saturation flux density and lower coercivity), has been studied to develop nanolaminated CoNiFe cores. The following sections present fabrication, characterization, and comparison of nanolaminated cores with both permalloy and CoNiFe materials.

## 3.2 Permalloy and CoNiFe Thin Films

### 3.2.1 Electrodeposition of Permalloy and CoNiFe Thin Films

Electroplated permalloy and CoNiFe are widely researched magnetic materials due to their superior magnetic properties than conventional ferrite, and several electrodeposition approaches for them have been established [34 - 36]. Table 3.1 details the electrodeposition conditions (i.e., bath composition and plating parameters) that have been used in this research. During electrodeposition, a 5x5 $cm^2$ nickel sheet anode was utilized and no agitation of the electrolyte is conducted to minimize the convective mass-transfer effect [61].

Table 3.1 Electrodeposition conditions for permalloy and CoNiFe.

| Permalloy | | CoNiFe | |
|---|---|---|---|
| Component | Quantity | Component | Quantity |
| $NiSO_4 \cdot 6H_2O$ | 1.29 [mol/L] | $CoSO_4 \cdot 7H_2O$ | 0.08 [mol/L] |
| $FeSO_4 \cdot 7H_2O$ | 0.029 [mol/L] | $NiSO_4 \cdot 6H_2O$ | 0.2 [mol/L] |
| $NiCl_2 \cdot 6H_2O$ | 0.039 [mol/L] | $FeSO_4 \cdot 7H_2O$ | 0.03 [mol/L] |
| Boric acid | 0.4 [mol/L] | NH4Cl | 0.3 [mol/L] |
| Saccharin | 3 [g/L] | Boric acid | 0.4 [mol/L] |
| | | Sodium saccharin | 2.1 [g/L] |
| | | Sodium lauryl sulfate | 0.01 [g/L] |
| Temperature | 23 ℃ | Temperature | 23 ℃ |
| pH | 2.7 - 2.9 | pH | 2.7 - 2.9 |
| Deposition rate | 0.25 μm/min | Deposition rate | 0.25 μm/min |
| Current density | 10 [$mA/cm^2$] | Current density | 20 [$mA/cm^2$] |

In the case of CoNiFe electrodeposition, sodium saccharin and sodium lauryl sulfate were added to relieve the deposition stress and improve ionic mass transfer. Ammonium chloride was utilized to enhance the electrolyte conductivity. With the electroplating conditions in Table 3.1, the composition of the deposited materials was measured as 80%-nickel and 20%-iron for permalloy and 44%-cobalt, 37%-nickel, and 19%-iron for CoNiFe (measurement techniques described below).

### 3.2.2 Properties of CoNiFe Thin Film

Before commencing the full automated sequential electrodeposition process leading to a multilayer structure, initial material characterization experiments were carried out on single film laminations. A 1-μm-thick CoNiFe film was deposited with various current densities (5 - 30 mA/cm$^2$) to develop the optimal electrodeposition condition for CoNiFe. Note that electrodeposition condition for permalloy has been established and optimized by our research group previously [28].

For the characterization of the CoNiFe film, an atomic force microscope (AFM, Veeco AFM 3100) was used to investigate the surface topology of the film, energy-dispersive X-ray spectroscopy (EDX, Hitachi S-3700N) was used for atomic composition assessment of the CoNiFe material, and vibration sample magnetometry (VSM, LakeShore 7300) was used to measure the saturation flux density and coercivity of the CoNiFe material.

Figure 3.1 shows the dependence of the magnetic properties (i.e., saturation flux density $B_s$ and coercivity $H_c$) as a function of current density during deposition. Note that over 20 samples were deposited and measured at each current density and the presented

properties represent average values for a given current density. From the graph, it was observed that the saturation flux density of the CoNiFe material exceeds 1.4 T and the coercivities are lower than 1.5 Oe over this current density range.

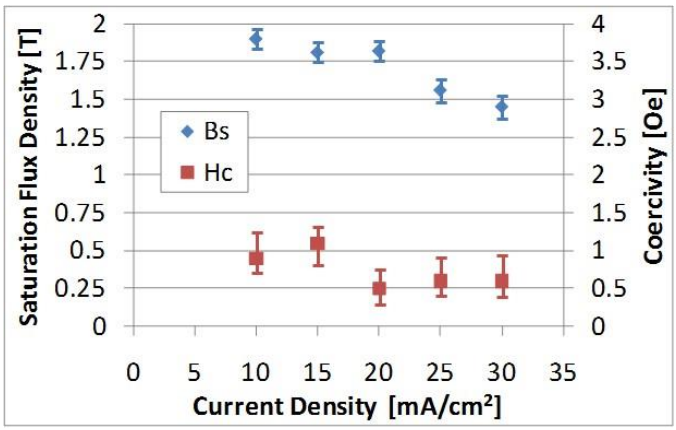


Figure 3.1 Saturation flux density and coercivity of 1-µm-thick CoNiFe film as a function of deposition current density. Data points represent average values and error bars represent the data range.

In addition to the magnetic properties, the composition of the CoNiFe films was also measured. Table 3.2 summarizes the compositions and magnetic properties of CoNiFe film with various current densities.

Table 3.2 Properties and composition of electrodeposited CoNiFe

| Current density [mA/cm$^2$] | Composition [%] | | | Deposition rate [µm/min] | Bs [T] | Hc [Oe] |
|---|---|---|---|---|---|---|
| | Cobalt | Nickel | Iron | | | |
| 5 | 58.7 | 13.37 | 27.93 | 0.0625 | 1.19 | 8.9 |
| 10 | 54.42 | 19.11 | 26.47 | 0.125 | 2.09 | 1.5 |
| 15 | 50.97 | 26.72 | 22.31 | 0.188 | 1.83 | 1.4 |
| 20 | 44.2 | 37.13 | 18.67 | 0.25 | 1.81 | 0.5 |
| 25 | 42.02 | 40.12 | 17.86 | 0.313 | 1.6 | 0.6 |
| 30 | 42.79 | 38.69 | 18.52 | 0.375 | 1.49 | 0.6 |

From Table 3.2, it was observed that the composition of nickel increases as the current density increases, while the other components (i.e., cobalt and iron) exhibit the

opposite tendency, which is in agreement with previous reports [34 - 36]. It was also observed that increasing nickel composition (e.g., decreasing cobalt and iron composition) results in decreasing coercivity. However, it seems that the decreasing coercivity trend saturates near 0.5 Oe (however, it should also be noted that this is approaching the resolution of the measurement tool). On the contrary, increasing cobalt and iron composition results in increasing saturation flux density. However, the magnetic properties degrade rapidly when the current density decreases below 5 mA/cm$^2$. Over this current density range, 20 mA/cm$^2$ was selected for further use since it provided both high saturation flux density (1.82 T) and the lowest coercivity (0.5 Oe).

### 3.2.3 Comparing Properties of Permalloy and CoNiFe Thin Films

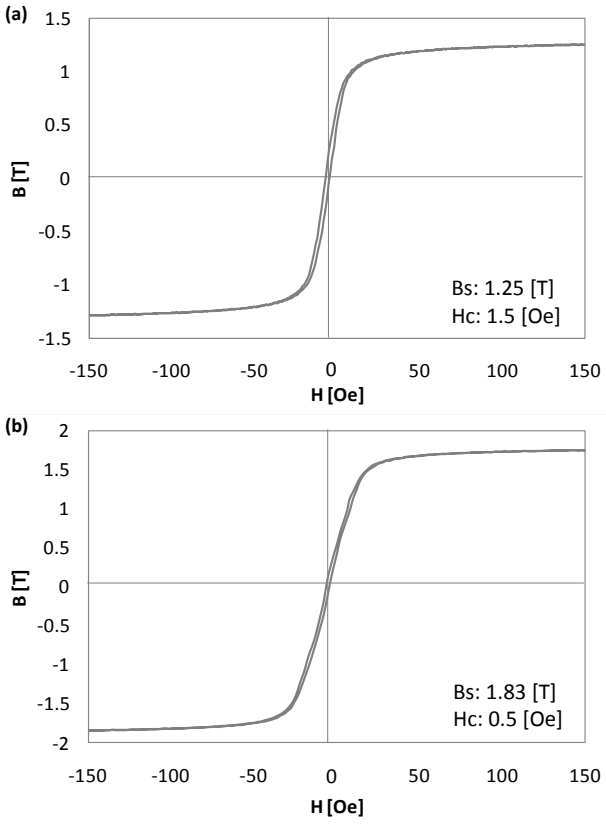


Figure 3.2 Measured B-H hysteresis curves of (a) permalloy and (b) CoNiFe.

Figure 3.2 shows measured B-H hysteresis curves of both electrodeposited permalloy and CoNiFe films. Current densities of 10 mA/cm$^2$ and 20 mA/cm$^2$ were used for permalloy and CoNiFe, respectively. As shown in the graph, CoNiFe exhibits higher saturation flux density (1.83 T) as well as lower coercivity (0.5 Oe) than permalloy, implying higher power density capability and lower intrinsic magnetic losses (i.e., hysteresis losses) as an energy storage/transfer material.

### 3.3 Sequential Electrodeposition for Multilayer Magnetic Structure

After the characterization and comparison of the properties of CoNiFe and permalloy thin films, these materials are further fabricated as nanolaminated magnetic cores for high-frequency and high-power DC-DC converter applications. The fabrication process for the nanolaminated magnetic cores is based on automated sequential electrodeposition of ferromagnetic materials (i.e., permalloy or CoNiFe) and sacrificial material (i.e., copper), followed by selective removal of the sacrificial layers so as to insulate each magnetic layer [62, 63]. Figure 3.3 shows a schematic of the automated sequential electrodeposition system, which is based on a robotic arm (i.e., computer-controlled X-Y-Z stage) that moves a cathode bearing the growing films from one bath to another. Copper was chosen for the sacrificial material as it exhibits low surface roughness, high adhesion to the magnetic material, and is able to be selectively etched away without degrading or etching the magnetic materials. Two rinsing steps are also performed between the magnetic material and copper electrodeposition to prevent cross contamination of the electrolytes. The number of layers is determined as desired with the robot system, and the thickness of individual layer is precisely controlled by adjusting the electrodeposition time. This robot-assisted system allows the fabrication of hundreds of layers of ferromagnetic

material and copper, which is a significant improvement compared to the previous work done by manual multilayer electrodeposition [11].

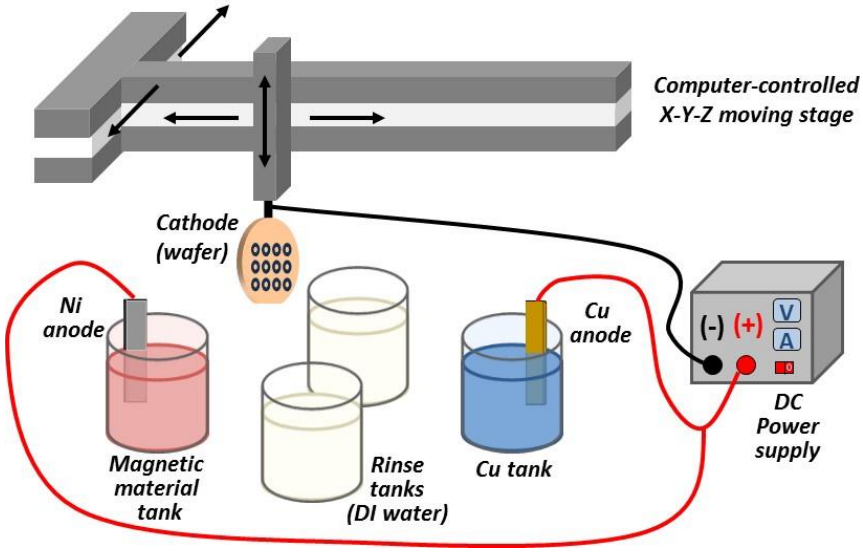


Figure 3.3 Schematic of automated sequential electrodeposition system.

The sequential electrodeposition is performed through a core-shape-defining photoresist mold on a silicon wafer substrate bearing a $SiO_2$/titanium/copper/titanium seed layer. An approximately 500 nm $SiO_2$ layer is deposited on the 4-inch silicon water using PECVD (plasma enhanced chemical vapor deposition). The titanium/copper/titanium layers are deposited using sputtering and the thicknesses are 200 nm, 500 nm, and 200 nm, respectively. A negative photoresist (NR21-20000P, Futurrex) was used to develop 50 - 100 um-thick molds with precisely designed patterns. After the pre-electrodeposition sample preparation (i.e., titanium etching and copper de-oxidation), the mold is filled with alternating layers of magnetic material (permalloy or CoNiFe) and copper using the automated sequential electrodeposition system (see Figure 3.6 (c)). The baths described in Table 3.1 was utilized for the electrodeposition of permalloy and CoNiFe, and a

commercial copper bath (Grobet, Clean Earth Cu-mirror solution) containing brighteners and levelers was utilized for copper electrodeposition.

The fabricated multilayer structure of alternating CoNiFe/copper was characterized to examine any magnetic property degradation compared to the 1-µm-thick single CoNiFe film, before etching the sacrificial copper. In order to assess the magnetic properties (i.e., saturation flux density and coercivity) of the CoNiFe/copper multilayer, VSM measurement was conducted on multilayers with differing numbers of laminations. For all multilayers, the individual lamination thickness is maintained at 1 µm. Figure 3.4 shows the magnetic properties of the multilayer as a function of the number of laminations, demonstrating that the saturation flux density of the multilayer remains approximately 1.8 T and does not change with increasing numbers of laminations. The coercivity of the laminated film tends to increase compared to a single lamination deposited directly on a sputtered copper seed layer, possibly due to the higher roughness of electrodeposited copper compared to sputtered seed copper [36].

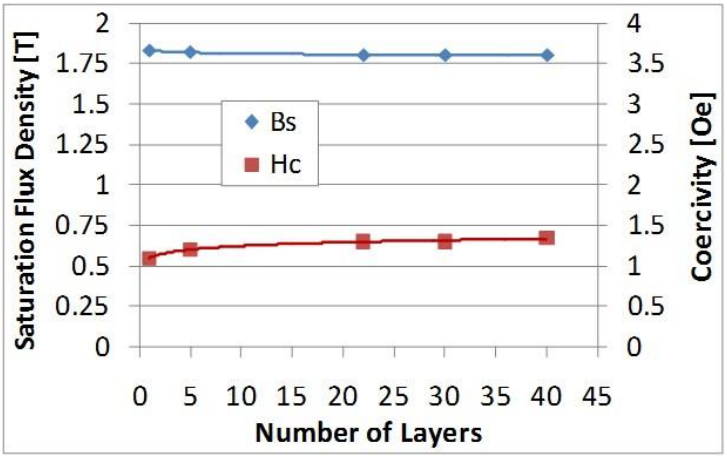


Figure 3.4 Saturation flux density and coercivity of CoNiFe/copper multilayer as a function of number of laminations.

In order to investigate the effect of the CoNiFe film roughness, atomic force microscopy measurements have been conducted on the two different seed layers (i.e., sputtered copper and electroplated copper) as well as the CoNiFe films deposited on the two seed layers. The average roughness of the sputtered copper is 2.78 nm, while that of the electrodeposited copper is 10.9 nm. Consequently, it is observed that the average roughness of the CoNiFe film on the electrodeposited copper layer is 17.1 nm, which is higher than that of the CoNiFe film on the sputtered copper of 10.6 nm. Figure 3.5 illustrates an example of 3-D surface topology of electrodeposited CoNiFe films on the two different seed layers. Although the increased average roughness of the CoNiFe film deposited on electrodeposited copper may degrade the magnetic property of the film (increased coercivity), the measured coercivity is maintained less than 1.5 Oe up to 40 lamination layers as shown in Figure 3.4.

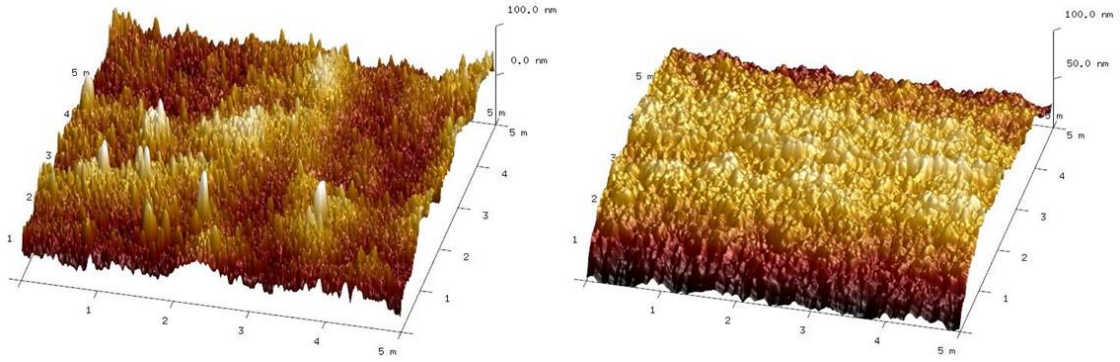


(a) (b)

Figure 3.5 Surface topology of electrodeposited CoNiFe films (a) on sputtered copper seed layer and (b) on electrodeposited copper seed layer.

### 3.4 Fabrication of Nanolaminated Magnetic Cores

Once the alternating layers of magnetic material and copper are electrodeposited, the sacrificial copper layers should be selectively removed, while the magnetic layers are separated from each other without collapse. In order to realize the laminated

magnetic/insulator structure, two fabrication techniques were developed: 1) SU-8 support approach, and 2) Surface-tension-driven assembly of metallic nanosheets. The two techniques are described and compared in the following sections.

### 3.4.1 SU-8 Support Approach

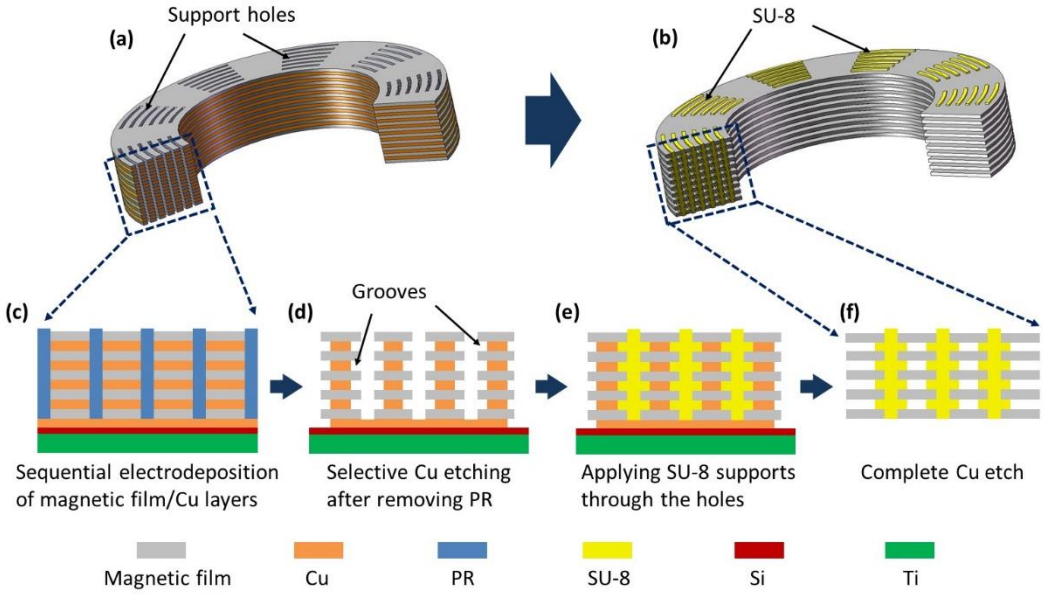


Figure 3.6 Fabrication of nanolaminated magnetic core using SU-8 support approach. (a) Schematic of electrodeposited magnetic film/copper multilayers (eddy currents are dominant). (b) Schematic of laminated magnetic film/insulator structure (eddy currents are suppressed). (c) - (f) Nanolaminated magnetic core fabrication steps.

Once the photoresist mold is filled with magnetic film/copper multilayers, the photoresist is removed by acetone. Then, a short selective copper wet-etch is performed to create lateral "grooves" around the sidewall of the structure (Figure 3.6 (d)). A saturated solution of copper sulfate in ammonium hydroxide ($NH_4OH$ + $CuSO_4$) is utilized as a copper etchant since it provides excellent selectivity between the magnetic layers and the copper. SU-8 epoxy is then applied through the "support-holes" depicted in Figure 3.6 (e), which refer to the areas that were covered by the plating mold during the electrodeposition.

A subsequent UV-exposure and post exposure bake allows a subset of the “support-holes” to be filled with cross-linked SU-8. Next, the sacrificial copper layers are completely removed in the etchant through the periphery of the structure and the “support-holes” unoccupied by SU-8, so that individual laminations can be created (Figure 3.6 (b) and (f)). Note that the non-conductive SU-8 filled in the “grooves” as well as in the support holes allows the magnetic layers to maintain their mechanical integrity and separation after the copper removal, in comparison to the previous work where an additional electrodeposition of conductive structures was employed for the same purpose [11]. Through this proposed approach, complete electrical insulation between magnetic layers is feasible, minimizing the source of eddy current losses.

Figure 3.7 shows various images of toroid nanolaminated magnetic cores comprising tens to hundreds of laminations with single layer thickness less than 500 nm. Figure 3.7 (a) shows optical images of toroidal shaped nanolaminated magnetic cores having inner diameter of 6 - 8 mm and outer diameter of 10 mm. A magnified top-view of the core is shown in Figure 3.7 (b), demonstrating the support holes. Note that the dimensions of the cores are precisely determined in batch-scale through the use of photolithography. From the cross-sectional view, it is observed that the permalloy layers have a uniform thickness of 300 nm after the selective etching of sacrificial copper layers (Figure 3.7 (c) and (d)). Also, cores with varying numbers of total layers and targeted lamination thickness could be manufactured by a simple adjustment of plating variables. A cross sectional view of a core comprising 70 layers of 500-nm-thick CoNiFe layers is shown in Figure 3.7 (e) and (f).

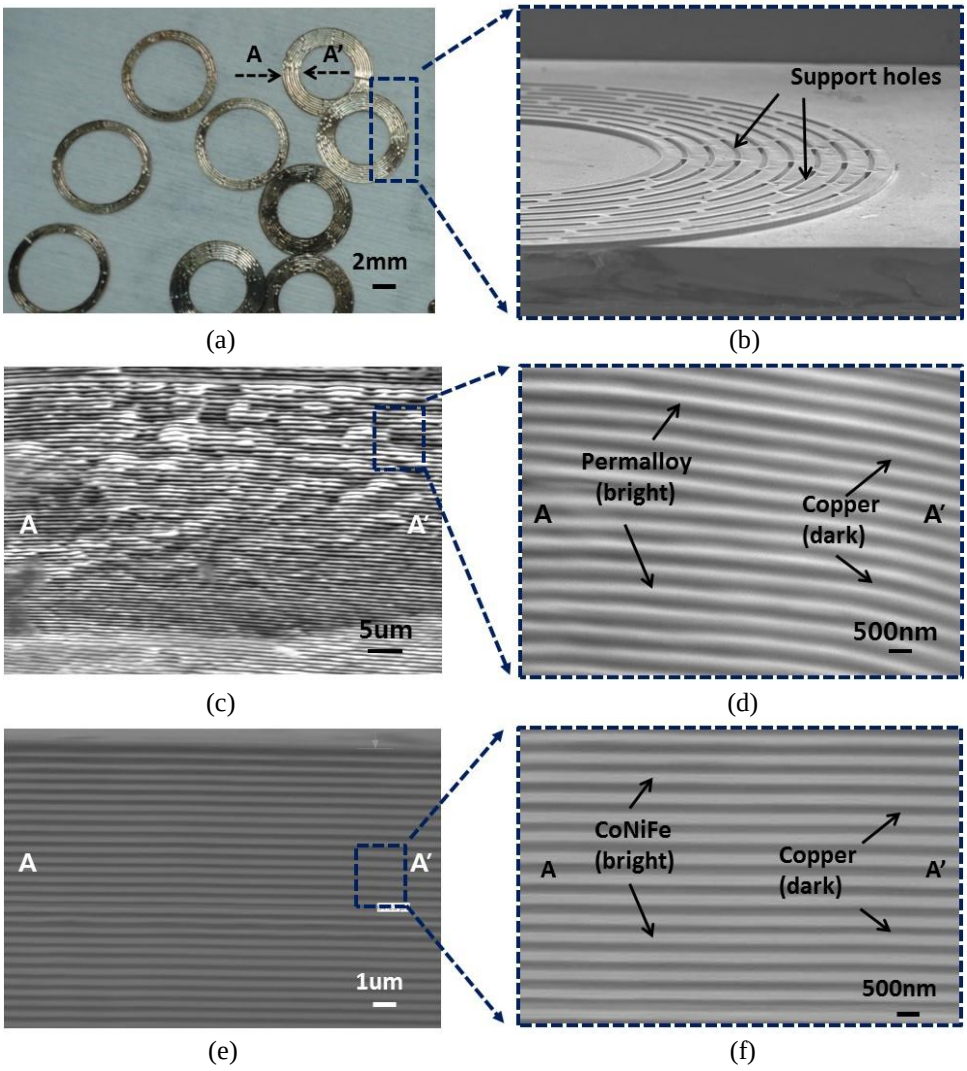


Figure 3.7 Images of nanolaminated magnetic cores using SU-8 support approach. (a) Batch-fabricated nanolaminated toroid cores. (b) Magnified top-view of the core showing support holes. (c), and (d) Cross section of a core with 300 layers of 300 nm permalloy laminations. (e), and (f) Cross section of a core with 70 layers of 500 nm CoNiFe laminations.

### 3.4.2 Surface-Tension-Driven Assembly

In case of the previous approach (i.e., SU-8 support approach), the total achievable thickness of the core is limited to the thickness of the mold (e.g., ~ 100 µm). In order to overcome the total thickness limitation as well as to simplify the fabrication process, we developed a surface-tension-driven assembly of nanosheets, in which individual magnetic

films can be induced to self-assemble. This technique relies on a surface-tension-driven coalescence and self-alignment of the wetted films when multiple films are removed from a liquid solution, resulting in laminated structures comprised of many layers of metallic sheets after evaporation of the liquid.

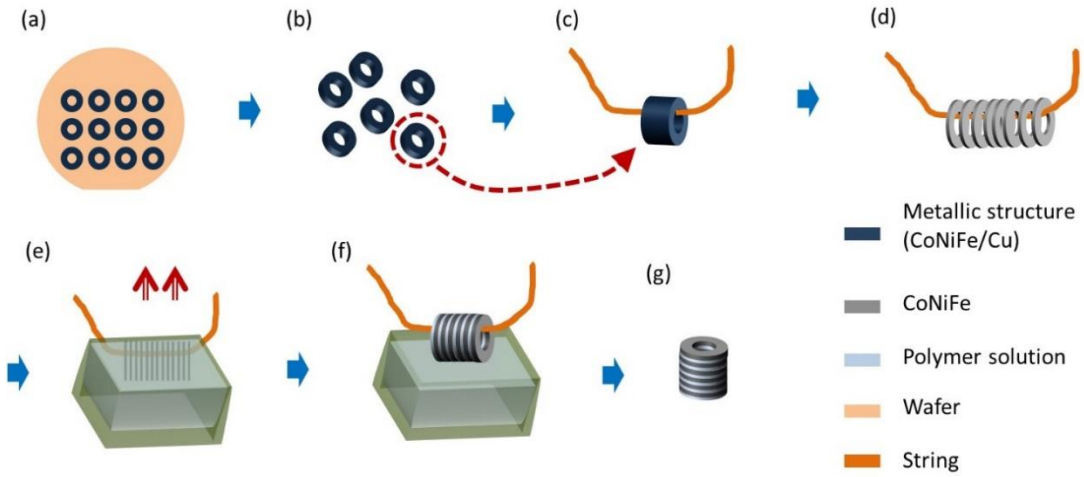


Figure 3.8 Fabrication sequence for surface-tension-driven assembly of nanosheets. (a) Electrodeposition of metallic multilayer structure on Si wafer, where each structure comprises multiple CoNiFe laminations connected by interlamination electrodeposited copper, (b) Removal of (CoNiFe/Cu) metallic multilayer structures from the substrate by seed layer removal, (c) Threading an assembly wire through the metallic multilayer structure, (d) Selective copper etching, resulting in a large number of thin CoNiFe laminations on the wire, (e) Immersion of the CoNiFe laminations in a liquid polymer solution, (f) Removing the laminations from the solution, (g) Polymer-insulated CoNiFe multilayer formed in a self-aligned fashion

The fabrication sequence for surface-tension-driven assembly of nanosheets for nanolaminated cores is described in Figure 3.8. Once sequential electrodeposition of the desired number of layers (Figure 3.6 (a) and Figure 3.8 (a)) is finished, the individual metallic structures (CoNiFe/Cu multilayer) are separated from the substrate silicon wafer by removing the underlying titanium seed layer in a 49% hydrofluoric acid solution as shown in Figure 3.8 (b). Then, a chemically-resistant wire (e.g., nylon, enameled magnet wire, or enameled Litz wire) is manually threaded through one of the unitary released

metallic structures as shown in Figure 3.8 (c). Since the metallic structure consists of multiple laminations of CoNiFe and copper, selective removal of the sacrificial copper layers causes the unitary multilayer structure to separate, producing a large number of individual thin CoNiFe laminations on the wire as shown in Figure 3.8 (d). It is noted that the CoNiFe laminations on the wire (Figure 3.8 (d)) were created from a single metallic structure fabricated using the automated sequential electrodeposition system, alleviating labor-intensive, manual threading of large numbers of individual thin laminations onto the assembly wire. The prepared individual CoNiFe laminations on the string are then immersed in a liquid polymeric solution, resulting in a conformal polymeric coating on the individual CoNiFe laminations, as shown in Figure 3.8 (e). A commercial Novec 1700 solution, which is designed for conformal 100nm coating on a metallic surface [64], was used as a polymeric solution; however, the selection of the polymeric material is unconstrained. The CoNiFe laminations are then removed from the solution and dried. As the solvent (a hydrofluoroether) in the Novec 1700 evaporates, the wet laminations coalesce in a self-aligned fashion to form a polymer-insulated CoNiFe multilayer assembly as shown in Figure 3.8 (f) and (g). A video recording of the assembly process can be observed online [65]. It should be noted that not only can a large number of CoNiFe laminations result from a single multilayer structure (where the number of laminations is determined by the automated sequential electrodeposition), a large number of multilayer structures can in principle be threaded onto the assembly wire, etched, and self-assembled into a single unitary core structure. In this manner, limitations on the number of laminations and achievable total thickness of assembled polymer-insulated multilayer are eliminated.

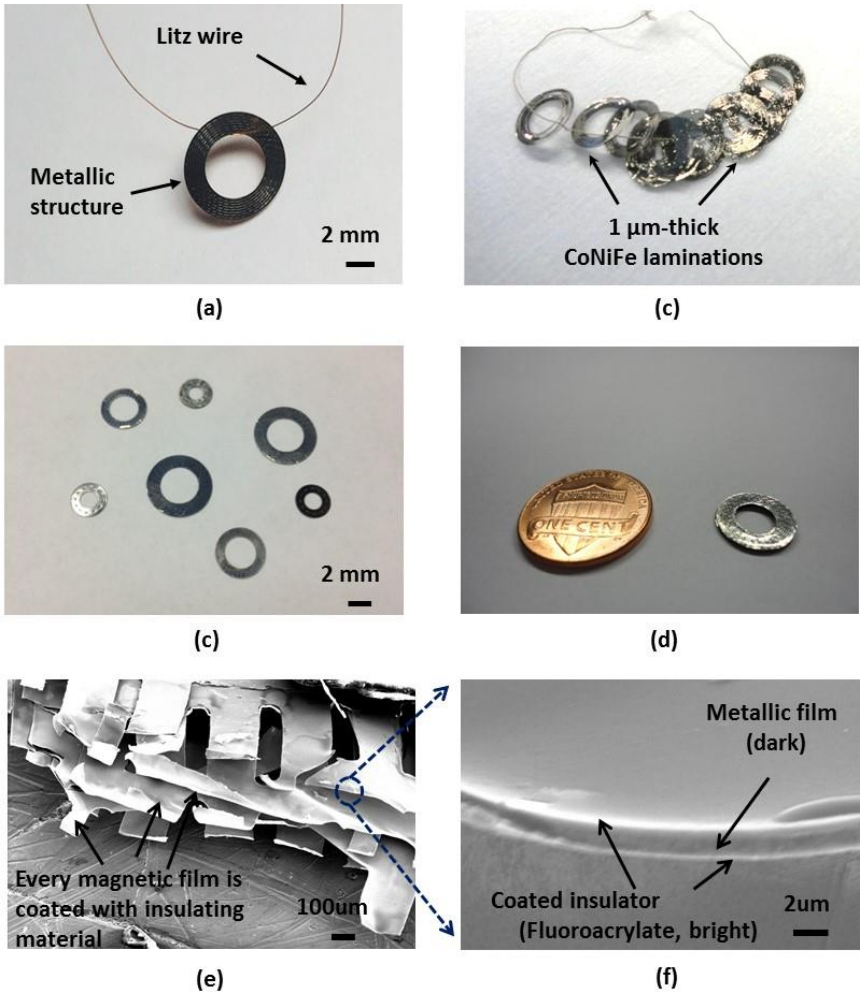


Figure 3.9 Images of nanolaminated CoNiFe cores fabricated through surface-tension-driven assembly. (a) Toroidal-shape metallic structure connected on a string. (b) Released CoNiFe laminations after copper layer etch. (c) Various sizes of assembled cores. (d) Tilted top-view of nanolaminated CoNiFe core comprising 300 layers of 1000-nm-thick laminations. (e) Cross-sectional SEM image of a core demonstrating each CoNiFe film is coated with insulating material. (f) Magnified view of (e) showing 100-nm-thick insulating polymer and 1000-nm-thick CoNiFe.

Figure 3.9 (a) shows a toroidal-shape metallic structure, comprising 40 layers of CoNiFe/Cu laminations, threaded on a Litz wire. The toroid has an inner diameter of 6 mm and an outer diameter of 10 mm. Once the sacrificial copper layers are removed, 40 separate layers of CoNiFe laminations are attained as shown in Figure 3.9 (b). Different sizes of nanolaminated CoNiFe cores fabricated through the surface-tension-driven

assembly are shown in Figure 3.9 (c). Figure 3.9 (d) shows a tilted top-view of nanolaminated CoNiFe core comprising 300 layers of 1000-nm-thick laminations. Cross-sectional SEM imaging of a core shows that each CoNiFe film is coated with polymeric insulating material (i.e., fluoroacrylate) as shown in Figure 3.9 (e). A magnified view (Figure 3.9 (f)) demonstrates that thicknesses of the insulating polymer and CoNiFe layers are 100 nm and 1000 nm, respectively.

### 3.4.2.1 Characterization of Surface-tension-driven Assembly

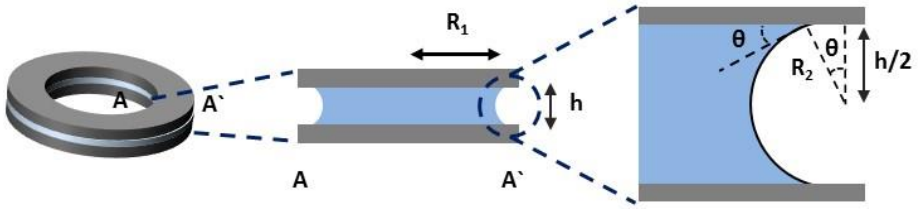


Figure 3.10 Schematic of two parallel laminations possessing liquid in between them.

In this section, further characterization of the surface-tension-driven assembly is described. When the individual CoNiFe laminations are removed from the polymer solution (i.e., Novec 1700), the liquid polymer is captured between the laminations by a capillary force. Considering two parallel laminations separated by a liquid (Figure 3.10) simplifies the theoretical analysis. In this case, the capillary pressure difference at the interface can be expressed using Laplace`s equation [66]:

$$\Delta P = \gamma\left(\frac{1}{R_1} - \frac{1}{R_2}\right) = \gamma\left(\frac{1}{R_1} - \frac{2cos\theta}{h}\right) \tag{3.1}$$

where $\gamma$ is the surface tension of the liquid [N/m], $\theta$ is the contact angle [deg], $R_1$ is the length of the laminations [m], and $h$ is the gap [m] between the laminations. Assuming that the gap ($h$) is much less than the length of the laminations ($R_1$), the equation becomes:

$$\Delta P \approx \gamma\left(-\frac{2cos\theta}{h}\right), for\ R_1 \gg h \tag{3.2}$$

Therefore, the capillary force that links the laminations is:

$$F = \frac{2\gamma cos\theta}{h} \cdot A \tag{3.3}$$

where $A$ is the area of the lamination [$m^2$]. Since the laminations are suspended from an assembly wire, the liquid polymer experiences a gravitational force expressed as:

$$F = \rho \cdot h \cdot A \cdot g \tag{3.4}$$

where $\rho$ is the density of the liquid [$kg/m^3$], and $g$ is the acceleration due to gravity, 9.8 $m/s^2$. Combining equations (3.3) and (3.4) determines the critical gap ($h_{crit}$), where the capillary force between the laminations and the gravitational force on the liquid are equal, and is expressed as:

$$h_{crit} = \sqrt{\frac{2\gamma cos\theta}{9.8\rho}} \tag{3.5}$$

This equation indicates that the laminations are not assembled in a self-aligned fashion if the gap between the laminations is too large (i.e., if the gravitational force on the liquid is greater than the capillary force between the laminations). In order to estimate the critical gap, contact angles of two liquid droplets (i.e., DI water and Novec 1700) on CoNiFe film were measured using a goniometer (CMA-Plus, TanTec) as shown in Figure 3.11. With additional properties shown in Table 3.3, the critical gaps for water and Novec 1700 become 1.44 mm and 1.19 mm, respectively.

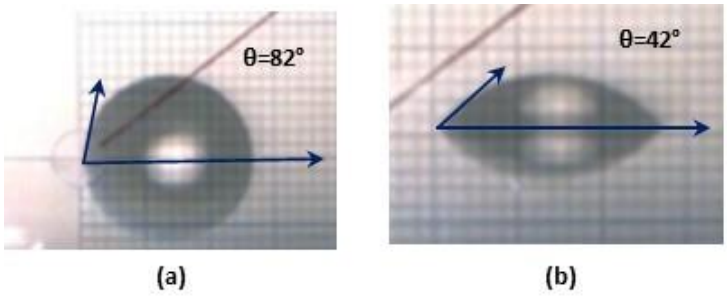


Figure 3.11 Measured contact angle of (a) DI water and (b) Novec 1700 polymer droplets on CoNiFe film.

Table 3.3 Properties of water and Novec 1700 at 23°C

| Property | Water | Novec 1700 [64] |
|---|---|---|
| Density [kg/m$^3$] | 998 | 1500 |
| Viscosity [cP] | 1 | 0.6 |
| Surface tension [mN/m] | 72.75 | 14 |
| Contact angle [Degree] | 82 | 42 |

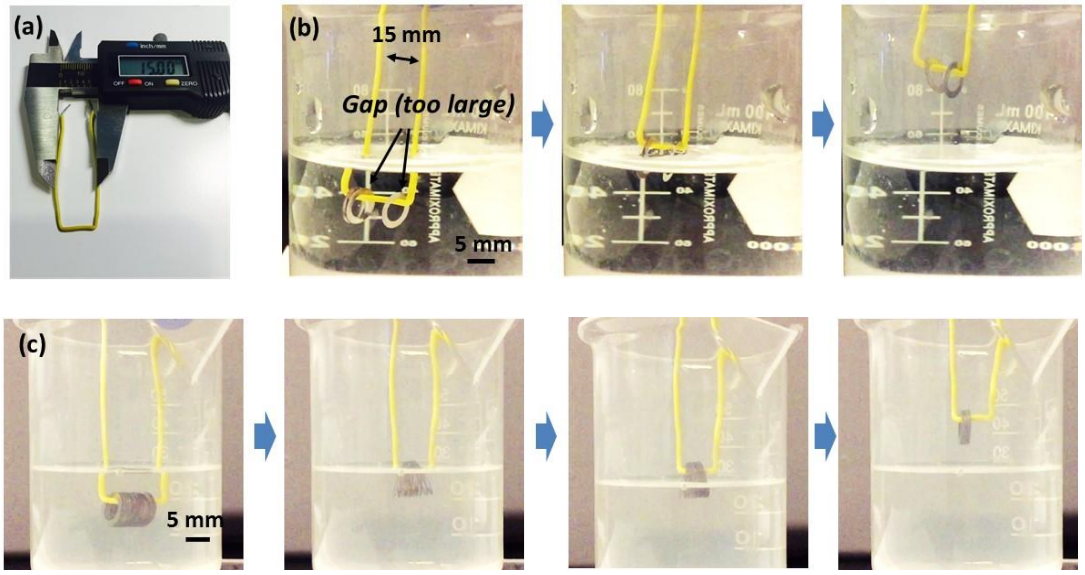


Figure 3.12 Assembly of CoNiFe sheets in a given length of 15 mm. (a) Wire with 15 mm width, (b) Failed assembly of 4 CoNiFe laminations in water due to a too large gap. (c) Successful assembly of 20 CoNiFe laminations in Novec 1700.

Performing the assembly technique with a controlled gap between the CoNiFe lamination could verify the analysis experimentally. However, it is challenging to adjust the gap precisely in the liquid. Alternatively, the assembly technique was performed with varying numbers of laminations in a given length (15 mm, Figure 3.12 (a)) of the assembly wire. In this case, the larger the number of laminations, the higher the possibility of possessing smaller gaps between the laminations. Figure 3.12 shows examples of the

performed assembly technique with varying numbers of laminations (2, 4, 7, 10, and 20 laminations) in a 15 mm space. Figure 3.12 (b) demonstrates an example of a failed assembly of 4 CoNiFe laminations in water due to a too large gap between the laminations. On the other hand, an example of a successful assembly of 20 CoNiFe laminations in Novec 1700 is shown in Figure 3.12 (c).

Since the experiment is probabilistic in nature, more than 70 assemblies were performed for each number of laminations, and a 'percentage of assembly' (i.e., probability of successful assembly into a single CoNiFe multilayer) was measured. The experimental result is shown in Figure 3.13, demonstrating that decreasing the average gap (i.e., increasing the number of laminations) results in a greater probability of successful assembly, as indicated by the theoretical analysis. A significant increase in the successful assembly percentage was observed between 1.5 mm (10 layers) and 0.75 mm (20 layers), which encompass the theoretical critical gap. Typically, a higher assembly percentage was observed when the assembly was performed in water, due to the higher surface tension and lower density of water than Novec 1700.

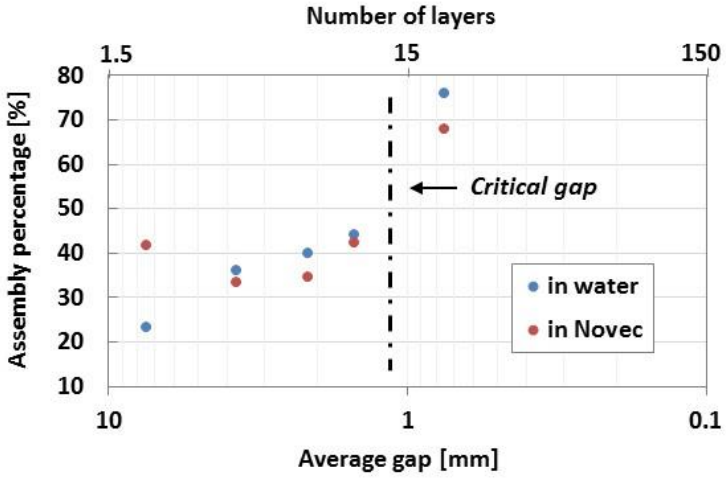


Figure 3.13 Assembly percentage with varying number of CoNiFe laminations in a 15 mm space.

### 3.4.3 Comparison of Two Fabrication Techniques (SU-8 Support Approach and Surface-tension-driven Assembly)

Table 3.3 compares the two fabrication techniques to develop nanolaminated magnetic cores (i.e., SU-8 support approach and Surface-tension-driven assembly). As described in Table 3.3, the surface-tension-driven assembly allows insulation of each individual magnetic layer. resulting in higher mechanical robustness then the SU-8 support approach. The surface-tension-driven approach allows not only fabrication ease, but also potentially unlimited achievable total core thickness by threading a desired number of CoNiFe/copper multilayer structures in a string.

Table 3.4 SU-8 support approach and surface-tension-driven assembly

| | | SU-8 support approach | Surface-tension-driven assembly |
|---|---|---|---|
| Core cross-section | Metallic film<br>SU-8<br>Polymeric material |  | 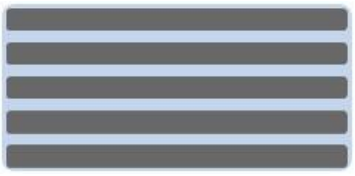 |
| Interlamination layer | | SU-8 and air | Insulating polymer |
| Packaging | | Additional packaging required (e.g., PDMS or PVA) | Co-packaging |
| Achievable total thickness | | Limited to photoresist mold thickness | Potentially unlimited |

## 3.5 Characterization of Nanolaminated Magnetic Cores

In order to characterize the performance of the nanolaminated magnetic cores, test inductors were prepared by placing the cores in laser-machined polymeric bobbins and winding them with wire as shown in Figure 3.14. For the fabrication of the bobbin, the 500-μm-thick polymeric sheet (Plastic Shim Stock, ARTUS) is first laser-scribed to from a toroidal trench at the center where the magnetic core can be securely placed. The trench

is slightly deeper than the core thickness and wider than the core outer diameter so that the released core structure does not collapse by subsequent manual coil winding. Then, a number of notches are cut along the periphery of the trench to provide the space for tight and reproducible winding without overlap.

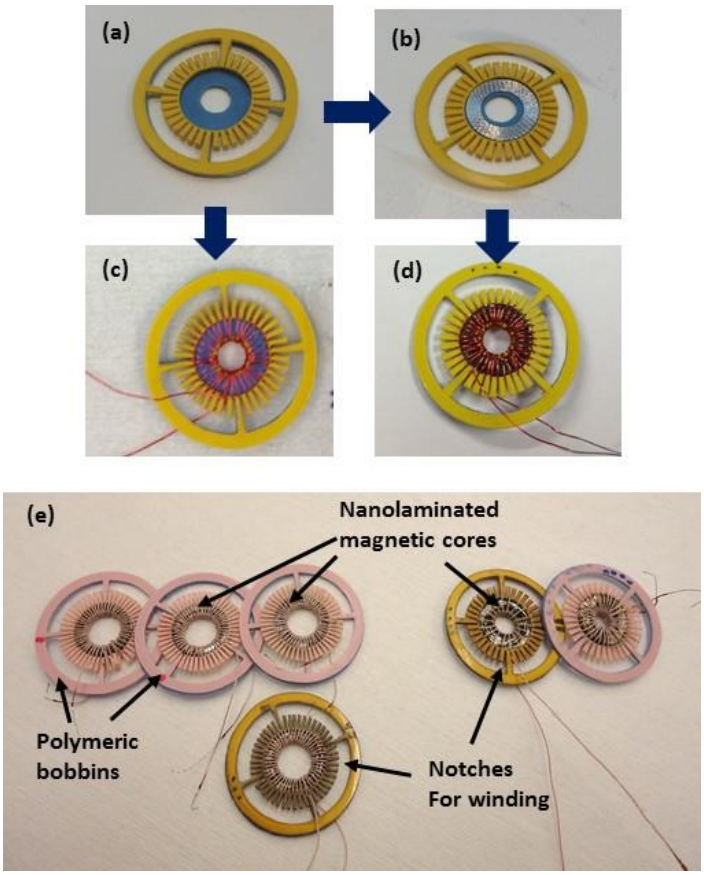


Figure 3.14 Test inductors. (a) – (d) Fabrication steps. (e) Image

The test inductor fabrication procedure consists of: 1) laser-micromachining of polymeric bobbin with desired number of notches for winding guide (Figure 3.14 (a)); 2) placing nanolaminated magnetic core in the bobbin (Figure 3.14 (b)); 3) winding the bobbin with wire (Figure 3.14 (d)). An air core inductor was also formed by winding the same bobbin without the magnetic core as shown in Figure 3.14 (c). The bobbin not only provides mechanical support for the nanolaminated core and winding, but also allows

reproducible windings through equally distributed notches. Figure 3.14 (e) shows fabricated test inductors with laminated magnetic cores packaged in polymer bobbins, wound by wire having 36 or 48 turns with Litz wire or magnet wire (Belden, AWG 8056).

Once the test inductors were prepared, three different types of characterizations were performed on the test inductors consecutively: 1) low flux *in situ* characterization using an impedance analyzer; 2) high flux characterization under large signal AC flux conditions; and 3) system level characterization in DC-DC converters. Each characterization was performed on both nanolaminated permalloy and CoNiFe cores with the same geometry, and the results from both cores are compared.

For the nanolaminated cores that are fabricated using the SU-8 support approach, it is the first priority to ensure the electrical isolation of each lamination for the reliable characterization of the nanolaminated cores, since it is challenging to visually ensure complete copper removal throughout the entire core structure. Note that the surface-tension-driven assembly ensures isolation of each lamination layers by the nature of the process, since the assembly process starts after the complete removal of copper.

For the nanolaminated cores fabricated by the SU-8 support approach, measuring frequency-dependent core inductance *in situ* during the sacrificial copper layer etch is an effective method to validate isolation of each magnetic lamination [62, 63]. This *in situ* measurement enables monitoring of inductance decrease as a function of frequency prior to the complete copper etch since the electrically connected magnetic layers form a bulk metallic core (~ 100 μm thickness) causing significant eddy-current flow. Consequently, one can conclude the complete isolation of each magnetic lamination when a constant inductance as a function of frequency is observed due to the suppressed eddy-currents in

nanolaminations. The low flux *in situ* measurement provides not only the validation of suppressed eddy-current losses but also estimation of complete copper etch time.

Once the constant inductance as a function of frequency is observed from the low flux *in situ* measurement, the next characterization stage is carried out on the test inductor under large signal AC flux conditions. Since magnetic metallic alloys possess higher saturation flux density than conventional ferrites, it is worthwhile to study the magnetic performance of nanolaminated magnetic cores under simultaneous high flux and high frequency (HFHF) conditions. The HFHF test enables not only the assessment of maximum magnetic flux handling capacity but also detailed analysis of the core losses by decomposition of the observed losses into hysteresis and eddy-current components.

Finally, the test inductor is investigated in an appropriate DC-DC converter system (e.g., output power, inductor current, and switching frequency) based on the two characterization stages (low flux and high flux characterization).

### 3.5.1 Low Flux Characterization

#### 3.5.1.1 In Situ Characterization of Nanolaminated Cores Fabricated by SU-8 Support Approach

For the *in situ* characterization on the nanolaminated cores fabricated by the SU-8 support approach, the inductance and quality factor of test inductors were assessed using an impedance analyzer (HP 4194A) prior to sacrificial copper layer etching, and subsequently at various times during the progression of the sacrificial layer etching, enabling assessment of the eddy-current suppression. Note that the measurements at various stages of sacrificial layer etching are performed by removing the test inductors from the etchant, immersing them in deionized (DI) water. Then, the test inductor is

returned to the etch solution for continued etching. Figure 3.15 shows the inductance and the quality factor from the nanolaminated magnetic cores before and after sacrificial copper layer removal from the nanolaminated magnetic cores. For the in situ characterization, a pre-measured inductance and resistance of an air core inductor (i.e., wound bobbin without magnetic core (Figure 3.14 (c)) of nominally identical geometry was subtracted from a measured inductance and resistance of a magnetic core inductor (i.e., wound bobbin with magnetic core (Figure 3.14 (d)); thus the results are solely attributable to the magnetic core performance.

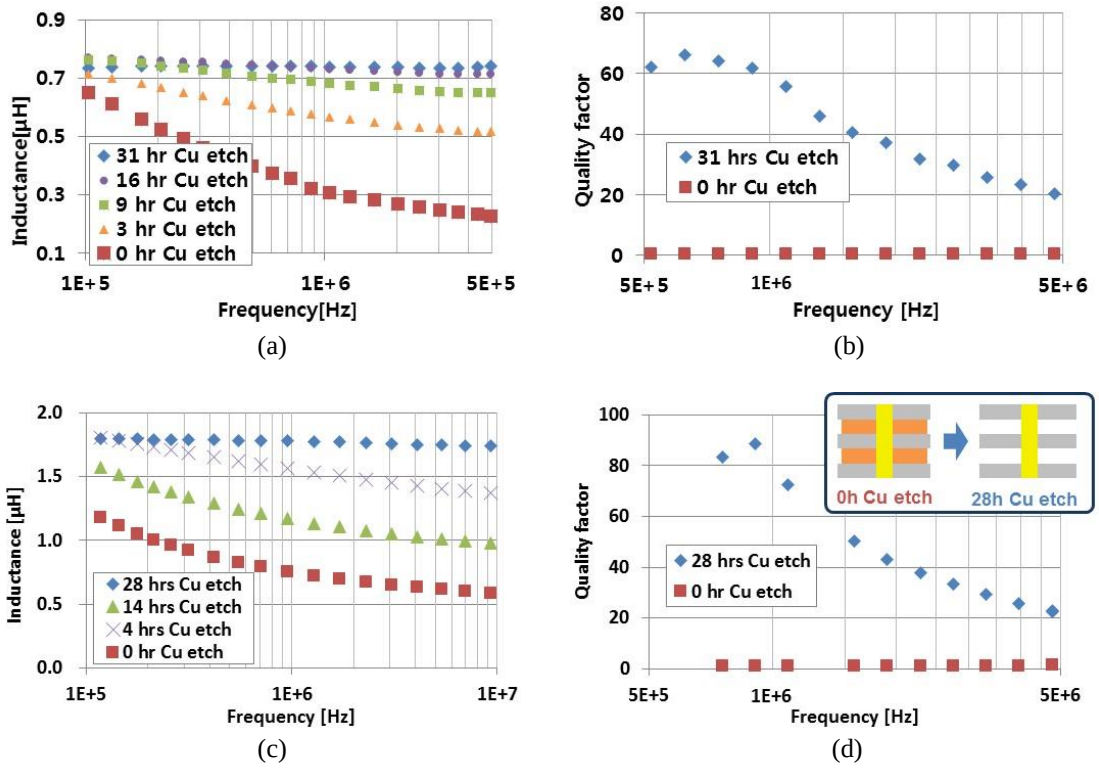


Figure 3.15 *In situ* characterization of nanolaminated magnetic cores. (a) Inductance and (b) Q factor of permalloy. (c) Inductance and (d) Q factor of CoNiFe.

Figure 3.15 (a) and (c) shows an example of measured inductance as a function of operation frequency parameterized by etching time. The test inductor possesses 36-turn windings around a nanolaminated magnetic cores having outer diameter of 10 mm and

inner diameter of 6 mm. Note that Figure 3.15 (a) and (b) represent a nanolaminated permalloy core and Figure 3.15 (c) and (d) represent a nanolaminated CoNiFe core.

Before sacrificial copper layers are etched (red dots in the graph), the nanolaminated magnetic core comprises 70 alternating pairs of 500-nm-thick magnetic material (i.e., permalloy or CoNiFe) and copper layers in which every layer is electrically connected, causing significant eddy current flow throughout the bulk metallic medium since the total core thickness exceeds the skin depth of the material in the measured frequency region. Consequently, a significant inductance decrease as a function of operation frequency is observed. However, each magnetic lamination is gradually isolated as the sacrificial copper layers are removed, so that eddy currents are mitigated. Upon complete isolation of each magnetic lamination (blue dots in the graph), constant inductance is observed as a function of operation frequency verifying the suppressed eddy-current losses in the 500-nm-thick magnetic laminations, which are thinner than the skin depth of the magnetic materials (~3 μm) at the frequency of 10 MHz. From the inductances in Figure 3.15 (a) and (c), it is demonstrated that the nanolaminated CoNiFe core possesses approximately 2 time higher inductance than the nanolaminated permalloy core, implying a higher effective permeability of CoNiFe than permalloy. Using equation (1.19), the effective permeabilities of the nanolaminated CoNiFe core and the nanolaminated permalloy core are 200 and 100, respectively.

Measured quality factor of the nanolaminated CoNiFe core after the sacrificial copper layers removal approaches 80 at 1 MHz, whereas the quality factor before the sacrificial copper layers removal is less than 2 in the measured frequency region. The nanolaminated permalloy core with the same geometry shows a quality factor approaching 60 at 1 MHz after complete removal of the sacrificial copper layer.

### 3.5.1.2 Low Flux Characterization of Nanolaminated Cores Fabricated by Surface-tension-driven Assembly

For nanolaminated CoNiFe core fabricated by the surface-tension-driven assembly, the in situ measurement is not necessary since the assembly process starts after the completion of entire copper removal. Figure 3.16 shows the inductance and quality factor of developed test inductors with nanolaminated CoNiFe cores fabricated using the surface-tension-driven assembly. Note that inductance and quality factor in the graph are attributed to the test inductor performance, meaning that the values are including areas not occupied by the nanolaminated CoNiFe cores.

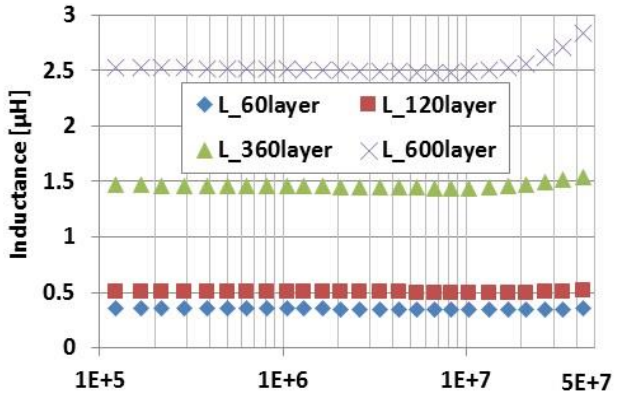


(a)

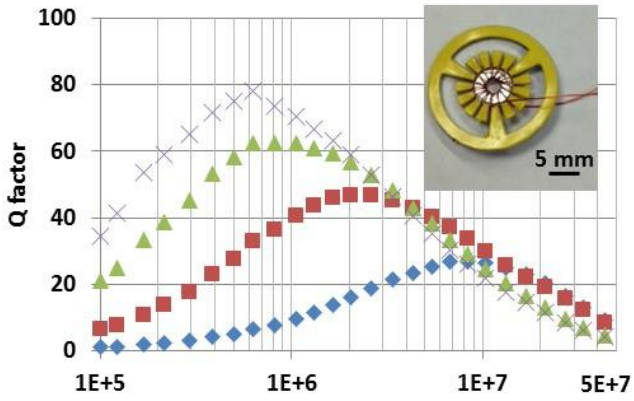


(b)

Figure 3.16 Characterization of test inductors with nanolaminated CoNiFe cores with varying number of laminations. (a) Inductance and (d) Q factor.

The test inductor has 15-turn windings as shown in the inset of Figure 3.16. The nanolaminated CoNiFe core has an outer diameter of 5.3 mm and inner diameter of 2.7 mm. Since the achievable number of laminations is potentially unlimited in the surface-tension-driven assembly, several nanolaminated CoNiFe cores with a varying number of 500-nm-thick CoNiFe laminations were prepared. Figure 3.16 (a) shows the inductances of test inductors with the nanolaminated CoNiFe cores, demonstrating a higher inductance with a larger number of laminations. Further, the inductance remained constant at operation frequencies up to 50 MHz, indicating suppressed eddy-current losses. Figure 3.16 (b) demonstrates that the peak quality factor of the inductor also increased with a larger number of laminations.

### 3.5.2 High Flux, High Frequency Characterization

Nanolaminated magnetic cores enable the fabrication of inductors operating in the MHz frequency range with exceptionally high operating flux density of 0.5 T, which is challenging to achieve with conventional ferrite. In order to characterize the superior performance of the nanolaminated magnetic cores, high flux and high frequency (HFHF) core loss measurements were performed using an LC resonant test setup based on series resonance between the test inductor and a reference capacitor [67]. A circuit diagram of the HFHF core loss characterization setup is shown in Figure 3.17. The inductor is modeled as a series connection of an ideal inductor with inductance of $L$ and two resistive components ($R_{core}$ and $R_{coil}$) that represent the copper and core losses of the inductor. The resistance ($R_c$) and the capacitance ($C$) of the resonant capacitor are pre-measured so as to resonate with the inductor at the desired measurement frequency. Note that a high quality

factor capacitor needs to be used so that the capacitor resistance ($R_c$) is negligible compared to $R_{core}$ and $R_{coil}$.

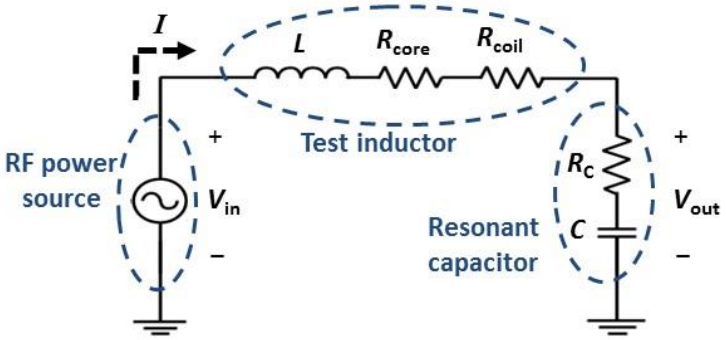


Figure 3.17 Schematic of the HFHF core loss characterization setup.

In the circuitry, the input voltage $V_{in}$ is a sinusoidal wave, generated by a signal generator and an rf power amplifier, and expressed as:

$$V_{in\_pk} = i_{pk} \cdot (jX_L + R_{core} + R_{coil} + jX_C + R_C) \tag{3.6}$$

where $X_L$ is the reactance of the inductor:

$$X_L = 2\pi f L \tag{3.7}$$

and $X_C$ is the reactance of the capacitor:

$$X_C = \frac{1}{2\pi f C} \tag{3.8}$$

The output voltage of the circuit becomes:

$$V_{out\_pk} = i_{pk} \cdot (jX_C + R_C) \tag{3.9}$$

In order to understand how the circuit enables core loss measurement, the resonant frequency ($f_s$) of the circuit must be considered:

$$f_s = \frac{1}{2\pi\sqrt{LC}} \tag{3.10}$$

The inductive reactance ($X_L$) and the capacitive reactance ($X_C$) are the same at the resonance ( $1/\omega_s C = \omega_s L$), and the capacitor resistance ($R_c$) can be negligible when high

quality factor is used ($R_c$ << $R_{core}$ and $R_c$<<$R_{coil}$). Hence, the ratio between the peak output voltage ($V_{out\_pk}$) and the peak input voltage ($V_{in\_pk}$) amplitude becomes the quality factor of the test inductor:

$$\frac{V_{out\_pk}}{V_{in\_pk}} = \left| \frac{R_c + \frac{1}{j\omega_s C}}{R_{core} + R_{coil} + R_c} \right| \approx \frac{\omega_s L}{R_{core} + R_{coil}} = Q_L \tag{3.11}$$

Then, the resistance of the core ($R_{core}$) is obtained by:

$$R_{core} = \frac{\omega_s L}{Q_L} - R_{coil} \tag{3.12}$$

where $R_{coil}$ is the resistance of the inductor coil [Ω] which was pre-measured.

The peak current through the circuit is calculated from the measured peak output voltage and the capacitor:

$$i_{pk} = V_{out\_pk} \cdot 2\pi f_s C \tag{3.13}$$

Thus, the power losses of the core is estimated by:

$$P_{core\_pk} = I_{pk}^2 \cdot R_{core} \tag{3.14}$$

The peak sinusoidal flux density within the core is estimated from the voltage across the secondary pick-up coil of the inductor using Faraday`s law of induction:

$$B_{pk} = \frac{V_{pickup\_pk}}{2\pi f_s N A_c} \tag{3.15}$$

where $V_{pickup\_pk}$ is the peak voltage [V] from the secondary pick-up coil, $N$ is the number of the secondary pick-up winding, and $A_c$ is the core cross-section area [$m^2$]. Therefore, by changing the capacitance (thereby the resonant frequency), one can characterize the core loss as functions of operating frequency and peak flux density as shown in Figure 3.18.

During the measurement, the amplitude and the frequency of a sinusoidal input voltage, generated by a signal generator (Agilent 33120A) and an RF power amplifier (BT00500-AlphaS, TOMCO), are precisely modulated to resonate the circuit at the desired

flux density within the core. The output voltage from the reference capacitor is monitored by an oscilloscope (Tektronix TDS 2024C). It should be noted that premeasured resistances of the resonant capacitor, experimental PCB, and an air core inductor of nominally identical geometry were determined at the same frequency in this high flux characterization. These premeasured values were subtracted from the resistance of the test inductors with the nanolaminated magnetic cores during the measurement so that the presented volumetric power losses are attributable to the core material alone.

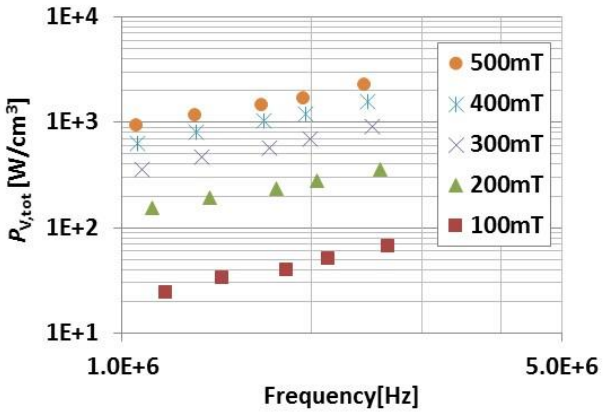


(a)

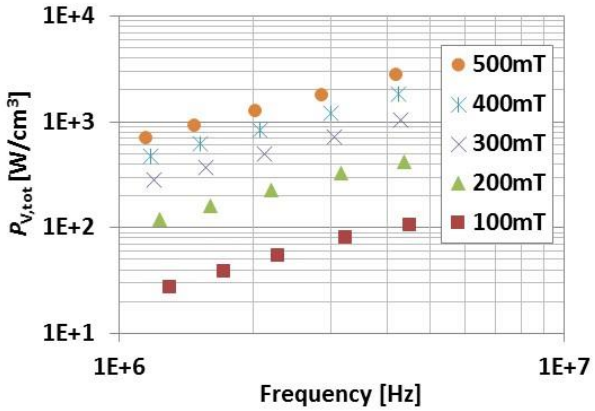


(b)

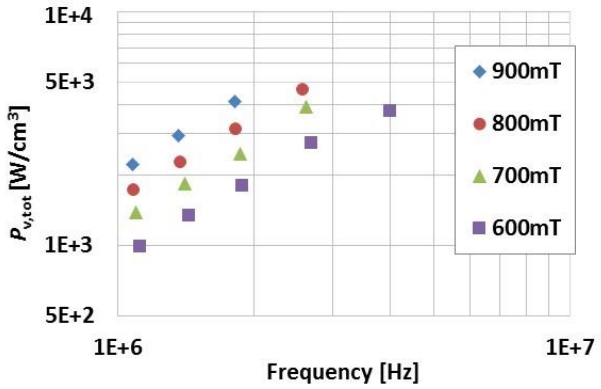

(c)

Figure 3.18 Measured power loss per unit volume at high peak flux densities at low MHz frequency. (a) permalloy, (b) and (c) CoNiFe

Figure 3.18 shows measured total volumetric power losses ($P_{v,tot}$) at high peak flux densities in the 1-5 MHz frequency range from nanolaminated magnetic cores comprising 70 layers of 500-nm-thick laminations in 36-turn test inductors. From Figure 3.18 (a) and (b), it is observed that the CoNiFe core exhibits lower volumetric power loss density than the permalloy core at the same operation frequency and flux density. Further, the nanolaminated CoNiFe core was operated up to peak flux density of 0.9 T as shown in Figure 3.18 (c), which is challenging to achieve with the nanolaminated permalloy core due to its intrinsic magnetic property (i.e., low saturation flux density). During high flux operation, the temperature variation of the cores was measured using an infrared thermometer. Negligible temperature increase from both cores was observed up to operation peak flux density of 0.3 T without any thermal cooling. Also without thermal cooling, the temperature increase reached 50 ℃ at 0.4 T flux level. Above this flux level, convective cooling was employed during the highest operation peak fluxes over 0.5 T where the core temperature reached 100 ℃, implying that appropriate thermal cooling (e.g.,

convective cooling or heat sinking) may be required for the highest peak flux level operation.

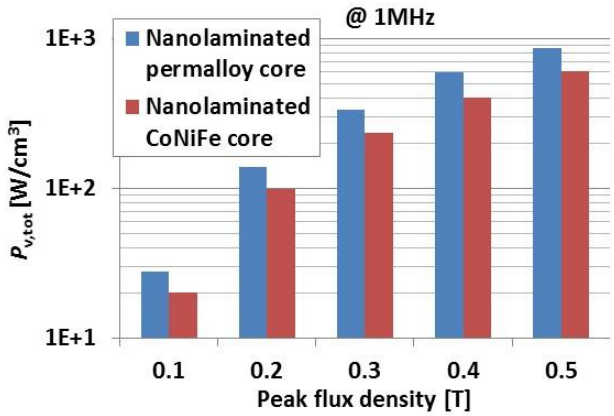


Figure 3.19 Volumetric power losses of a nanolaminated permalloy and CoNiFe cores at 1 MHz as a function of flux density. Note that y-axis is in log-scale.

In order for the direct comparison of the performance of the nanolaminated permalloy and the CoNiFe cores, volumetric power losses of both cores at 1 MHz as a function of peak flux density levels ranging from 0.1 T to 0.5 T are plotted in Figure 3.19. Note that both cores comprise 70 layers of 500 nm-thick-laminations with the same geometry. As shown in the graph, the nanolaminated CoNiFe core exhibits approximately 30% lower total power loss density than the nanolaminated permalloy core at the high flux densities mainly due to the advanced intrinsic properties of the CoNiFe material (lower coercivity).

### 3.5.3 Decomposition of Magnetic Losses

In order for further analyze on the measured magnetic losses, decomposition of the magnetic losses into hysteresis losses and eddy-current losses has been performed. The distribution of electric fields, magnetic fields, and eddy currents in the magnetic core can

be analytically modeled for a rectangular lamination (Figure 3.20) under sinusoidal excitation.

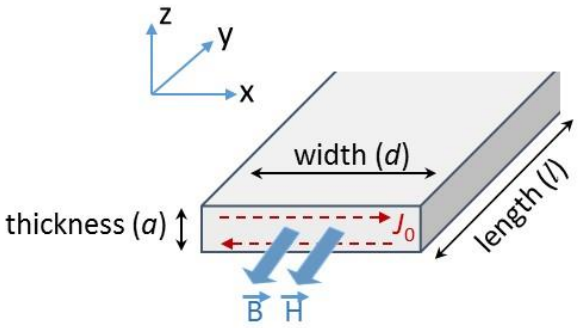


Figure 3. 20 Schematic of analytically modeled magnetic lamination of thickness *a*, width *d*, and length *l*.

Equations for hysteresis losses and eddy-current losses (i.e., the two dominant losses mechanisms) are developed based on the Poynting theorem, which considers conservation of energy for the electromagnetic field in the form of a partial differential equation [10]. In general, the following assumptions need to be considered to find analytical solutions of magnetic core losses: 1) the magnetic core material is assumed to be linear, isotropic, and homogeneous, resulting in a constant conductivity ($\sigma$) and permeability ($\mu$); 2) the length of the magnetic lamination in much larger than either of its cross-sectional dimensions; 3) the cross-sectional thickness is much smaller than the cross-sectional width. With the assumptions, the fringing field at the edges of the lamination can be neglected, and the curl form of Maxwell's equations become:

$$\nabla \times \vec{E}(t) = -\frac{\partial \vec{B}(t)}{\partial t} \tag{3.12}$$

$$\nabla \times \vec{H}(t) = \vec{J}(t) \tag{3.13}$$

where $\vec{E}$ is the electric field, $\vec{B}$ is the magnetic flux density, $\vec{H}$ is the magnetic field, and $\vec{J}$ is the current density. When the divergence of the Poynting vector ($\vec{S}(t) = \vec{E}(t) \times \vec{H}(t)$ ) is integrated over the enclosed volume, it is expressed as:

$$\int_V \nabla \cdot \left[\vec{E}(t) \times \vec{H}(t)\right] dV = -\int_V \left[\vec{H}(t) \cdot \frac{\partial \vec{B}(t)}{\partial t} + \vec{E}(t) \cdot \vec{J}(t)\right] dV \qquad (3.14)$$

The left side of equation (3.14) represents the energy flow into the volume per unit time, while the right side of the equation represents the energy stored and dissipated per unit time. Then the energy flow into the stationary volume between two points of time $t_1$ and $t_2$ becomes:

$$W = \int_{t1}^{t2} \int_V \left[\vec{H}(t) \cdot \frac{d\vec{B}(t)}{dt} + \vec{E}(t) \cdot \vec{J}(t)\right] dV\, dt = \int_V \left[\int_{B1}^{B2} H dB + \int_{t1}^{t2} \frac{J^2(t)}{\sigma} dt\right] dV \quad (3.15)$$

where $B_1$ and $B_2$ are the flux densities corresponding to $t_1$ and $t_2$, respectively. Over a complete B-H loop cycle, the first term represents the hysteresis loss. The second term represents the eddy-current loss. Thus, the total loss or core loss is

$$P_{core} = P_{hyst} + P_{eddy} \qquad (3.16)$$

where $P_{\text{hyst}}$ is the hysteresis loss and $P_{\text{eddy}}$ is the eddy-current loss.

### 3.5.3.1 Analytic Model for Eddy-current Loss

In order to calculate the core loss, the current and field distribution within the volume of the material must be known by solving a differential equation in the quantity of interest. In Maxwell`s equations, the curl of magnetic field is expressed as:

$$\nabla \times \vec{H}(t) = \sigma \vec{E}(t) \qquad (3.17)$$

Taking the curl of the equation and combining with equation (3.12) yields:

$$-\nabla^2 \vec{H}(t) + \nabla\left[\nabla \cdot \vec{H}(t)\right] = -\sigma \frac{\partial \vec{B}(t)}{\partial t} \qquad (3.18)$$

Under the assumptions outlined in section 1.2.4 of this thesis, the above equation can be written as:

$$\nabla^2 \vec{B}(t) = \sigma\mu \frac{\partial \vec{B}(t)}{\partial t} \tag{3.19}$$

where $\mu = \mu_0 \cdot \mu_r$. When the field is applied to the surface of the lamination, the induced eddy currents flow as indicated in Figure 3.17. By a similar derivation, the relation between the space and time derivatives of current density at any point in a conductive lamination is:

$$\nabla^2 \vec{J}(t) = \sigma\mu \frac{\partial \vec{J}(t)}{\partial t} \tag{3.20}$$

Introducing the complex exponential form to the sinusoidal current $\vec{J}(t)$ yields:

$$\vec{J}(t) = Re\{\vec{J} e^{j\omega t}\} \tag{3.21}$$

Then, equation (3.20) is expressed as:

$$\nabla^2 \vec{J}(t) = j\omega\sigma\mu\vec{J} \tag{3.22}$$

where $\nabla^2$ is the Laplace operator (in Cartesian coordinates):

$$\nabla^2 = \frac{\partial^2}{\partial x^2} + \frac{\partial^2}{\partial y^2} + \frac{\partial^2}{\partial z^2} \tag{3.23}$$

In the lamination in Figure 3.17 where the width is much larger than the thickness, the following symmetry and boundary conditions are assumed:

$$J_y = 0 \tag{3.24}$$

$$J_z = 0 \tag{3.25}$$

$$\frac{\partial J_x}{\partial x} = \frac{\partial^2 J_x}{\partial x^2} = 0 \tag{3.26}$$

$$\frac{\partial J_x}{\partial y} = \frac{\partial^2 J_x}{\partial y^2} = 0 \tag{3.27}$$

$$J_x|_{z=\left(\frac{a}{2}\right)} = J_0 \tag{3.28}$$

$$J_x|_{z=\left(-\frac{a}{2}\right)} = -J_0 \tag{3.29}$$

With the above boundary conditions, the current flows only in the x-direction and the current distribution equation (3.20) becomes:

$$\frac{d^2 J_x}{dz^2} = j\omega\sigma\mu J_x = T^2 J_x \tag{3.30}$$

where *T* is a constant and is written as:

$$T = \sqrt{j\pi f\mu\sigma} = (1+j)\sqrt{\pi f\mu\sigma} = \frac{1+j}{\delta} \tag{3.31}$$

where $\delta$ is the skin depth.

The differential equation can be expressed in terms hyperbolic functions:

$$J_x = A\sinh Tz + \mathrm{C}\cosh Tz \tag{3.32}$$

Solving the equations with the boundary conditions (equations 3.28 and 3.29) results in:

$$\mathrm{C} = 0 \tag{3.33}$$

$$\mathrm{A} = \frac{J_0}{\sinh T\frac{a}{2}} \tag{3.34}$$

Therefore the current density in the x-direction is:

$$J_x = J_0 \frac{\sinh T_z}{\sinh T\frac{a}{2}} = J_0 \frac{\sinh(\frac{1+j}{\delta})\mathrm{z}}{\sinh(\frac{1+j}{\delta})\frac{a}{2}} \tag{3.35}$$

where *a* is the thickness of the lamination.

Taking the absolute value of the current density gives:

$$|J_x| = |J_0| \left| \frac{\sinh\frac{z}{\delta}\cos\frac{z}{\delta} + j\cosh\frac{z}{\delta}\sin\frac{z}{\delta}}{\sinh\frac{a}{2\delta}\cos\frac{a}{2\delta} + j\cosh\frac{a}{2\delta}\sin\frac{a}{2\delta}} \right| = |J_0| \left( \frac{\sinh^2\frac{z}{\delta} + \sin^2\frac{z}{\delta}}{\sinh^2\frac{a}{2\delta} + \sin^2\frac{a}{2\delta}} \right)^{1/2} \tag{3.36}$$

For the thin lamination, where $a/2\delta << 1$ and $x/\delta << 1$:

$$|J_x| = |J_0| \frac{z}{\left(\frac{a}{2}\right)} \tag{3.37}$$

The current distribution is linear with *z*-direction and $J_0$ needs to be evaluated. Using Faraday`s line integral and integrating around the cross-sectional area in Figure 3.17 yields:

$$\oint \vec{E}(t)_0 \cdot \vec{d}d = -\frac{d\Phi(t)}{dt} \tag{3.38}$$

where *d* is the width of the cross-section and $\Phi(t)$ is the total flux within the cross-section. Multiplying both sides by conductivity yields:

$$\oint \vec{j}(t)_0 \cdot \vec{d}l = -\sigma\frac{d\Phi(t)}{dt} \tag{3.39}$$

Since the lamination has a width of *d* that is much larger than the thickness (*a*), the current density ($J_0$) in complex notation form is:

$$J_0 = \frac{j\omega\sigma\Phi}{2d} \tag{3.40}$$

The absolute value becomes:

$$|J_0| = \frac{\omega\sigma|\Phi|}{2d} \tag{3.41}$$

Hence, the current density in the *x*-direction becomes:

$$|J_x| = \frac{\omega\sigma|\Phi|}{2l}\left(\frac{\sinh^2\frac{z}{\delta}+\sin^2\frac{z}{\delta}}{\sinh^2\frac{a}{2\delta}+\sin^2\frac{a}{2\delta}}\right)^{1/2} \tag{3.42}$$

Combining with equation (1.27), the eddy-current loss in the lamination in Figure 3.17 can be expressed as:

$$P_{eddy} = \int_V \frac{J^2(t)}{2\sigma}dV = 2\int_0^{\frac{a}{2}}\frac{J^2(t)}{2\sigma}dl\,dx = \frac{\omega^2|\Phi|^2\sigma l\delta}{8d}\left(\frac{\sinh\frac{a}{\delta}-\sin\frac{a}{\delta}}{\cosh\frac{a}{\delta}-\cos\frac{a}{\delta}}\right) \tag{3.43}$$

If the lamination thickness is less than the skin depth ($a << \delta$), the eddy-current power loss becomes:

$$P_{eddy} = \frac{\omega^2\Phi^2\sigma la}{24d} \tag{3.44}$$

Since $B$ is assumed to be uniform with frequency, the average power per unit volume yields:

$$P_{V,eddy} = \frac{\pi^2 f^2 B^2 a^2 \sigma^2}{6} \tag{3.45}$$

### 3.5.3.2 Analytic Model for Hysteresis Loss

In the analysis of hysteresis losses, the flux density distribution must be known. This can be found from the current density expression. Using the complex exponential form of $\vec{B}$ and $\sigma\vec{E} = \vec{J}$, equation (1.24) can be expressed as:

$$\nabla \times \vec{J}(t) = -j\omega\sigma\vec{B} \tag{3.46}$$

Since $J_x$ is the only component of $\vec{J}$, it can be written as:

$$-\frac{\partial J_x}{\partial z} = -j\omega\sigma B_y \tag{3.47}$$

Combined with equation (3.35), the flux density becomes:

$$B_y = -\frac{j}{\omega\sigma}\frac{\partial}{\partial z}\left(J_0 \frac{\sinh Tz}{\sinh T\frac{a}{2}}\right) = \frac{\Phi T}{2b}\left(\frac{\cosh Tz}{\sinh T\frac{a}{2}}\right) \tag{3.48}$$

The absolute value is:

$$\left|B_y\right| = \frac{\sqrt{2}|\Phi|}{2d\delta}\left(\frac{\cos^2\frac{z}{\delta}+\sinh^2\frac{z}{\delta}}{\sin^2\frac{a}{2\delta}+\sinh^2\frac{a}{2\delta}}\right)^{1/2} \tag{3.49}$$

From equation (3.15), we know that the hysteresis energy loss over a full cycle of hysteresis loop becomes:

$$P_{hyst}(per\ cycle) = \int_V \left[\oint (H\ dB)\right] dV = \int_V \frac{2B^2 S}{\mu} dV \tag{3.50}$$

where $B$ is the operation flux density and $S$ is the shape factor that depends on the shape of the hysteresis loop [10]. With the volume of the laminated core as shown in Figure 3.17, the hysteresis loss for one cycle is expressed:

$$P_{hyst}(per\ cycle) = 4dl\int_0^{a/2}\frac{B^2S}{\mu}dz \tag{3.51}$$

Note that $S$ and $\mu$ are assumed to be constant.

Combined with equation (3.49) and by noting that $|B_y| = B$, the hysteresis loss becomes:

$$P_{hyst}(per\ cycle) = \frac{2dlS}{\mu}\left(\frac{|\Phi|}{d\delta}\right)^2\frac{1}{sinh^2\frac{a}{2\delta}+sin^2\frac{a}{2\delta}}\int_0^{\frac{a}{2}}\left(cos^2\frac{z}{\delta}+sinh^2\frac{z}{\delta}\right)dz =$$

$$\frac{lS|\Phi|^2}{\mu d\delta}\left(\frac{\sinh\frac{a}{\delta}+\sin\frac{a}{\delta}}{\cosh\frac{a}{\delta}-\cos\frac{a}{\delta}}\right) \tag{3.52}$$

The hysteresis loss at a given frequency becomes:

$$P_{hyst} = \frac{flS|\Phi|^2}{\mu b\delta}\left(\frac{\sinh\frac{a}{\delta}+\sin\frac{a}{\delta}}{\cosh\frac{a}{\delta}-\cos\frac{a}{\delta}}\right) \tag{3.53}$$

When the lamination thickness is less than the skin depth ($a<<\delta$), the hysteresis loss becomes:

$$P_{hyst} = \frac{2flS\Phi^2}{\mu da} \tag{3.54}$$

Since $B$ is assumed to be uniform with frequency, the average power per unit volume yields:

$$P_{V,hyst} = \frac{2fSB^2}{\mu} \tag{3.55}$$

Therefore, for the laminated magnetic core where the single lamination thickness is less than the skin depth, the total volumetric power loss can be expressed:

$$P_{V,tot} = P_{V,hyst} + P_{V,eddy} = \frac{2fSB^2}{\mu} + \frac{\pi^2f^2B^2a^2\sigma^2}{6} \tag{3.56}$$

### 3.5.3.3 Decomposition of Measured Magnetic Loss

One of the well-known core loss models is the Steinmetz equation [68], which represents the core loss with sinusoidal flux density of varying magnitude and frequency in the form of:

$$P_{V,tot} = kf^{\alpha}B^{\beta} \tag{3.57}$$

where $k$, $\alpha$, and $\beta$ is the empirical material parameters (e.g., $1< \alpha <2$, and $2< \beta <3$ for ferrite).

After the Steinmetz equation, various models have been proposed for corrections and modification [69 - 75]. One standard method of analyzing core loss in more detail is to break it up into static hysteresis loss, classical eddy current loss, and excess (anomalous) loss in the form of:

$$P_{V,tot} = P_{V,hyst} + P_{V,eddy} + P_{V,ex} = k_h f B^n + k_e f^2 B^2 + k_{ex} f^{1.5} B^{1.5} \tag{3.58}$$

The origin of the excess loss can be well understood by describing the magnetization dynamics in terms of a random distribution of magnetic correlation regions (i.e., groups of interacting domain walls).

Although anomalous losses are ignored in equation (3.56), their effects will be distributed among the losses attributed to eddy currents and hysteresis, meaning that the losses measured by this technique are conservative estimates of the true losses due to eddy currents and hysteresis. Therefore, it can be implied from the equation that in the "thin" lamination regime where the thickness of lamination ($a$) is well-below the skin depth ($\delta$), both eddy current and hysteresis losses become functions of frequency-squared and frequency, respectively.

$$P_{V,eddy} \propto f^2 \text{ and } P_{V,hyst} \propto f \tag{3.59}$$

This analytical modeling shows that eddy current losses and hysteresis losses are distinguishable from each other in the thin lamination regime by analyzing the core losses as a function of frequency. Because the lamination thicknesses of the developed cores are 0.3 - 1 μm thick which are thinner than the skin depth (e.g., 3μm at 10 MHz), the core loss mechanisms of developed laminated cores can be interpreted as being within the thin lamination regime.

As a result, total power loss per unit volume ($P_{V,tot}$) can be written as:

$$P_{V,tot} = P_{eddy} + P_{hyst} = k_{eddy}f^2 + k_{hyst}f \tag{3.60}$$

where $k_{eddy}$ is the eddy current power loss density coefficient and $k_{hyst}$ is the hysteresis power loss density coefficient. Consequently, by plotting $P_{Vtot}/f$ as a function of frequency, the coefficients ($k_{eddy}$ and $k_{hyst}$) can be extracted from the graph's slope and intercept, respectively.

Figure 3.21 shows $P_{V,tot}/f$ of the nanolaminated magnetic cores as a function of frequency parameterized by operation peak flux densities. The linear fitting lines are extracted from measured data of each peak flux density showing nearly zero-degree slopes. Also, both coefficients ($k_{eddy}$ and $k_{hyst}$) indicate that volumetric eddy-current losses are much lower than volumetric hysteresis losses, demonstrating that the eddy currents are suppressed in the nanolaminations of the cores at the measured high frequencies and high flux densities.

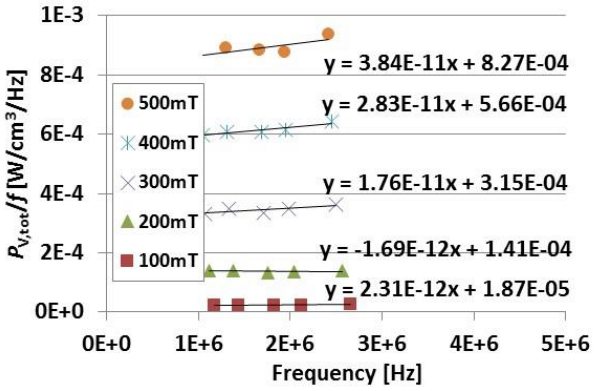


(a)

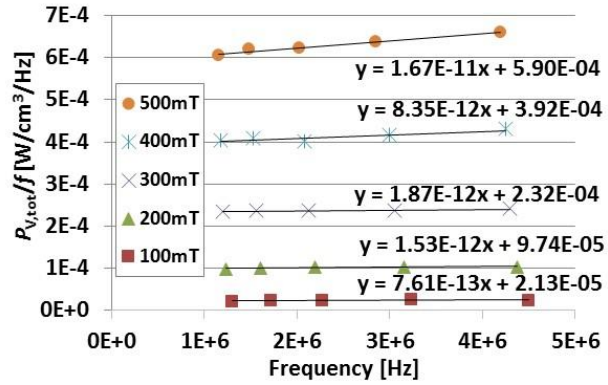


(b)

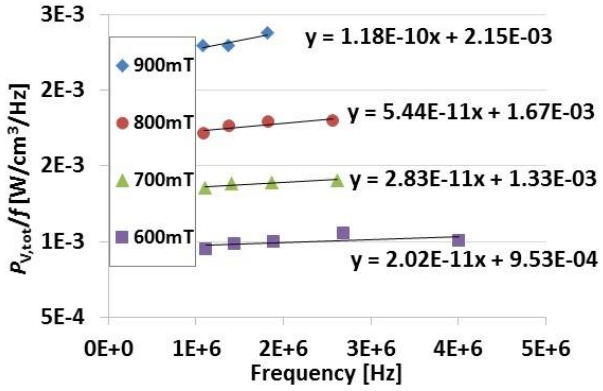


(c)

Figure 3.21 Measured power loss per unit volume over operation frequency up to 0.5 T flux density. (a) permalloy, (b) and (c) CoNiFe.

Figure 3.22 shows total volumetric power losses divided into hysteresis and eddy-current losses at 1 MHz as a function of peak flux density, demonstrating that the total power losses are dominated by hysteresis losses while eddy-current losses are suppressed

to approximately 1 - 3 % of the total losses. Note that volumetric eddy-current losses at lower peak flux densities (e.g., 0.1 - 0.3 T) are hardly seen in the graph, meaning that the eddy-current losses are suppressed to a negligible level. In order to further evaluate the correlation between the total volumetric power losses of the nanolaminated magnetic cores with operation peak flux density, a $B_{peak}$^2 fitting line is also plotted, demonstrating that measured volumetric power losses at 1 MHz correspond with a $B_{peak}$^2 line.

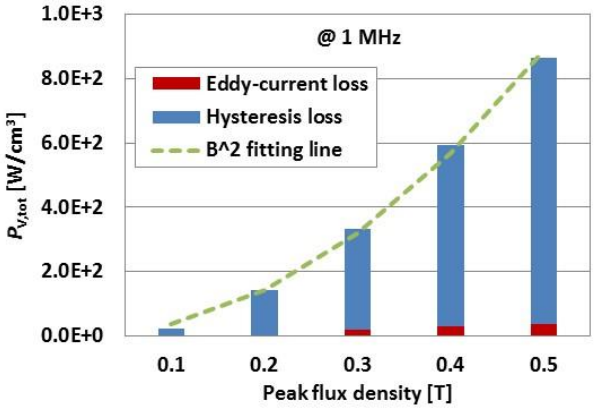


(a)

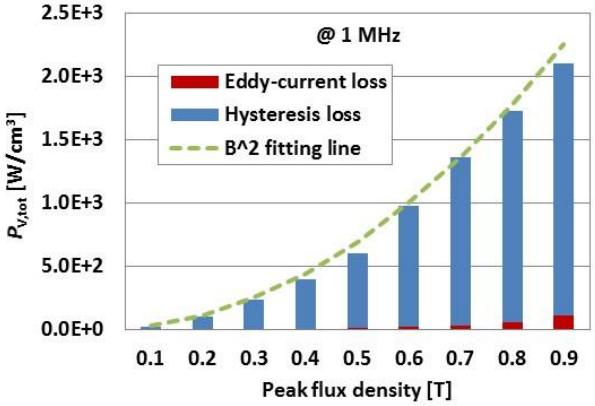


(b)

Figure 3.22 Comparison of eddy-current loss with hysteresis loss at 1 MHz as a function of flux density. (a) permalloy and (b) CoNiFe

For comparison, characteristics (e.g., saturation flux density and volumetric power loss) of several commercial MnZn ferrites that can be operated at low MHz frequency are presented in Table 3.5. These materials exhibit lower volumetric power losses than the

nanolaminated CoNiFe core (5.03 W/cm$^3$ at 0.05 T peak flux density and 1 MHz frequency). Although these losses are lower than that of the CoNiFe cores at these relatively low flux densities, achieving ultracompactness in inductors and converters requires operation at much higher flux densities. The demonstrated operation peak flux density of the nanolaminated CoNiFe core of up to 0.9 T exceeds not only the operating flux density, but also the saturation flux density, of these ferrites.

Table 3.5. Properties of commercial ferrites.

| Product | $P_{vol}$ [W/cm$^3$] (0.05 T, 1 MHz) | Bs [T] | Hc [Oe] | $\mu_i$ | $\rho$ [Ω·m] |
|---|---|---|---|---|---|
| 3F35 [76] | 0.7 | 0.5 | N/A | 1400 | 10 |
| 3F45 [77] | 0.3 | 0.42 | N/A | 900 | 10 |
| N59 [78] | 0.51 | 0.46 | 0.8 | 850 | 25 |
| N49 [78] | 0.56 | 0.46 | 0.7 | 1300 | 11 |
| PC95 [79] | 3.8 (0.1 T, 1 MHz) | 0.53 | 9.5 | 3300 | 6 |
| TP5B [80] | 0.6 | 0.5 | N/A | 1000 | 9 |

### 3.5.4 System Level Characterization

The fabricated inductor with nanolaminated magnetic cores have been tested in a DC-DC converter with switching frequencies in the MHz range. The LM3103 step down evaluation board from TI was selected as a testbed. A diagram of the evaluation board as well as typical component values can be found in [81]. By modifying the resistor that sets the switching frequency, and by replacing the commercial inductor by a low-profile, 36-turn test inductor with a nanolaminated magnetic core consisting of 70 layers of 500-nm-thick magnetic laminations (Figure 3.23), the converter operates at switching frequencies above 1 MHz with output power up to 8 W. During the measurement, input voltages are higher than 10 V, and output voltage is fixed at 7 V.

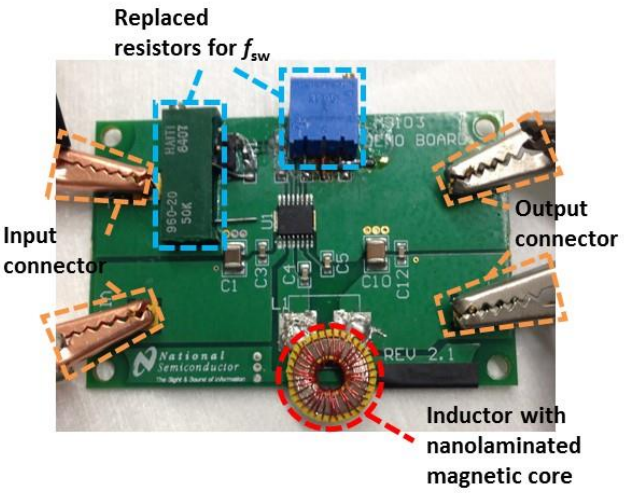


Figure 3.23 Image of a DC-DC converter evaluation board with a 36-turn inductor with nanolaminated magnetic core

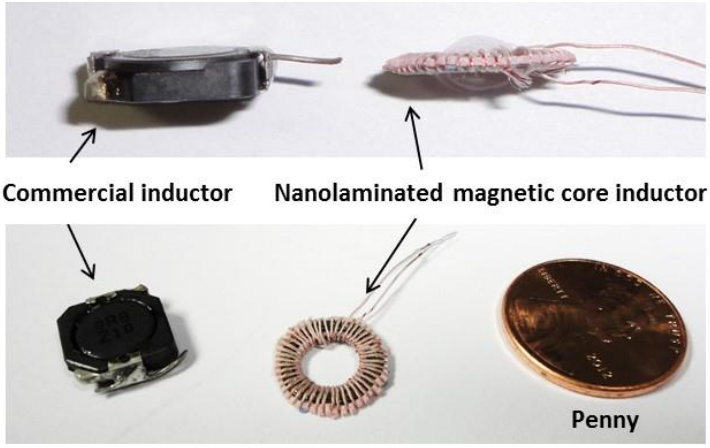


Figure 3.24 Comparison of commercial inductor and a nanolaminated core inductor with penny. (a) Side view and (b) inclined top view.

Figure 3.24 is an image of a commercial inductor and the nanolaminated magnetic core inductor of similar inductance value of 1 μH. For comparison, the volume of the nanolaminated magnetic core inductor even including non-optimized Litz wire winding is approximately 90 $mm^3$, whereas the packaged commercial inductor volume measured 260 $mm^3$, indicating the large inductor size reduction enabled by the nanolaminated magnetic core technology. The smaller volume of the nanolaminated magnetic core is

achieved mainly due to the higher saturation flux density and permeability of the magnetic metallic alloys. Also, greater power density can be achieved with the nanolaminated magnetic core since the operating flux density can be higher than that of commercial ferrite. The volume of the nanolaminated magnetic core itself is 1.5 $mm^3$.

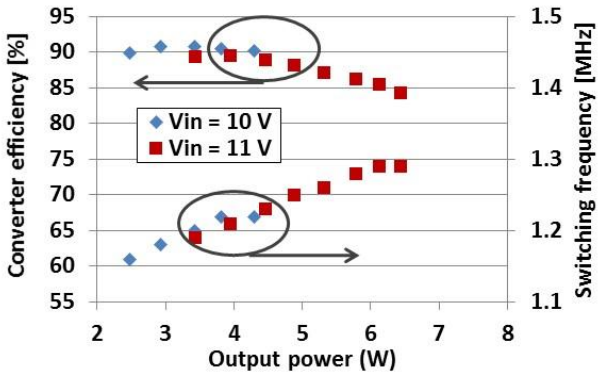


(a)

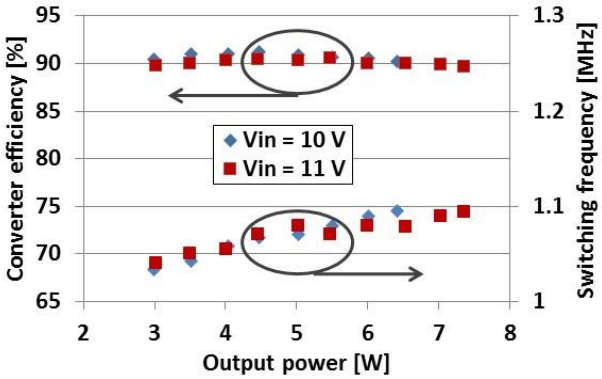


(b)

Figure 3.25 Converter efficiency and switching frequency as a function of output power. Experimental measurements of dc-dc power converter performance tested with (a) nanolaminated permalloy core and (b) nanolaminated CoNiFe core inductor

Figure 3.25 shows the converter efficiency and switching frequency of the selected converter with the test inductors as a function of output power. As shown in Figure 3.22 (a), the efficiency of the power converter operated with the nanolaminated permalloy core inductor is approximately 90% at output power of 4 W, but tends to decrease with

increasing output power. When the converter operates with nanolaminated CoNiFe core inductor, however, the efficiency is maintained at approximately 90% up to an output power of 7.5 W as shown in Figure 3.25 (b). The operation peak flux density of the nanolaminated magnetic cores reaches 0.4 T during the measurement which would be challenging to achieve with conventional ferrite cores.

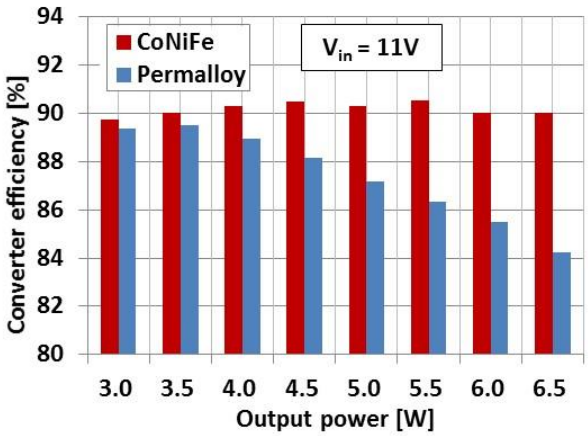


Figure 3.26 Comparison of power converter performance tested with a nanolaminated permalloy core inductor and a nanolaminated CoNiFe core inductor. Converter efficiency at 11 V input as a function of output power.

Figure 3.26 compares the converter efficiency as a function of output power when the converter operates with the nanolaminated CoNiFe core and the same geometry nanolaminated permalloy core under input voltage of 11 V, output voltage of 7 V, and switching frequency approximately 1.1 MHz. At the same output power levels, use of the nanolaminated CoNiFe core resulted in higher converter efficiency than use of the nanolaminated permalloy core as shown in the graph. Also, it is observed that the converter efficiency decreased as output power increased when the converter operated with a nanolaminated permalloy core, while the converter efficiency remained higher than 90 % over the entire range of output power levels when it was operated with a nanolaminated CoNiFe core. The decreasing efficiency of the converter employing the nanolaminated

permalloy core is caused possibly due to the saturation of the magnetic core. Considering the DC current of the inductor ($I_{dc} = V_{out}/R_{out}$) during the converter operation, together with the peak flux density of 0.4 T, it is estimated that the maximum peak flux density of the permalloy core at high output power levels (> 5 W) is approaching 1 T, which is close to the saturation flux density (1.2 T) of the material. In this saturation region, magnetic material can exhibit non-linear behavior (e.g., non-linear permeability) [9], possibly resulting in unstable operation of the converter (e.g., altering switching frequency). Consequently, there can be increasing losses from the magnetic core as well as other components in the converter. These results demonstrate the superior performance of the nanolaminated CoNiFe core over that of nanolaminated permalloy in this DC-DC power conversion application.

The properties of both nanolaminated permalloy and CoNiFe cores, fabricated by SU-8 support approach, ranging from intrinsic magnetic property to system level performance are compared in Table 3.6, showing the superior properties of the nanolaminated CoNiFe core. Note that the core volume was calculated by multiplying core surface, single lamination thickness, and number of layers due to the presence of many support holes in the core (Figure. 3.4 (b)).

Table 3.6 Comparison of nanolaminated permalloy and CoNiFe cores

| **Inductor and core configuration** | | |
|---|---|---|
| Number of windings | 36 | |
| Core outer diameter | 10 mm | |
| Core inner diameter | 6 mm | |
| Number of support holes | 200 | |
| Total support hole area | 11.7 $mm^2$ | |
| Core surface area | 38.56 $mm^2$ | |
| Single layer thickness | 500 nm | |
| Number of layers | 70 | |
| Total core thickness | 35 µm | |
| Core cross section area | 0.07 $mm^2$ | |
| Total core volume | 1.3496 $mm^3$ | |
| **Thin film property** | | |
| | Permalloy | CoNiFe |
| Saturation flux density | 1.25 T | 1.83 T |
| Coercivity force | 1.5 Oe | 0.5 Oe |
| **Nanolaminated core** | | |
| Core peak quality factor | 60 (@ 1 MHz) | 80 (@ 1 MHz) |
| Effective permeability | ~ 100 | ~ 200 |
| Operation peak flux density | Up to 0.5 T | Up to 0.9 T |
| $P_{V,hyst}$ (@1 MHz, 0.4 T) | 566 $W/cm^3$ | 392 $W/cm^3$ |
| $P_{V,eddy}$ (@1 MHz, 0.4 T) | 28.3 $W/cm^3$ | 8.35 $W/cm^3$ |
| **Converter test** | | |
| Input voltage | 10 - 11 V | 10 - 11 V |
| Output voltage | 7 V | 7 V |
| Output power | 3 - 6.5 W | 3 - 8 W |
| Switching frequency | 1.05 - 1.3 MHz | 1.05 - 1.1 MHz |
| Peak flux density of core | 0.4 T | 0.4 T |
| Converter efficiency | 84 ~ 89% | 90 ~ 91% |

## 3.6 Anisotropic Nanolaminated CoNiFe Core

Previous chapters presented toroidal-shape nanolaminated magnetic cores comprising tens to hundreds of layers of 300 – 1000 nm thick metallic alloys (i.e., $Ni_{80}Fe_{20}$ or $Co_{44}Ni_{37}Fe_{19}$) based on sequential electrodeposition, demonstrating suppressed eddy-current losses at MHz frequencies. It is also demonstrated that the nanolaminated CoNiFe core exhibits better properties (e.g., higher saturation flux density and lower hysteresis losses) than the nanolaminated permalloy core. In order to further improve the magnetic property of the nanolaminated CoNiFe core, magnetic anisotropy was induced to the cores by applying an external magnetic field (50 - 100 mT) during the electrodeposition of CoNiFe film.

The magnetic properties of soft magnetic metallic alloys can often be improved by induction of magnetic anisotropy (i.e., easy and hard axes). It is reported that the anisotropic magnetic cores exhibit higher permeability and lower magnetic losses in the MHz frequency range and above when magnetic flux flows in the direction parallel to the hard axis during operation [82, 83].

In the following section, fabrication and characterization of anisotropic nanolaminated CoNiFe cores featuring a hard magnetic axis in the length direction are presented.

### 3.6.1 Fabrication of Anisotropic Nanolaminated CoNiFe Cores

In order to apply magnetic anisotropy to the nanolaminated CoNiFe core, a rectangular shape has been introduced to apply the hard magnetic axis in the length direction. The rectangular, anisotropic nanolaminated CoNiFe cores were batch-fabricated based on automated sequential electroplating as depicted in Chapter 3.3. Magnetic

anisotropy was induced by applying an external magnetic field (50 – 100 mT) during CoNiFe electrodeposition by placing two permanent magnets across the substrate as shown in Figure 3.27. The orientation of the magnetic field was perpendicular to the long axis of the rectangular core so as to realize a hard magnetic axis in the length direction.

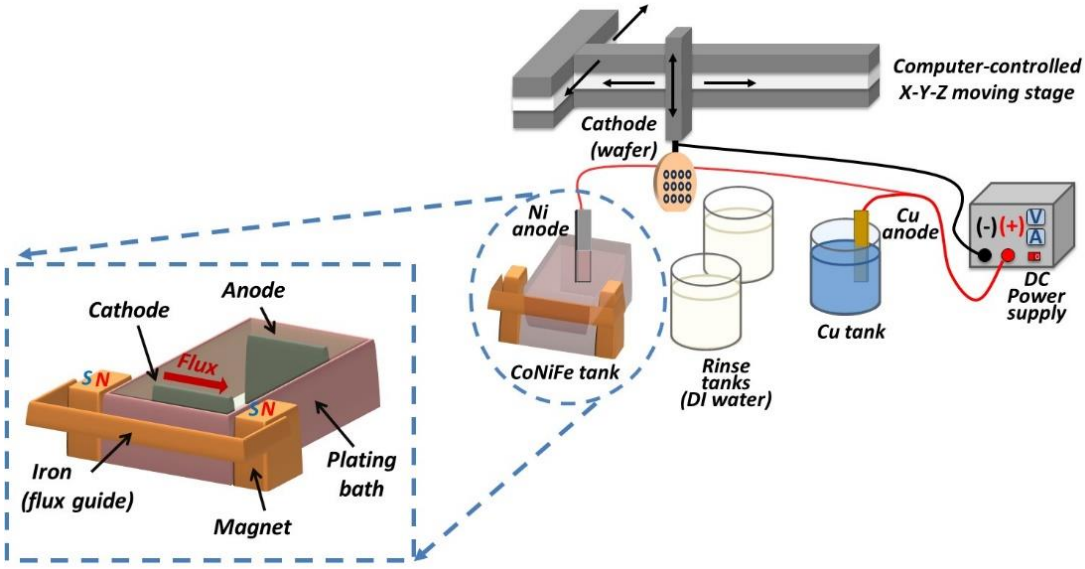


Figure 3.27 Schematic of in-field sequential electrodeposition system.

Figure 3.28 shows images of anisotropic nanolaminated CoNiFe cores and test inductors. The cores are 2 mm wide and 10 – 15 mm long rectangular cores comprising tens to hundreds layers of 500 – 1000-nm-thick CoNiFe laminations. For these rectangular cores, threading holes are required to connect a string when surface-tension-driven assembly is utilized as shown in Figure 3.28 (a) and (b). Figure 3.28 (c) and (d) shows cross-section SEM images of the core, demonstrating that individual 500-nm-thick CoNiFe laminations are separated from each other. Figure 3.28 (e) and (f) shows laser-machined polymeric bobbins and 10 – 22 turn test inductors with the cores.

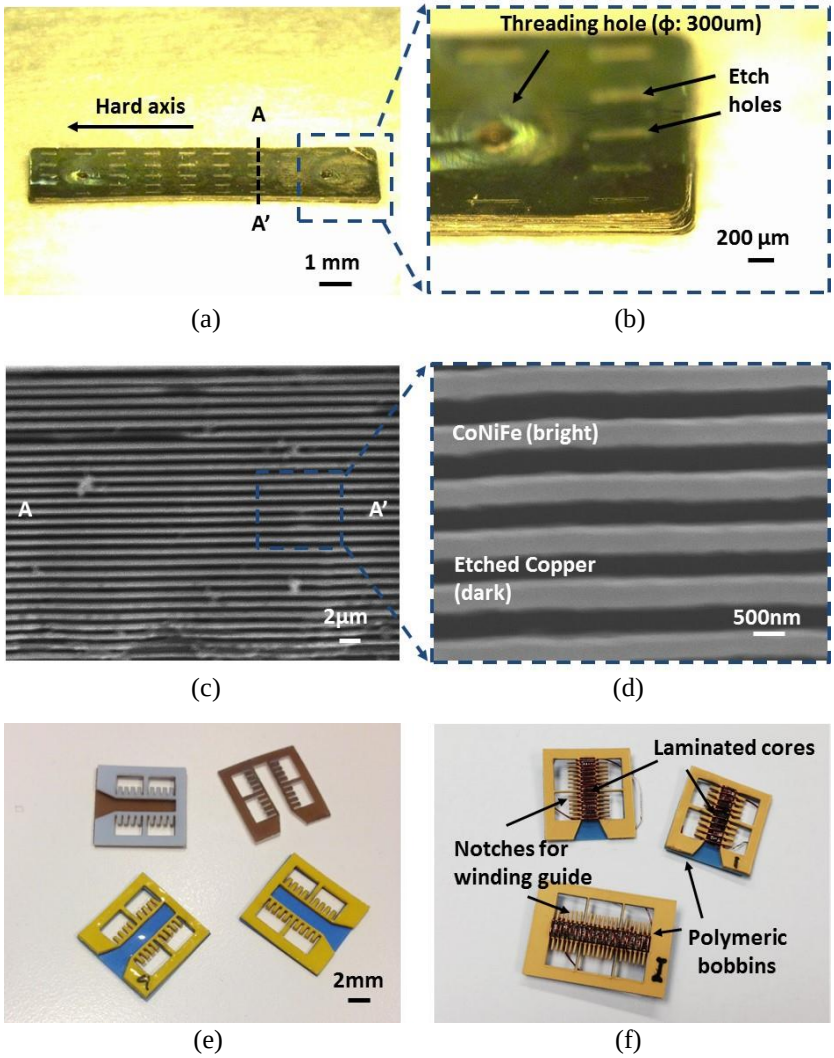


Figure 3.28 Images of anisotropic nanolaminated CoNiFe cores and test inductors.

### 3.6.2 Characterization of Anisotropic Nanolaminated CoNiFe cores

An anisotropic nanolaminated CoNiFe core comprising 70 layers of 500 nm-thick laminations was packaged in a solenoid test inductor by winding 22 turns of magnet wire (inset of Figure 3.26) around the core for characterization. Low flux and high flux measurement and system level characterization has been performed.

### 3.6.2.1 Low Flux Characterization

For low and high flux characterization, an isotropic nanolaminated CoNiFe core of the identical geometry electrodeposited without external magnetic field was also prepared for comparison. First, both inductors were characterized using an impedance analyzer (HP 4194A).

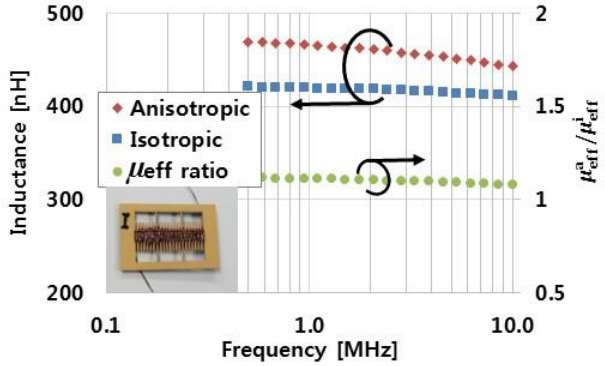


Figure 3.29 Measured inductance of test inductors and ratio of effective permeabilities of nanolaminated CoNiFe cores.

As shown in Figure 3.29, the test inductor with the anisotropic core shows approximately 10% higher inductance than the test inductor with the isotropic core over the 0.5 - 10 MHz frequency range. The constant inductance from both cores indicates that the eddy currents are suppressed in each nanolamination. Considering the identical geometry of both cores, the higher inductance is attributed to the higher effective permeability of the anisotropic core; i.e., the ratio of effective permeability of both cores (i.e., $\mu_{eff}$ of anisotropic core divided by $\mu_{eff}$ of isotropic core ($\mu^a_{eff}/\mu^i_{eff}$)) can be estimated from the ratio of measured inductances of the test inductors.

### 3.6.2.2 High Flux Characterization

Further investigation of volumetric power losses on both magnetic cores at high flux density (0.1 – 0.5 T) at 1 MHz was performed based on the high flux and high frequency characterization method explained in Chapter 3.3.2. Figure 3.30 shows volumetric power losses of both anisotropic and isotropic cores at 1 MHz, demonstrating that the anisotropic core exhibits approximately 25% reduced total volumetric power losses (i.e., sum of the hysteresis losses and the eddy-current losses) compared to the isotropic core at the same peak flux density levels. Since eddy-current losses of both cores are suppressed to a negligible level, the reduced volumetric power losses of the anisotropic core are mainly attributed to the reduced hysteresis losses resulting from the induced anisotropy.

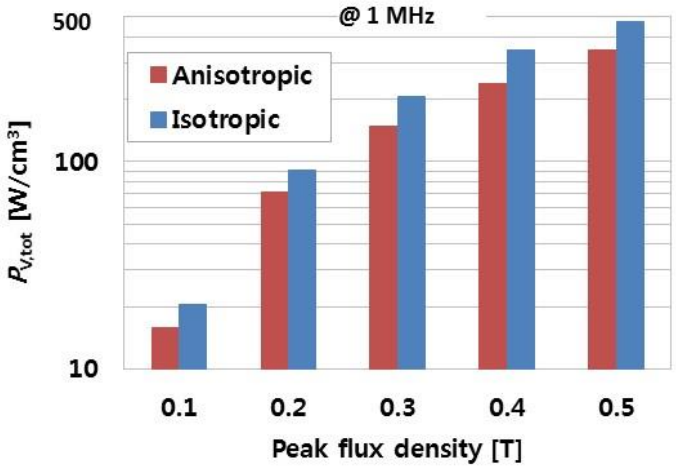


Figure. 3.30 Total volumetric power losses of nanolaminated CoNiFe cores at 1 MHz as a function of peak flux density. Note that y-axis is in log-scale.

### 3.6.2.3 High Power DC-DC Converter Test

The 22-turn test inductor with the anisotropic nanolaminated CoNiFe core was operated in a DC-DC converter evaluation board (LM 5116, TI) by replacing a commercial

inductor in the board with the test inductor. A diagram of the evaluation board and typical component values can be found in [84]. By modifying the resistor that sets the switching frequency, the converter operated at switching frequencies above 1 MHz and output power higher than 2 W. Figure 3.31 shows the evaluation board with the replaced resistor and the 22-turn test inductor.

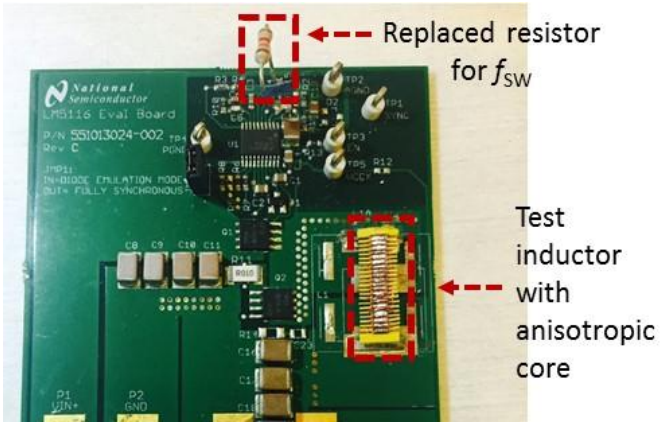


Figure 3.31 Converter evaluation board with replaced resistor and test inductor with anisotropic core.

During the measurement, applied input voltages were ranging from 8V to 15V, and output voltage was fixed at 5.3 V with a switching frequency 1.1 – 1.5 MHz. Converter efficiencies as a function of output power are shown in Figure 3.32. With an input voltage of 8 V, the converter efficiency exceeds 90 % up to 5 W output power. Decreasing converter efficiency was observed with increasing voltage regulation ratio, and the converter efficiency was approximately 81 % with a 15 V input voltage at 6.5 W output power.

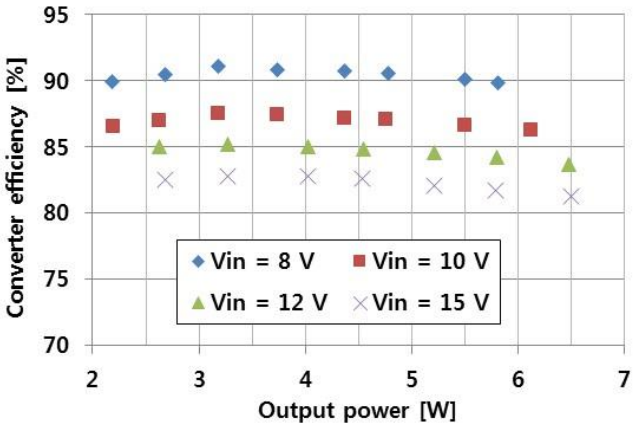


Figure 3.32 Experimental results of DC-DC converter performance tested with an anisotropic, nanolaminated CoNiFe core inductor. Converter efficiency as a function of output power at 5 V fixed output voltage.

### 3.7 Conclusion

In this chapter, fabrication and characterization of nanolaminated metallic alloy (i.e., permalloy and CoNiFe) cores were presented. The nanolaminated cores were fabricated based on sequential electrodeposition followed by sacrificial layer removal. Characterization of the nanolaminated metallic alloy cores demonstrated that substantial magnetic volume for high power was achieved from the stacked multiple magnetic and insulating layers, while eddy currents were suppressed in the magnetic nanolaminations. . It was also observed that the superior magnetic properties of CoNiFe (i.e., higher saturation flux density and lower coercivity) result in higher operational flux density and lower volumetric power losses of the nanolaminated CoNiFe core, compared to the nanolaminated permalloy core. The high saturation flux density of CoNiFe, together with large number of nano-range-magnetic layers enabled by CMOS-compatible processes will enable the development of high power density, ultracompact magnetic components for DC-DC power conversion application. To demonstrate this, in the following chapter, the

nanolaminated CoNiFe cores are integrated into microfabricated windings for on-chip inductors that can realize PSiP and PSoC.

# CHAPTER 4

# MICROFABRICATED INDUCTORS INTEGRATED WITH NANOLAMINATED MAGNETIC CORES

## 4.1 Introduction

This chapter presents microfabricated inductors integrated with nanolaminated metallic cores for high power and high frequency DC-DC power conversion. Since it is demonstrated that CoNiFe cores show better performance than permalloy cores in the previous chapter, only CoNiFe cores were considered for integration into microfabricated inductors.

As shown in chapter 2, the miniaturization of DC-DC converters is often made more challenging by their need for passive components, e.g., inductors, which can consume large physical volumes. Consequently, significant effort has been expended to develop chip-scale inductors using advanced microfabrication technology, exploiting the trends of increasing switching frequencies as well as incorporation of magnetic cores to reduce physical size. Especially, in order to realize microfabricated inductors that can handle high power (e.g., > 10 W), it is required to develop 1) magnetic materials with sufficiently large volume and minimized losses; 2) microfabricated windings providing a large magnetic flux path where the large volume core could be placed; and 3) a fabrication technique to integrate the large volume core into the windings. Since we demonstrated the nanolaminated magnetic cores with sufficiently large volume and minimized eddy-current losses, this chapter presents fabrication of the chip-scale inductor integrated with the nanolaminated CoNiFe cores.

In order to realize the integrated inductor with the nanolaminated CoNiFe core, two types of microfabrication techniques were studied for the microfabricated inductors with nanolaminated cores: 1) core drop-in approach where pre-fabricated cores are incorporated as an intermediate step in the fabrication of windings; and 2) direct winding approach where windings are directly fabricated on insulated core.

### 4.2 Microfabricated Inductors using Core Drop-in Approach

Fabrication process of the core drop-in approach for microfabricated inductors with nanolaminated CoNiFe cores can be divided into three main steps as illustrated in Figure 4.1. First, the nanolaminated CoNiFe cores and partially-formed windings (i.e., bottom and vertical windings) are individually prepared (Figure 4.1 (a)). Second, the cores are integrated with the partially-formed windings by means of a drop-in approach (Figure 4.1 (b)). Third, top windings are fabricated to complete the toroidal inductor (Figure 4.1 (c)).

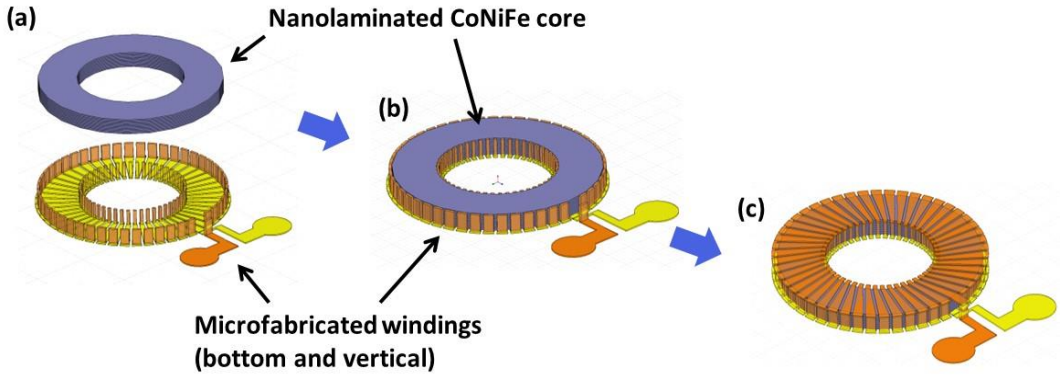


Figure 4.1 Conceptual approach for microfabricated inductor with drop-in core.

### 4.2.1 Fabrication Process of Core Drop-in Approach

#### 4.2.1.1 Winding Fabrication and Core Drop-in

A typical microfabricated toroidal inductor winding consists of bottom, vertical, and top conductors. For the proposed drop-in approach, the vertical conductors are fabricated based on copper metallization of high-aspect-ratio SU-8 pillars, followed by lithographic patterning [85]. Figure 4.2 (a) shows fabricated 50-turn bottom and vertical conductors on a glass substrate. For the bottom windings, approximately 250-μm-wide, 30-μm-thick conductors are positioned with 100 μm interconductor lateral spacing. For the vertical windings, 1-mm-tall SU-8 pillars with 100 μm diameter are lithographically formed and coated with a 30-μm-thick electrodeposited copper layer. These high aspect ratio vertical windings enable placement of large volume magnetic cores. Once the partially-fabricated windings (i.e., bottom and vertical winding) are prepared, nanolaminated CoNiFe cores are manually pick-and-placed and affixed as shown in Figure 4.2(b). In order to prevent electrical shorts between the windings and the core, either a 100-μm-thick insulating spacer (Plastic Shim Stock, ARTUS) is added between them or the nanolaminated CoNiFe core is pre-packaged with PDMS (Polydimethylsiloxane) (SYLGARD 184, Dow Corning) since it can fill the interspace between each magnetic film, providing mechanically robustness once it is cross-linked. In order to ensure the infiltration of PDMS into the nanolaminated structure, the core is immersed in un-crosslinked PDMS and vacuum is applied for approximately 10 minutes. The infiltrated PDMS is fully cross-linked in 48 hours at room temperature. As the PDMS is firmly confined between the CoNiFe layers due to the vacuum process, excess PDMS around the core is easily stripped manually, providing a PDMS-laminated CoNiFe multilayer core.

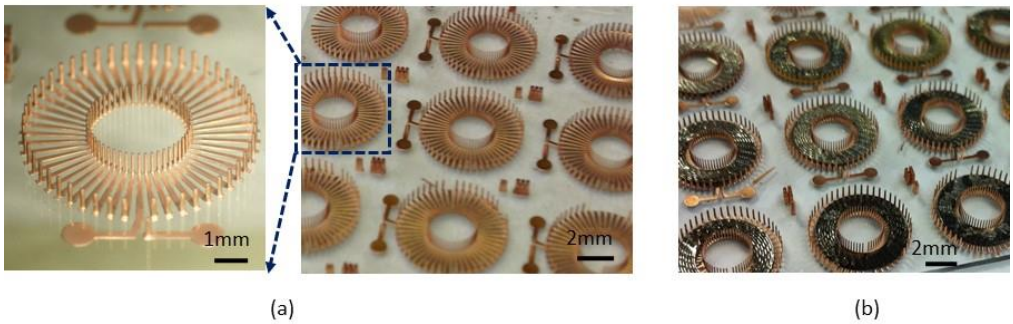


Figure 4.2 Drop-in cores. (a) Batch fabricated 50-turn partial windings on glass substrate. (b) Nanolaminated CoNiFe cores integrated with the partial windings.

#### 4.2.1.2 Core Integration

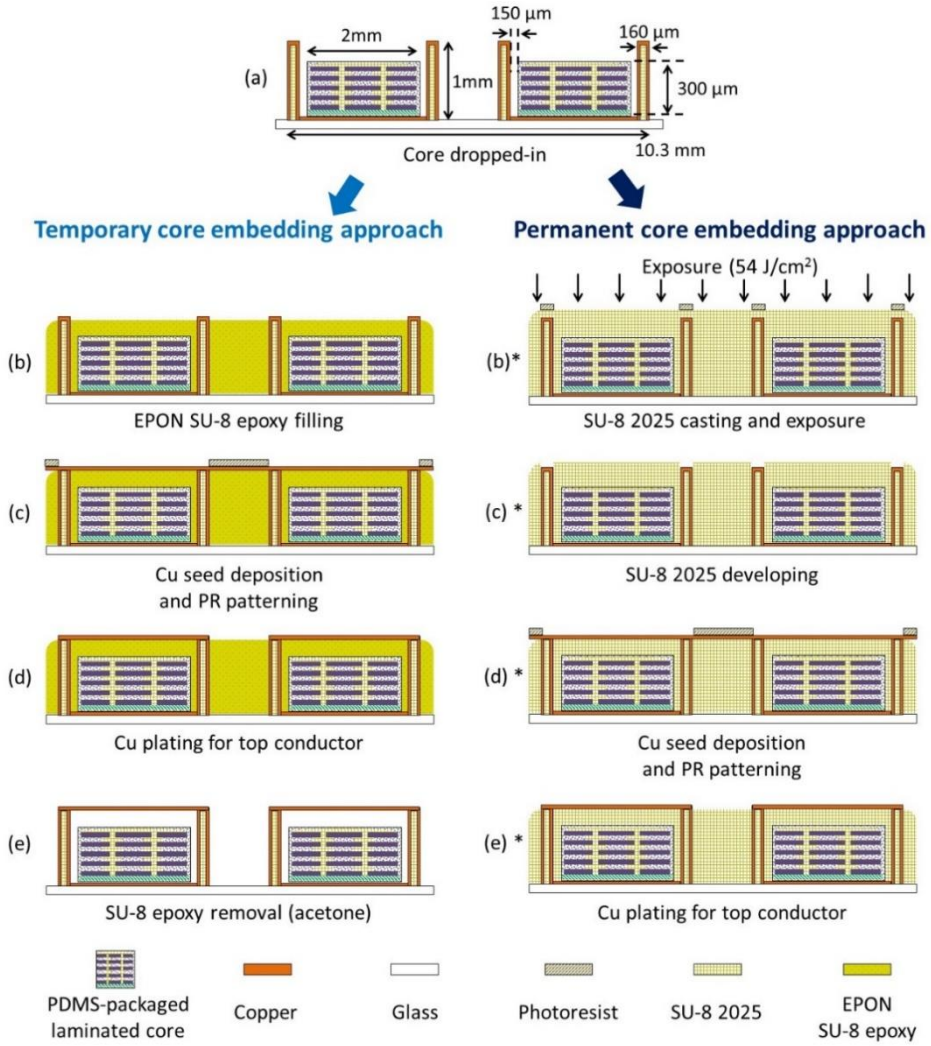


Figure 4.3 Core integration approaches after (a) core drop into the partially fabricated windings. (b) - (e) temporary core embedding approach, (b)* - (e)* permanent core embedding approach.

Prior to top winding fabrication, it is critical to form an insulating layer on top of the nanolaminated core where the top windings will be deposited and patterned. The insulating layer should possess a planar surface for top conductor deposition as well as sufficient thickness to avoid parasitic capacitance between the metallic core and top windings. Two methods, a *temporary* core embedding approach and a *permanent* core embedding approach, are explored as shown in Figure 4.3.

The temporary core embedding approach utilizes non-photopatternable EPON SU-8 epoxy pellets (Miller-Stephenson, Inc.), which will be removed in acetone after top winding fabrication. In this approach, epoxy pellets in a sufficient quantity to cover the nanolaminated core are distributed on the partially fabricated inductors (i.e., bottom and vertical windings, and magnetic cores) and melted at 130˚C on a hotplate as shown in Figure 4.3(b). In this step, it is critical to obtain an appropriate insulating layer thickness (600 μm - 900 μm from the bottom winding) so as to not cover the top of the vertical windings since the SU-8 epoxy pellet is not photo-patternable. However, due to the lack of solvent and crosslinker in the SU-8 epoxy pellet, long softbaking times are not required even for thick films, resulting in reduced process time. After melting, the SU-8 epoxy is brought to room temperature for approximately one hour until it is re-solidified. Figure 4.4(a) shows the inductor after the epoxy sacrificial layer step has been completed. Note that the top of the vertical windings are exposed while the laminated metallic core is embedded within the SU-8 sacrificial epoxy.

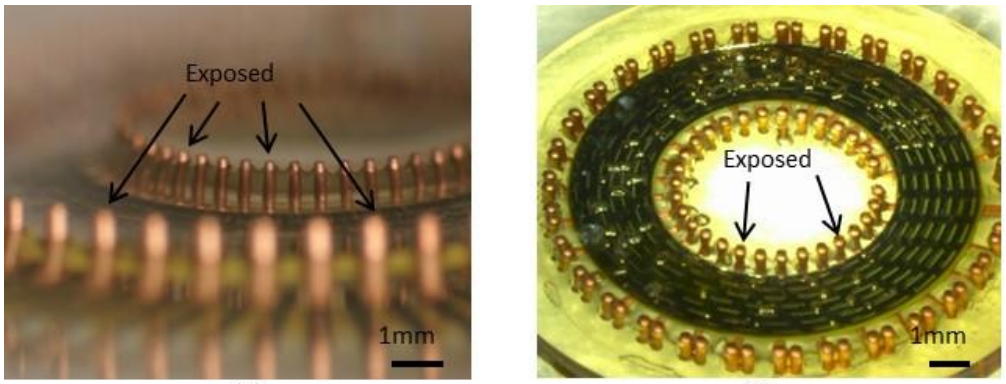


Figure 4.4 Optical images of fabricated additional layers with (a) EPON SU-8 epoxy using temporary core embedding approach, and (b) photopatternable SU-8 2025 using permanent core embedding approach.

In contrast, the permanent core embedding approach utilizes photo-definable SU-8 2025 (MicroChem). After casting SU-8 on the sample by weight as shown in Figure 4.3(b)*, it is planarized and softbaked at 95˚C for 12 hours on a hotplate. Note that 1g of casted SU-8 corresponds to 1 mm thickness on a 6.45 $cm^2$ glass substrate after softbaking. Since the softbaked SU-8 covers the vertical windings, it is patterned to expose the vertical windings to connect with top windings. After 4 hours cooling, the SU-8 is exposed with a UV light intensity of 54 $J/cm^2$ as shown in figure 5(b)*, followed by post bake at 95˚C for 30 minutes. The sample is then developed in PGMEA (propylene glycol methyl ether acetate)-based Thinner P (MicroChem) for 25 minutes leaving the vertical windings exposed as shown in Figure 4.3(c)*. Figure 4.4(b) shows that patterned SU-8 insulating layers encapsulate the lower and vertical windings as well as the core, and that the tops of the vertical conductors protrude. Since the SU-8 is fully crosslinked, it potentially provides higher mechanical robustness for the inductor.

Both temporary and permanent core embedding approaches are summarized in Table 4.1.

Table 4.1 Comparison of *temporary* and *permanent* core embedding approaches.

| | Temporary core embedding approach | Permanent core embedding approach |
|---|---|---|
| Insulating material | EPON SU-8 epoxy pellets (Miller-Stephenson, Inc.) | SU-8 2025 (MicroChem) |
| Process sequence | Melted at 130˚C<br>Solidified at 23˚C for 1 hr | Softbake at 95˚C for 12 hrs<br>Expose at 30mW/cm$^2$ for 30 min<br>Postbake at 95˚C for 30 min<br>Develop for 25 min in Thinner P |
| Top conductor seed layer deposition | E-beam evaporation | Sputtering or E-beam evaporation |
| Advantages | Fast process time | Mechanical reinforcement |
| Disadvantages | Non-photopatternable | More complex process steps |

#### 4.2.1.3 Top Winding Fabrication

For the two approaches, top windings are fabricated in a similar process. First, a 300-nm-thick copper seed layer is deposited by e-beam evaporation. Then, a 20-μm-thick photoresist layer is spray-coated on the seed layer and photolithographically patterned to serve as a mold for electrodeposition of top copper conductors as shown in Figure 4.3(c) and (d)*. After a 30-μm-thick copper electrodeposition, the photoresist and the copper seed layer are removed to complete the toroidal inductor fabrication as shown Figure 4.3(d) and (e)*. For the temporary core embedding approach, the embedding SU-8 epoxy can be removed in acetone as shown in Figure 4.3(e).

Optical images of integrated toroidal inductors with nanolaminated CoNiFe cores are shown in Figure 4.5. Figure 4.5(a) shows a 1-mm-tall, 50-turn-toroidal inductor fabricated using a dense winding mask. The sacrificial SU-8 epoxy has been removed upon completion of the top winding fabrication. The laminated magnetic core inside the toroid is comprised of 100 layers of CoNiFe with individual lamination thickness of 300 nm.

Figure 4.5(b) shows a 1-mm-tall, 30-turn-toroidal inductor fabricated using a sparse winding mask. The crosslinked SU-8 underlying the top windings enhances the mechanical robustness of the inductor. Although the integration approach is illustrated using nanolaminated CoNiFe cores, it is also potentially applicable to commercial ferrites and iron powder cores with suitable geometries.

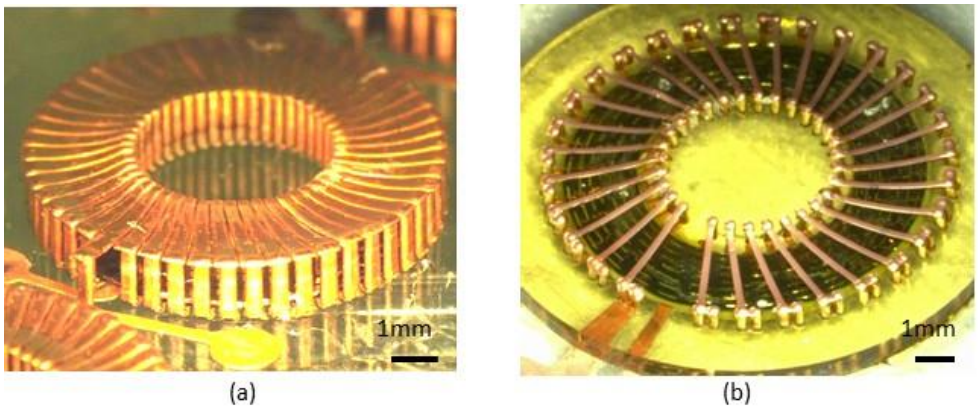


Figure 4.5 Microfabricated toroidal inductors integrated with nanolaminated CoNiFe cores. (a) 50-turn-dense winding and (b) 30-turn-sparse winding. Note in (b) the encapsulating SU-8 possesses a rim that extends to the periphery of the picture, resulting in additional mechanical stability.

### 4.2.2 Characterization of Toroid Microfabricated Inductors

The inductance, resistance, and quality factor of the inductors fabricated using core drop-in approaches were characterized as a function of frequency at typical core magnetic flux densities between 2 – 10 mT using an impedance analyzer (HP 4194 A). Figure 4.6 shows the measured result from a 50-turn toroid microfabricated inductor integrated with nanolaminated CoNiFe core using the temporary core embedding approach, and an air core inductor with the same nominal geometry. The nanolaminated core consists of 100 layers of 300 nm-thick CoNiFe laminations with 300-nm-tall interlamination gaps. Measured inductances of these two inductors are shown in Figure 4.6 (a). The microfabricated air

core inductor exhibits a constant inductance of approximately 210 nH (inductance density of 2.52e-3 μH/mm$^2$) up to 30 MHz. To validate this measured inductance, the theoretical inductance of the 50-turn-toroidal inductor has been estimated using the theoretical expression [86]:

$$L_{air} = \frac{\mu_0 \cdot A_{air} \cdot N^2}{\pi(r_i + r_o)} \tag{4.1}$$

where $\mu_0$ is the permeability of vacuum, $4\pi \times 10^{-7}$ H/m, $A_{air}$ is the cross-sectional area of the magnetic flux path [m$^2$], N is the number of windings, and $r_i$ and $r_0$ are the inner and outer radii of the toroid [m], respectively. With the parameters presented in Table 4.2, the theoretical air core inductance is estimated as 280 nH. The calculated and measured inductances agree within 25% up to 30 MHz. The lower measured inductance from the microfabricated inductor could be due to leakage flux between the windings and fabrication tolerances between the microfabricated inductor and the original design.

Table 4.2. Parameters of integrated inductor with nanolaminated cores

| | 50-turn-inductor | 30-turn-inductor |
|---|---|---|
| $A_{air}$ [m$^2$] | 2.3e-6 | 2.3e-6 |
| $A_{core}$ [m$^2$] | 6e-8 | 7e-8 |
| $r_i$ [m] | 2.85e-3 | 2.85e-3 |
| $r_o$ [m] | 5.15e-3 | 5.15e-3 |
| 2b [m] | 3e-7 | 5e-7 |
| $\mu_e$ | 250 | 330 |
| $N$ | 50 | 30 |

The measured inductance of the integrated inductor with laminated CoNiFe core exceeds 1.6 μH (inductance density of 1.9e-2 μH/mm$^2$) up to 30 MHz, showing approximately a 10 times inductance increase from the air core inductor. The measured inductance is also analyzed by comparing with theoretical prediction. To estimate the frequency-dependent inductance of the integrated inductor with nanolaminated CoNiFe

core, the effective permeability of the CoNiFe core is first extracted using a theoretical expression of low frequency inductance of integrated inductor with magnetic core, where eddy-current loss is negligible:

$$L_{core,DC} = \frac{\mu_0 \cdot \mu_e \cdot A_{core} \cdot N^2}{\pi(r_i + r_o)} \tag{4.2}$$

where $\mu_e$ is the effective permeability of magnetic core, and $A_{core}$ is the cross-sectional area of the magnetic core [$m^2$]. Considering that the total magnetic thickness of the nanolaminated core (30 μm) occupies approximately 3% of the total inductor thickness (1 mm), the effective permeability of the core is estimated as 250, which is in the range of typical soft magnetic material permeability (50 ~ 2000) [2]. Then, the frequency-dependent inductance ($L_{core}$) can be calculated based on a one-dimensional analysis of the electromagnetic diffusion in a laminated core with AC sinusoidal excitation [8, 10] which was introduced in chapter 3.3.3. Since the magnetic field intensity is depends only on the z-coordinate, equation (3.14) which was developed based on Poynting theorem can be expressed as:

$$\nabla^2 \vec{H} = \frac{d^2 \vec{H}}{dz^2} = j\omega\sigma\mu\vec{H} \tag{4.3}$$

The solution to differential equation (4.3) is in the form of:

$$\vec{H} = H_1 e^{Tz} + H_2 e^{-Tz} \tag{4.4}$$

Since the field is penetrating from both the top ($\vec{H}_{z=a/2}$) and the bottom ($\vec{H}_{z=-a/2}$) of the core lamination, the magnetic field intensity is expressed as:

$$H_y = H_1 e^{Tx} + H_2 e^{-Tx} = H_1 e^{-Tx} + H_2 e^{Tx} \tag{4.5}$$

where $H_0$ is the effective value of the magnetic field intensity in y-direction, and $T$ is $(1+j)/\delta$ as introduced in equation (3.26). By solving the equation:

$$H_1 = H_2 = \frac{H_y}{\cosh(T \cdot \frac{a}{2})} \tag{4.6}$$

Thus, the magnetic field intensity is:

$$\vec{H} = H_y \frac{\cosh(T \cdot z)}{\cosh(T \cdot \frac{a}{2})} \tag{4.7}$$

This leads to the magnetic flux density in the form of:

$$\vec{B} = \mu H_y \frac{\cosh(T \cdot z)}{\cosh(T \cdot \frac{a}{2})} \tag{4.8}$$

Then, the magnetic flux in the lamination is given by the integration of the magnetic flux density over the cross-section area:

$$\Phi = \int_{-a/2}^{a/2} d\vec{B} dz = \frac{2d\delta\mu}{1+j} H_y tanh\left\{\frac{(1+j)\frac{a}{2}}{\delta}\right\} \tag{4.9}$$

where $d$ is the width of the core. The total magnetic flux ($\Phi_c$) in the entire magnetic core (i.e., sum of all lamination layers) becomes:

$$\Phi_c = \frac{2dt\delta\mu}{(1+j)a} H_y tanh\left\{\frac{(1+j)\frac{a}{2}}{\delta}\right\} \tag{4.10}$$

where $t$ is the total magnetic thickness of the core [m]. The effective magnetic field intensity of the closed-loop core surface with $N$-turn winding is:

$$H_y = \frac{NI}{l} \tag{4.11}$$

where $I$ is the effective value of the current flowing through the windings [A] and $l$ is the magnetic path length of the core [m]. Considering a harmonic variation with time, the voltage induced in the winding is:

$$V = j\omega N \Phi_c \tag{4.12}$$

Thus, the impedance of winding due to the core is:

$$Z = \frac{V}{I} = \frac{j\omega dt\delta\mu}{(1+j)l\frac{a}{2}} N^2 tanh\left\{\frac{(1+j)\frac{a}{2}}{\delta}\right\} = L_{core,DC} \frac{j\omega\delta}{(1+j)\frac{a}{2}} tanh\left\{\frac{(1+j)\frac{a}{2}}{\delta}\right\} \tag{4.13}$$

By resolving this equation into its real and imaginary parts, the frequency-dependent core inductance ($L_{\text{core}}$) becomes:

$$L_{core} = L_{core,DC}\left(\frac{\delta}{a}\right)\left(\frac{\sinh\left(\frac{a}{\delta}\right)+\sin\left(\frac{a}{\delta}\right)}{\cosh\left(\frac{a}{\delta}\right)+\cos\left(\frac{a}{\delta}\right)}\right) \tag{4.14}$$

where $2b$ is the thickness of a single lamination layer [m], and $\delta$ is the skin depth [m] of the magnetic material at the operation frequency. Finally, the overall inductance ($L_{\text{total}}$) is expressed by adding inductances from air and magnetic core:

$$L_{total} = L_{air} + L_{core} = \frac{\mu_0 \cdot N^2}{\pi(r_i+r_o)}\left(A_{air} + A_{core}\mu_e\left(\frac{\delta}{a}\right)\left(\frac{\sinh\left(\frac{a}{\delta}\right)+\sin\left(\frac{a}{\delta}\right)}{\cosh\left(\frac{a}{\delta}\right)+\cos\left(\frac{a}{\delta}\right)}\right)\right) \tag{4.15}$$

From equation (4.15), the single lamination thickness (300 nm) of the core is well below the skin depth at 30 MHz (~1 μm), thereby the theoretical total inductance of the integrated inductor with nanolaminated CoNiFe core exhibits constant inductance of 2.1 μH up to 30 MHz. Compared with the theoretical inductance, the measured inductance shows a slight inductance decrease as frequency increases. Since the theoretical equation assumes perfect insulation of identical CoNiFe laminations, the decreasing inductance of fabricated inductor is possibly due to: 1) lamination thickness and material composition uniformity; 2) potentially collapsed CoNiFe layers causing electrical short; 3) parasitic capacitance between lamination layers as well as between the dense 50-turn-windings and the core. It is also shown that the measured inductance tends to increase after 20 MHz, implying a self resonance of the integrated inductor with nanolaminated CoNiFe core. The quality factors of the integrated inductor with nanolaminated core is approximately 12 at 6 MHz and higher than that of the air core inductor up to 15 MHz as shown in Figure 4.6 (b), indicating an effective energy storage/transfer capacity by utilizing nanolaminated magnetic cores.

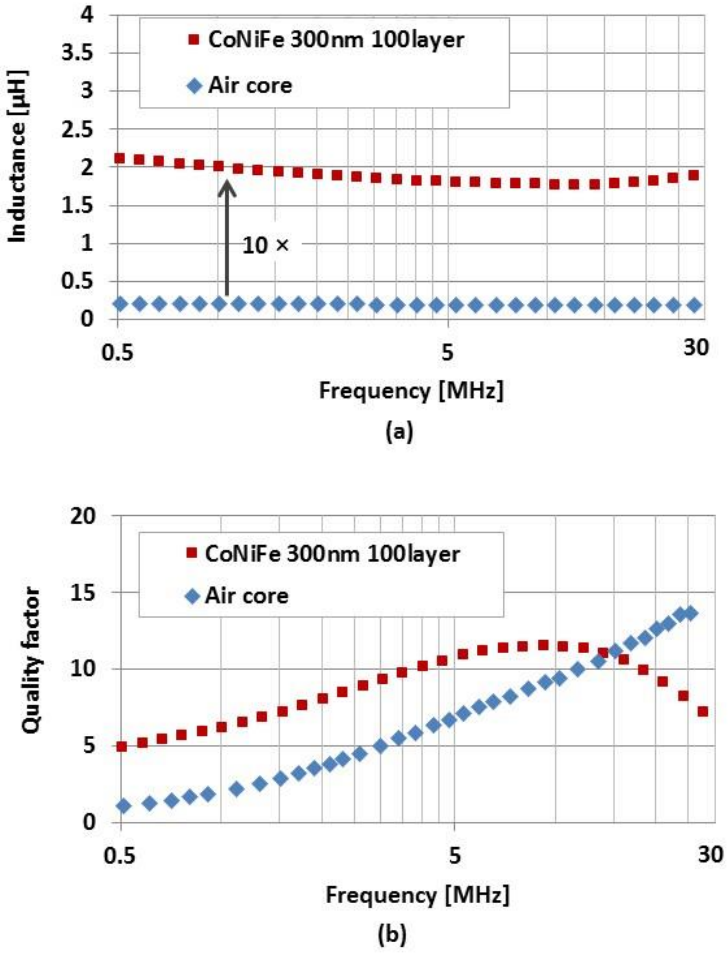


Figure 4.6 Characterization of 50-turn-integrated inductors with nanolaminated magnetic cores as well as an air core inductor by means of temporary core embedding approach. (a) Inductance, and (b) quality factor.

Figure 4.7 shows the measurement result from a 30-turn microfabricated inductor integrated with a nanolaminated CoNiFe core consisting of 70 layers of 500-nm-thick CoNiFe laminations (and 500-nm-tall interlamination gap) using the permanent core embedding approach, as well as an air core inductor with the same nominal geometry. Measured inductances of these two types inductors are shown in Figure 4.7 (a). The microfabricated air core inductor exhibits a constant inductance of approximately 96 nH

(inductance density of 1.15e-3 μH/mm$^2$) up to 30 MHz. The theoretical inductance of the 30-turn-toroidal inductor using equation (4.1) is estimated as 104 nH, demonstrating reasonable agreement with measured inductance up to 30 MHz. The 30-turn-inductor integrated with laminated CoNiFe core exhibits constant inductance of 1.15 μH (inductance density of 1.4e-2 μH/mm$^2$) up to 30 MHz, showing approximately a 12 times inductance increase over the air core inductor. From equation (4.2), the effective permeability of the nanolaminated CoNiFe core is estimated as 330. The measured inductance is also compared with theoretical prediction using equation (4.4). Since the single lamination thickness (500 nm) of the core is still below the skin depth at 30 MHz (~1 μm), the theoretical total inductance of the integrated inductor with nanolaminated CoNiFe core predicts a constant inductance of 1.15 μH up to 30 MHz. The good agreement of measured inductance with theoretical prediction indicates that improved insulation from thicker interlamination gap as well as uniform lamination thickness, resulting in suppressed eddy-current flow in the nanolaminated core. It is also expected that the sparsely-distributed 30-turn-windings compared to the densely-distributed 50-turn-windings minimize the capacitive effect between the core and the windings. In Figure 4.7 (b), the quality factor of the integrated inductor with nanolaminated CoNiFe core is approaching 20 at 5 MHz, and is greater than that of the air core inductor up to 15 MHz. Compared to the peak quality factor frequency (~ 6 MHz) from the 100 layers of 300-nm-thick CoNiFe laminations shown in Figure 4.6 (b), the higher quality factor implies that optimization of winding geometry (e.g., winging width, thickness, and height) as well as core design (e.g., lamination thickness, gap between the laminations) can improve the quality factors of the integrated inductors with nanolaminated magnetic core.

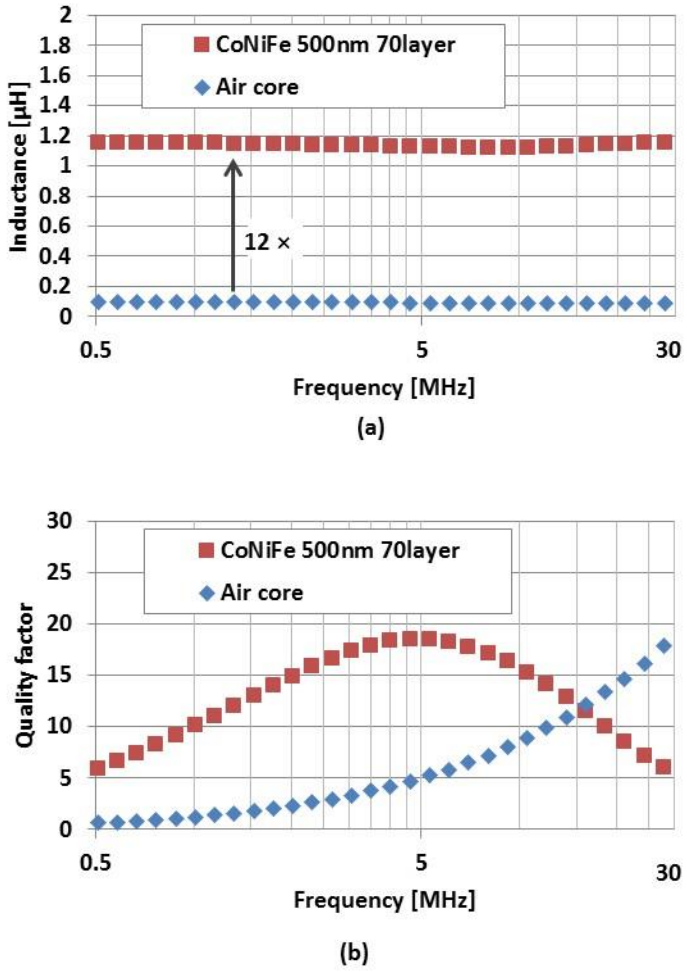


Figure 4.7 Characterization of 30-turn-integrated inductors with nanolaminated magnetic cores, as well as an air core by means of permanent core embedding approach. (a) Inductance, and (b) quality factor.

### 4.2.3 Solenoid Microfabricated Inductors using Core Drop-in Approach

Solenoid microfabricated inductor integrated with anisotropic nanolaminated CoNiFe core was also developed using core drop-in approach as shown in Figure 4.8 (a). Figure 4.8 (b) illustrates the cross section of the solenoid microinductor, showing specific dimensions of the device. A fully-fabricated 10-turn solenoid microinductor with an anisotropic nanolaminated CoNiFe core is shown in Figure 4.8 (c) and (d).

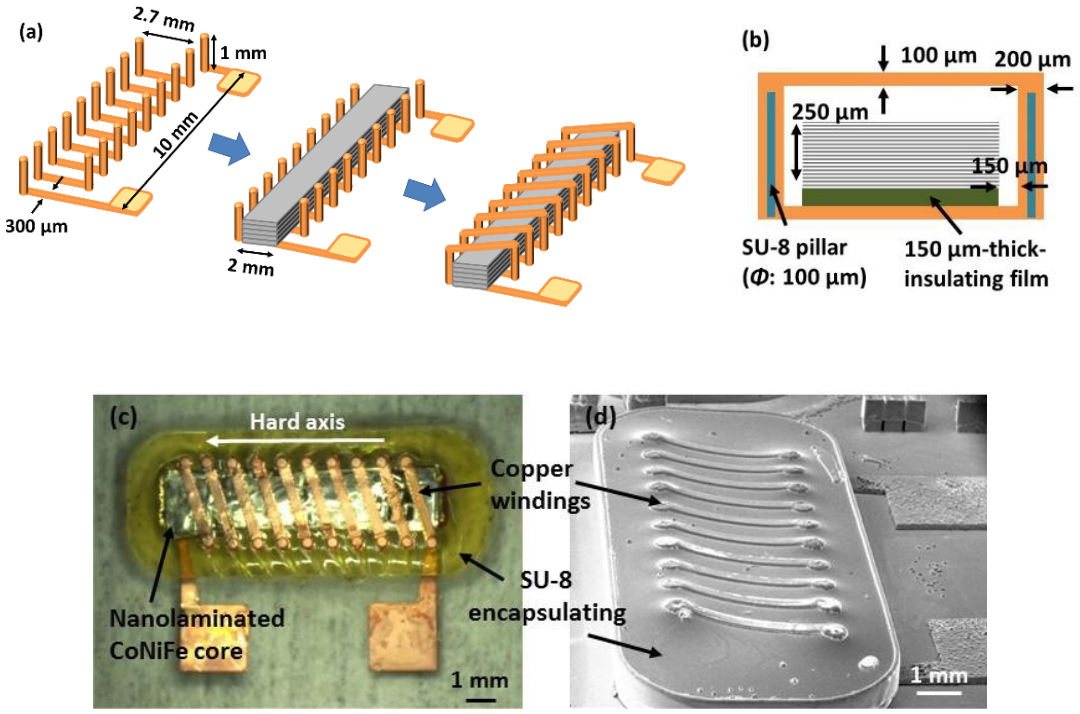


Figure 4.8 10-turn microfabricated solenoid inductor with an anisotropic nanolaminated CoNiFe core. (a) Fabrication steps, (b) cross section, (c) optical and (d) SEM images.

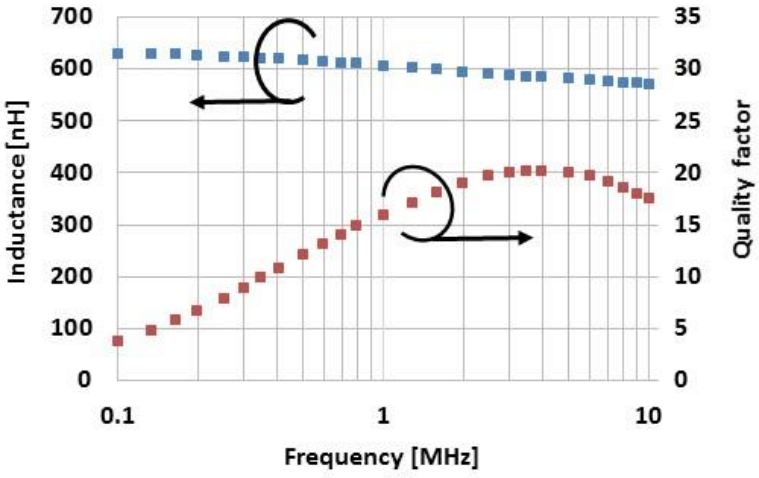


Figure 4.9 Characterization of a microfabricated solenoid inductor with nanolaminated CoNiFe core. Inductance and quality factor.

The microfabricated solenoid inductor with an anisotropic nanolaminated CoNiFe core was characterized in the 0.1 - 10 MHz frequency range using an impedance analyzer. The core comprises 200 layers of 1000-nm-thick CoNiFe laminations. As shown in Figure 4.9, the microinductor with the anisotropic core shows a constant inductance of 600 nH up to 10 MHz, indicating suppressed eddy-current losses in the measured frequency range. Peak quality factor of the microinductor exceeds 20 at 4 MHz.

## 4.3 Microfabricated Inductors using Direct Electroplated Winding Approach

The other type of microfabricated inductor winding method is a direct winding approach based on electrodeposition. This approach develops a microfabricated winding without using a conventional substrate, forming a microfabricated solenoid inductor directly upon a nanolaminated CoNiFe core. Typically, a substrate such as a glass or silicon is frequently used as a convenient flat surface platform for photopatterning and metallization. However, the substrate is often of no use after the fabrication process is completed and unnecessarily increases the overall device volume. The direct winding approach involves direct photopatterning on an epoxy-coated nanolaminated CoNiFe core. This approach is advantageous in particular with millimeter thick magnetic cores since it eliminates the proximity lithography step, which has been a relatively challenging process especially for the patterning of the high aspect ratio microstructures of previous substrate-supported inductors.

### 4.3.1 Fabrication Processes of Direct Electroplated Winding Approach

The fabrication sequence of the direct electroplated winding approach is described in Figure 4.10. A millimeter-thick nanolaminated CoNiFe core (Figure 4.10(a)) is dip-coated by SU-8 epoxy (Figure 4.10(b)). The dip-coating process comprises dipping in SU-

8 2025, drying in an oven (4 hours at 95℃), flood-UV-exposure for crosslinking (5 mJ/cm$^2$ for each side), and post-drying in an oven (1 hour at 95℃). A copper seed layer is deposited on the SU-8 surface of the sample by DC sputterering (Figure 4.10(c)), followed by photoresist-spray coating (20 µm of NR-7 resist, Figure 4.10(d)). Multiple photopatternings for inductor windings follow (Figure 4.10(e)), and copper electroplating is performed to form thick copper windings (Figure 4.10(f)). After removing the photoresist mold and the metal seed layers, the solenoid inductor is completed (Figure 4.10(g)).

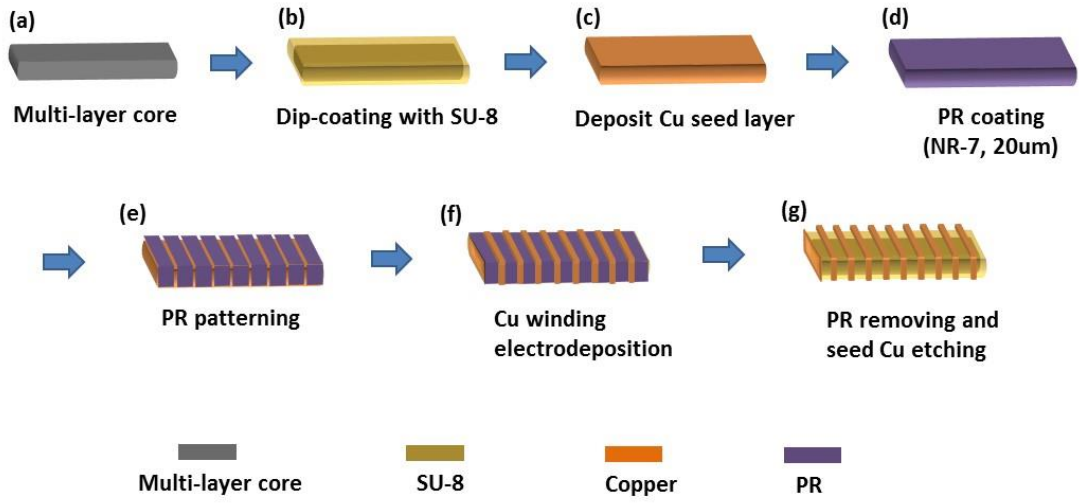


Figure 4.10 Fabrication sequence of microfabricated solenoid inductor with laminated CoNiFe core

Figure 4.11 shows optical images of the fabricated solenoid inductor with laminated CoNiFe core using the direct electroplated winding approach. Note that the laminated CoNiFe core is passivated with SU-8, preventing an electrical short between the core and the windings. The microfabricated windings have a winding width of approximately 800 µm, an interwinding distance of approximately 300 µm, and a winding thickness of approximately 300 µm.

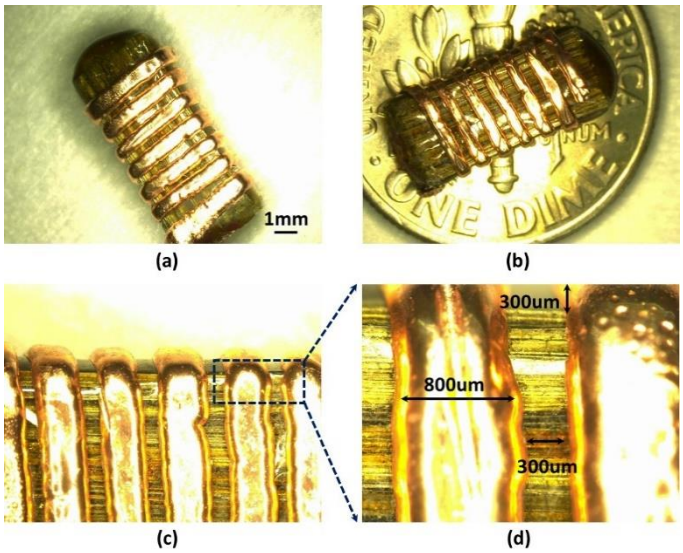


Figure 4.11 Optical images of a solenoid inductor with direct electroplated windings and laminated CoNiFe core.

### 4.3.2 Characterization of Solenoid Microfabricated Inductors

The microfabricated 9-turn solenoid inductor with nanolaminated CoNiFe core and direct electroplated windings is shown in the inset of Figure 4.12. The core is 1 cm long, 2 mm wide, and approximately 2 mm thick, and comprises 2000 layers of 1 µm thick CoNiFe laminations. Using an impedance analyzer (HP4194), an inductance of approximately 0.7 µH was measured over the frequency range 0.1 - 10 MHz as shown in the graph. A peak quality factor of approximately 35 was observed at 5.5 MHz.

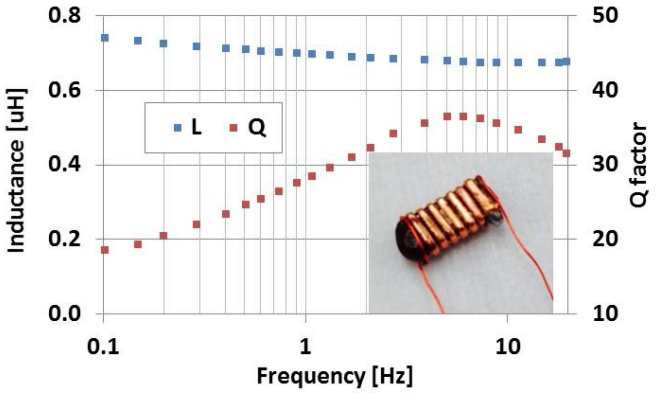


Figure 4.12 Measured inductance and quality factor of a 9-turm solenoid inductor with direct electroplated windings and a CoNiFe core comprising 2000 layers of 1-µm-laminations

### 4.4 Comparison of State-of-Art Microfabricated Inductors

Microfabricated inductors with nanolaminated CoNiFe cores fabricated using both the core drop-in approach as well as the direct electroplated winding approach are summarized in Table 4.3.

Table 4.3 Summary of microfabricated inductors with nanolaminated CoNiFe cores

| **Inductor configuration** | | | | |
|---|---|---|---|---|
| | 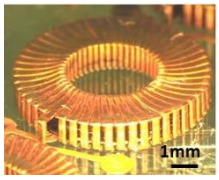  | 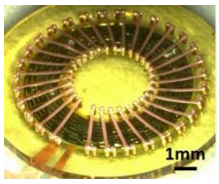  | 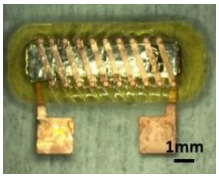  | 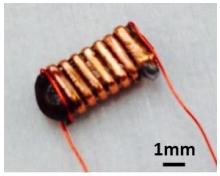  |
| Fabrication Method | Core drop-in (Temporary embedding) | Core drop-in (Permanent embedding) | Core drop-in (Permanent embedding) | Direct electroplated winding |
| Number of turns | 50 | 30 | 10 | 9 |
| Inductor surface area | 83.3 $mm^2$ | 83.3 $mm^2$ | 27 $mm^2$ | 31 $mm^2$ |
| Total inductor volume | 83.3 $mm^3$ | 83.3 $mm^3$ | 27 $mm^3$ | 80.6 $mm^3$ |
| **Core configuration** | | | | |
| Number of laminations | 100 | 300 | 200 | 2000 |
| Lamination thickness | 300 | 100 | 1000 | 1000 |
| Total magnetic thickness | 30 µm | 30 µm | 200 µm | 2000 µm |
| Core cross section area | 0.06 $mm^2$ | 0.06 $mm^2$ | 0.4 $mm^2$ | 4 $mm^2$ |
| Total core volume | 1.51 $mm^3$ | 1.51 $mm^3$ | 4 $mm^3$ | 40 $mm^3$ |
| **Inductor performance** | | | | |
| Inductance (0.5 - 10 MHz) | 2000 nH | 1200 nH | 600 nH | 700 nH |
| Peak Q factor | 12 at 6 MHz | 19 at 5 MHz | 20 at 4 MHz | 36 at 5 MHz |

Performance of the microinductor with the anisotropic nanolaminated CoNiFe core is also compared with other microinductors with electrodeposited magnetic cores [30, 39, 52, 54, 84 – 92]. Note that only electrodeposited magnetic cores are compared; performances of magnetic cores deposited by different techniques (e.g., sputtering or evaporation) are compared in [19]. These microinductors feature solenoid, spiral, or race track geometries and the magnetic cores comprise typically alloys of nickel, iron, and cobalt. Several figures of merit have been proposed to compare such microinductors based on inductance density, quality factor, saturation current density, and energy density ($E_D = Li_{sat}^2/2A$) [2]. Figure 4.13 compares the microinductors based on energy density and peak quality factor at 0.3 - 10 MHz. Generally, increasing magnetic core thickness for high energy density causes significant magnetic losses (e.g., eddy-current losses) at high frequency operation, resulting in low quality factor. Therefore, the thickness of the metallic alloy cores is typically limited to a few microns for MHz frequency range and above. The use of nanolaminated cores allows large overall magnetic thickness with suppressed eddy-current losses, simultaneously enabling high energy density and quality factor at high frequency as shown in the graph.

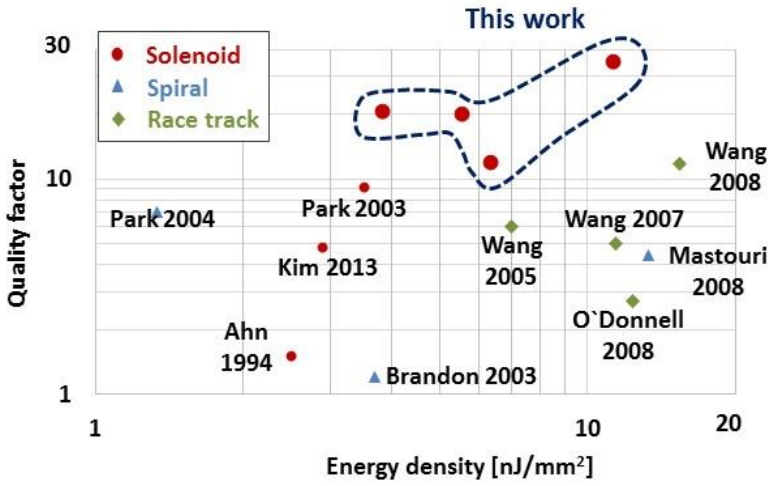


Figure 4.13 Comparison of microinductors with electroplated magnetic cores.

## 4.5 Performance of Microfabricated Inductors in High Power DC-DC Converter

### 4.5.1 Power Converter Topology

Microfabricated inductors were tested in a high-frequency and high-power DC-DC converter which is developed by our collaborators in an ARPA-E power conversion program [93]. The power converter has a merged-two-stage circuit topology operating in the high-frequency switching regime (3 – 30 MHz) and is designed for LED drivers operating from a wide-range DC input voltage. The two-stage topology is based on a soft-charged switched-capacitor pre-regulator/transformation stage and a high-frequency magnetic regulator stage as shown in Figure 4.14.

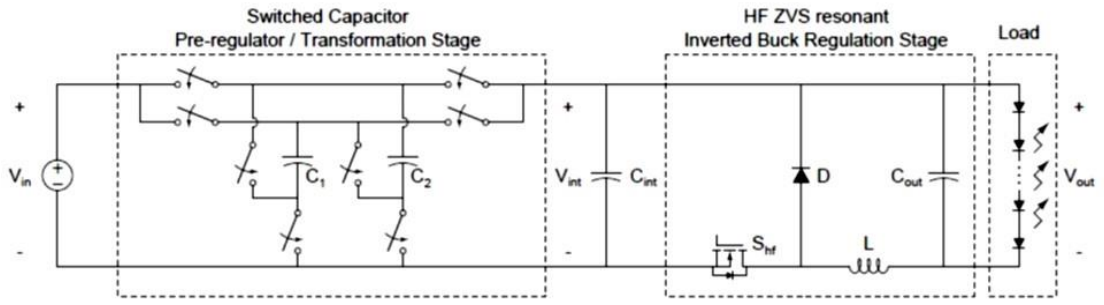


Figure 4. 14 A merged two-stage conversion architecture having a switched capacitor first stage that provides voltage pre-regulation and transformation, and a high-frequency magnetic stage that provides fine regulation of the output.

The first stage, that is, a variable-topology switched-capacitor (SC) circuit, operates at moderate switching frequencies (tens to hundreds of kHz). The details of the circuit with the controller design is shown in Figure 4.15. It consists of energy transfer capacitors (C1-C2) and power transistors (M1-M8), which are controlled to turn on and off by a micro-controller at a fixed frequency with 50% duty ratio. The SC circuit is designed

to achieve high power density and efficiency; however, the SC converter alone cannot efficiently provide the fine voltage regulation. This stage serves to reduce the voltage range over which the second stage (i.e., high-frequency magnetic regulation) needs to operate (50 – 100 V).

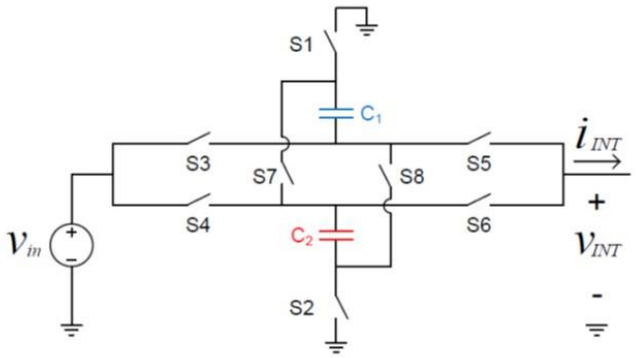


Figure 4.15 Schematic of the switched-capacitor pre-regulator/transformation stage with bootstrap diodes.

The second stage is a magnetic-based stage that provides both additional voltage transformation and fine voltage regulation. As shown in Figure 4.16, it is a resonant transition discontinuous-mode inverted buck converter operating at high frequency (3 - 30 MHz). The topology of the second stage is selected such that it requires relatively small inductor values and inherently absorbs parasitic capacitance as part of circuit operation. A benefit of this topology is that it operates with high inductor current ripple, yielding a relatively small required inductance value. Also, the softswitched nature of the circuit topology enables relatively high switching frequency to be achieved with acceptable loss, further reducing the required inductance value.

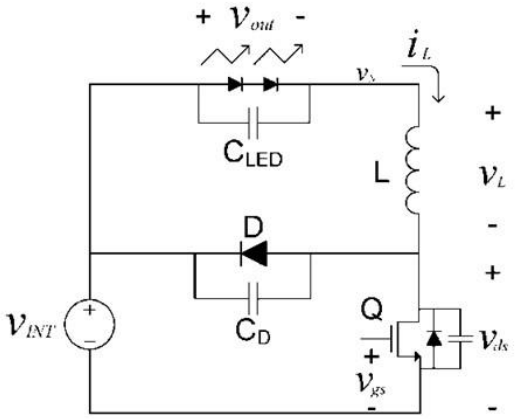


Figure 4.16 Schematic of the second magnetic-based regulation stage designed to operate at high frequency.

In summary, soft charging of the switched capacitor circuit, zero voltage switching of the high-frequency regulator circuit, and time-based indirect current control are used to maintain high efficiency, high frequency and power density, and high power factor for LED driver applications.

### 4.5.2 Microfabricated Inductors Tested in Power Converter

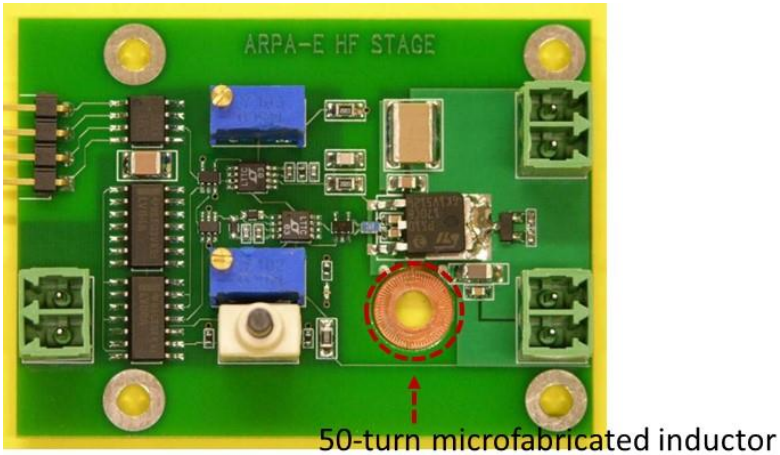


Figure 4.17 Image of converter circuit board integrated with a microfabricated inductor

Developed microfabricated inductors were integrated into the second magnetic-based regulation stage (high-frequency stage) in the power converter as shown in Figure

4.17. The power converter was operated with input voltage ranging from 50 V to 100 V and a switching frequency range of 1 - 10 MHz. Note that the output voltage was fixed at 35 V for all the input voltages.

#### 4.5.2.1 Toroid Microfabricated Inductor

First, the 50-turn toroidal microfabricated inductor with nanolaminated CoNiFe core detailed in the first column of Table 4.3 was tested in the power converter. The core comprises 300 layers of 100-nm-thick CoNiFe laminations, having outer diameter of 10 mm and inner diameter of 8 mm. The inductance of the inductor was approximately 1.2 μH over the range 0.1 – 10 MHz frequency. The test result for power converter efficiency and corresponding switching frequency as a function of input voltage is shown in Figure 4.18. The output power was ranging between 25 – 30 W during the measurement. Over the input voltage range of 55 – 100V, converter efficiencies of 87% at 50 V and 76% at 100 V operation were observed.

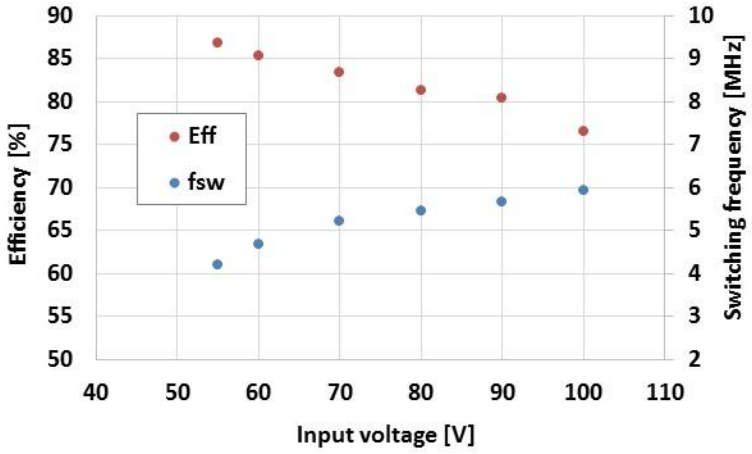


Figure 4.18 Experimental measurements of 50-turn toroidal inductor tested in power converter; converter efficiency and corresponding switching frequency as a function of input voltage.

#### 4.5.2.2 Solenoid Microfabricated Inductor

Second, the 10-turn solenoid microfabricated inductor with nanolaminated CoNiFe core detailed in the third column of Table 4.3 was tested in the power converter. The test result for power converter efficiency with various input voltages as a function of output power is shown in Figure 4.19. The switching frequency was ranging between 5 – 10 MHz during the measurement. Over the input voltage range of 50-100V, converter efficiencies of 93% at 50 V and 84% at 100 V operation were observed at an output power of 40 W.

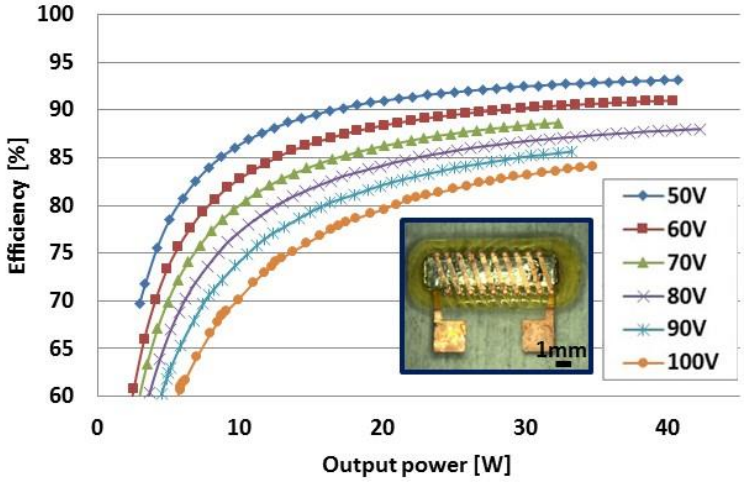


Figure 4.19 Experimental measurements of 10-turn solenoid inductor tested in power converter; converter efficiency with various input voltages as a function of output power.

#### 4.5.2.3 Solenoid Microfabricated Inductor with Large Core Volume

Lastly, the 9-turn solenoid microfabricated inductor with nanolaminated CoNiFe core detailed in the fourth column of Table 4.3 was tested in the power converter. The test result for power converter efficiency with various input voltages as a function of output power is shown in Figure 4.20. The switching frequency was ranging between 3 – 8 MHz during the measurement. At an input voltage of 50 V (blue line), the highest efficiency

exceeded 96.5% at an output power of 42 W. It was observed that the converter efficiency tends to decrease as the input voltage increases; however, the efficiency was exceeding 92% for all the input voltages. At the highest input voltage of 100 V (orange line), a maximum efficiency of 92.95% was observed at an output power of 41.5 W.

This result demonstrated that large magnetic core volume is required for regulation of high input voltage at these operating frequencies and powers. In addition, it was observed that solenoid inductors show higher converter efficiency than toroid inductors with similar thickness cores.

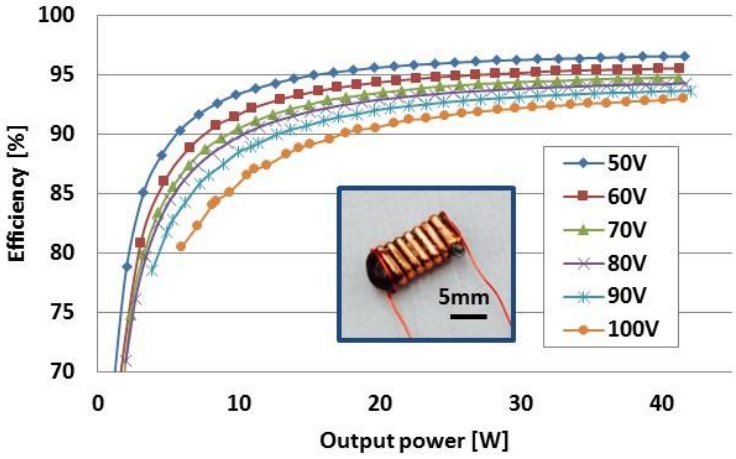


Figure 4.20 Experimental measurements of 9-turn solenoid inductor tested in power converter; converter efficiency with various input voltages as a function of output power.

## 4.6 Conclusion

In this chapter, the nanolaminated CoNiFe cores were integrated into microfabricated inductors for on-chip power supply application using two different microfabrication techniques: 1) core drop-in approach where pre-fabricated cores are incorporated as an intermediate step in the fabrication of inductor windings; and 2) direct winding approach where inductor windings are directly fabricated on encapsulated

magnetic core. By enabling integration of a large volume core (for high power handling) into the inductor windings, toroidal and bar-type microfabricated inductors with the nanolaminated CoNiFe cores were developed, demonstrating a high inductance of 2 μH up to 10 MHz and peak quality factor of 36 at 5 MHz. Combined with high power DC-DC buck converter designed by our collaborators at MIT, the converter operated at larger than 35 W output power and higher than 3 MHz switching frequency with a converter efficiency over 92 %, when the input voltage varied from 50 to 100 V and the output voltage was fixed at 35 V. The microfabricated inductor integrated with the nanolaminated CoNiFe core has the potential to enable ultracompact DC-DC power conversion operated at high power and high frequency.

# CHAPTER 5

# ULTRACOMPACT DC-DC BUCK CONVERTER WITH NANOLAMINATED MAGNETIC CORES

## 5.1 Introduction

In this chapter, a high-frequency (> 1 MHz) and high-power (> 10 W) ultracompact DC-DC converter using nanolaminated CoNiFe core inductors is presented, with the goal of understanding the converter area reductions achievable using this magnetic core technology. The ultracompact converter was developed utilizing commercially available components (regulator chip, capacitors, and resistors) with a nanolaminated CoNiFe core inductor on PCB (printed circuit board). For the nanolaminated CoNiFe core inductor, both toroid-type and bar-type cores were utilized.

## 5.2 Design of Ultracompact DC-DC Converter

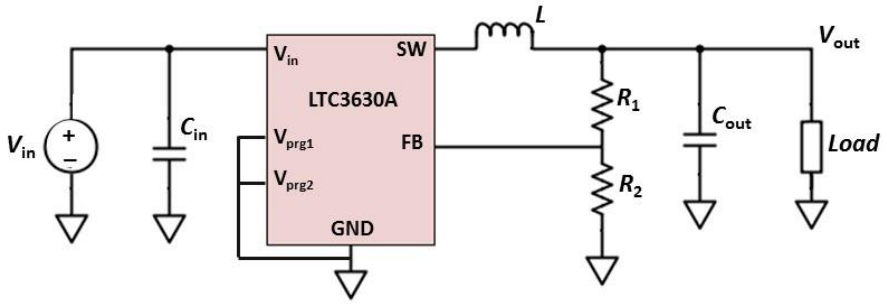


Figure 5.1 DC-DC buck converter schematic diagram.

As shown in section 1.2.1, switched-mode DC-DC converters typically comprise regulator chips and passive components such as inductors, capacitors, and resistors. In order to develop a high-frequency and high-power DC-DC converter, the LTC 3630A (Linear Technology) [94] switching regulator chip was selected. The LTC 3630A is an integrated chip for a step-down DC-DC converter and contains power MOSFET switches and a feedback comparator to adjust the output voltage. The LTC 3630A can operate at a

switching frequency exceeding 1 MHz with input voltages of 4 - 76 V and maximum output current of 500 mA.

Figure 5.1 shows a schematic circuit diagram of the ultracompact DC-DC buck converter system with the LTC 3630A regulator chip and other components. The output voltage of the converter is adjusted by an external resistive divider as calculated from the equation [94]:

$$V_{\text{out}} = 0.8 \cdot (1 + \frac{R_1}{R_2}) \tag{5.1}$$

In this converter design, the output voltage was set to 20 V by adopting 150 kΩ and 5.6 kΩ resistors for $R_1$ and $R_2$, respectively. Once the output voltage was selected, the inductance was determined to set the switching frequency using the following equation:

$$f_{\text{sw}} = \frac{(V_{\text{in}} - V_{\text{out}}) \cdot D}{2 \cdot \Delta i_{\text{L}} \cdot L} \tag{5.2}$$

where $D$ is the duty ratio ($V_{in}$ / $V_{out}$), and $\Delta i_{\text{L}}$ is the inductor ripple current [A]. In order to operate the converter at the switching frequency as high as 1 MHz, approximately 6 µH inductance was required. Therefore, the converter was designed to operate with fixed output voltage of 20 V and output power of 10 W at the switching frequency of approximately 1 MHz. The design specification for the high-frequency and high-power ultracompact DC-DC buck converter is shown in Table 5.1.

Table 5.1 Converter specification

| | |
|---|---|
| Input voltage | 30 – 70 V |
| Output voltage | 20 V |
| Duty ratio | 1.5 – 3.5 |
| Switching frequency | ~ 1 MHz |
| Output current | 500 mA |
| Output power | 10 W |
| Inductor ripple current | < 1A |
| Inductance | ~ 6 µH |
| $R_1$ | 150 kΩ |
| $R_2$ | 5.6 kΩ |

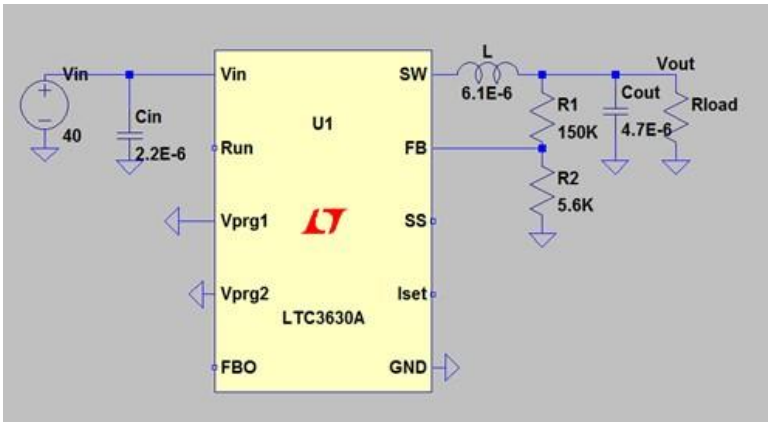


Figure 5.2 Schematic diagram of the converter circuit simulated with LTspice.

In order to verify the converter design a simulation has been conducted using LTspice provided by Linear Technology. Figure 5.2 shows a schematic diagram of the converter circuit simulated. In the simulation, the passive components were operated as an ideal case meaning that they are lossless and the values are not frequency-dependent. As an example of the simulation, Figure 5.3 illustrates the resulting waveforms from the output load and the inductor, when an input voltage of 40 V is applied. It is demonstrated that the output voltage and current are 20 V and 570 mA, respectively. It is also observed that the inductor ripple current is approximately 600 mA and the switching frequency is approximately 1.2 MHz. The simulation result verifies the high switching frequency (> 1 MHz) and the high output power (> 10 W) of the designed DC-DC converter.

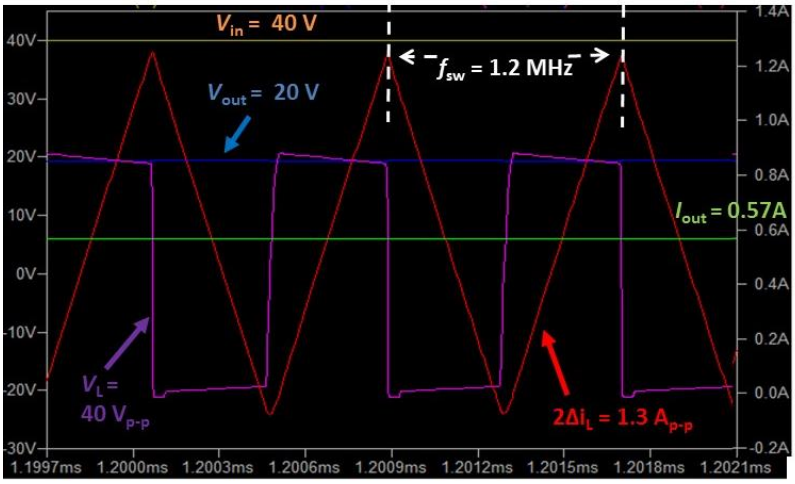


Figure 5.3 Simulation result from the circuit diagram in Figure 5.2.

## 5.3 Development of Ultracompact DC-DC Converter

### 5.3.1 Nanolaminated CoNiFe Core Inductor Preparation

In order to realize the ultracompact DC-DC converter, two nanolaminated CoNiFe cores were prepared: 1) toroidal core and 2) bar-shaped core. The toroidal core comprised 1500 layers of 1 µm-thick CoNiFe laminations, having outer diameter of 5.3 mm and inner diameter of 2.7 mm. An inductor was fabricated by winding 12-turn magnet wire around the core as shown in the inset of Figure 5.4 (a). The bar-type core comprised 2000 layers of 1 µm-thick CoNiFe laminations, having length of 10 mm and width of 2 mm. An inductor was fabricated by winding 22-turn magnet wire around the core as shown in the inset of Figure 5.4 (b).

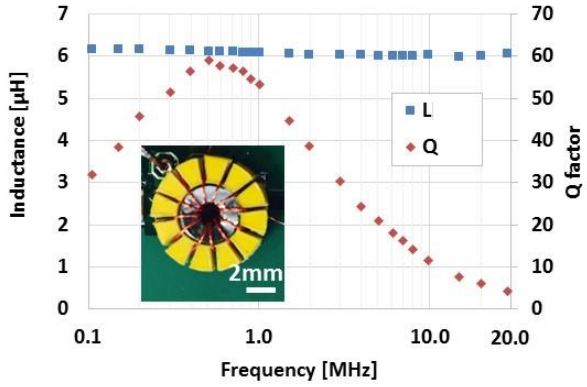


(a)

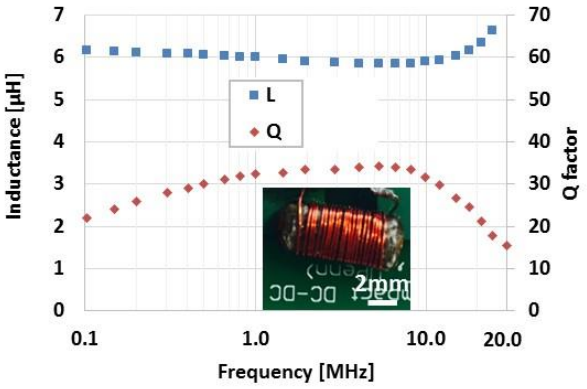


(b)

Figure 5.4 Inductance and quality factor of (a) 12-turn toroidal inductor and (b) 22-turn bar inductor

Both the toroidal and the bar inductors with nanolaminated CoNiFe cores were characterized over the 0.1 - 20 MHz frequency range using an impedance analyzer. As shown in Figure 5.4 (a), the toroidal inductor exhibits a constant inductance of 6.1 µH up to 20 MHz with a quality factor exceeding 50 at 1 MHz. The bar-type inductor exhibits a constant inductance of 6.1 µH up to 20 MHz with a quality factor reaching 35 at 1 MHz. Properties of both inductors are compared in Table 5.2. Note that the bar inductor possesses larger core volume and number of windings to achieve the required inductance (6.1 µH) due to the lower effective permeability resulting from the open magnetic path of the bar core.

Table 5.2 Comparison of inductors with nanolaminated CoNiFe core

| | Toroidal inductor | Bar inductor |
|---|---|---|
| Number of windings | 12 | 22 |
| Core surface area | 16.3 $mm^2$ | 20 $mm^2$ |
| Core thickness | 1.5 mm | 2 mm |
| Core volume | 24.5 $mm^3$ | 40 $mm^3$ |
| Single layer thickness | 1 µm | 1 µm |
| Number of layers | 1500 | 2000 |
| Inductance | 6.1 µH up to 20 MHz | 6.1 µH up to 20 MHz |
| Quality factor | 50 (@ 1 MHz) | 35 (@ 1 MHz) |

### 5.3.2 Fabrication of Ultracompact Converter on PCB

Using the nanolaminated CoNiFe core inductor, the designed ultracompact DC-DC buck converter was fabricated on PCB. Surface-mount-components (e.g., regulator chip, capacitors and resistors) were placed and soldered on designated pads on the PCB. The surface-mount-components utilized in this circuit are presented in Table 5.3.

Table 5.3 Components utilized for ultracompact DC-DC buck converter

| Name | Part number | Type | Parameter | Qty | Vendor |
|---|---|---|---|---|---|
| $C_{in}$ | 1276 | Capacitor | 2.2 µF, 100 V | 1 | Samsung EM |
| $C_{out}$ | 1276 | Capacitor | 4.7 µF, 35 V | 1 | Samsung EM |
| $R_1$ | MCT0603 | Resistor | 150 k, 1/8 W | 1 | Vishay |
| $R_2$ | MCT0603 | Resistor | 5.6 k, 1/8 W | 1 | Vishay |
| Connector | 5012 | Test point | | 4 | Keystone |
| LTC3630A | LTC3630A | Step-down switch | | 1 | Linear Technology |

Figure 5.5 shows images of the developed ultracompact DC-DC converter. Top view of the ultracompact DC-DC converter is shown in Figure 5.5 (a) and (b), demonstrating the total surface area less than 100 $mm^2$. As shown in Figure 5.5 (c), fabricated inductor is connected through via-holes, being embedded at the bottom of the PCB to reduce the surface area of the converter. The total thickness of the converter including the PCB is less than 2 mm as shown in Figure 5.5 (d).

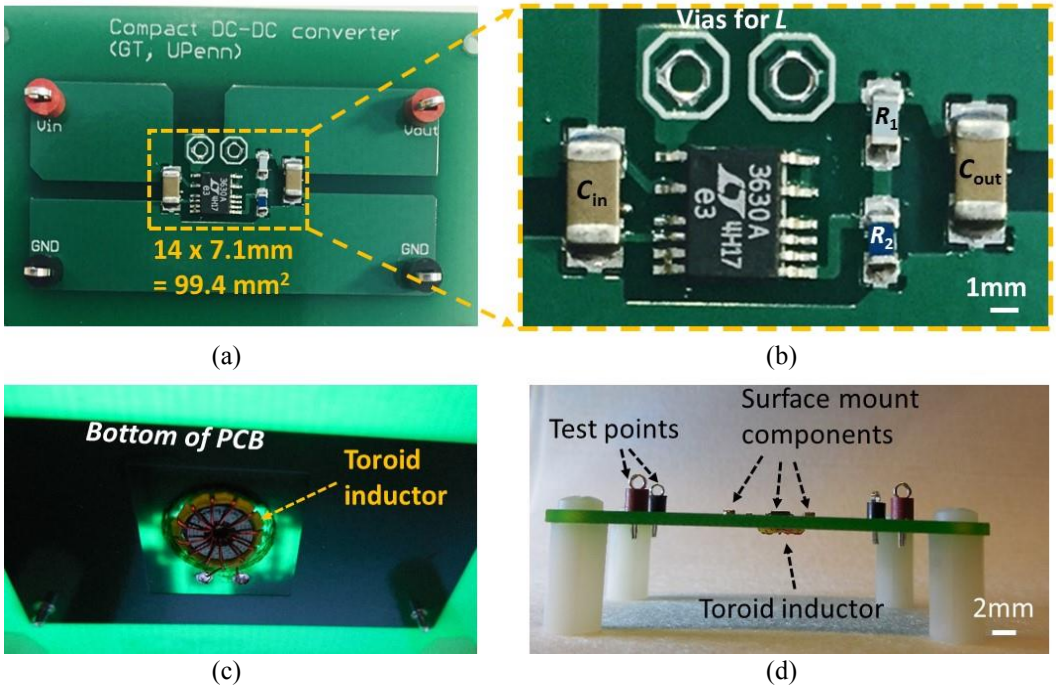


Figure 5.5 Images of ultracompact DC-DC converter. (a) and (b) top view, (c) bottom view showing inductor, and (d) side view.

## 5.4 Characterization of Ultracompact DC-DC Converter

During the converter operation, the output voltage was fixed at 20 V as designed. Input voltages ranging from 30 V to 70 V were applied using a DC power supply (HY10010EX, VOLTEQ). Input, output, and inductor voltages were measured using an oscilloscope (TDS 2024C, Tektronix), and the output current was obtained by measuring the voltage through a 1 Ω resistor at the output load.

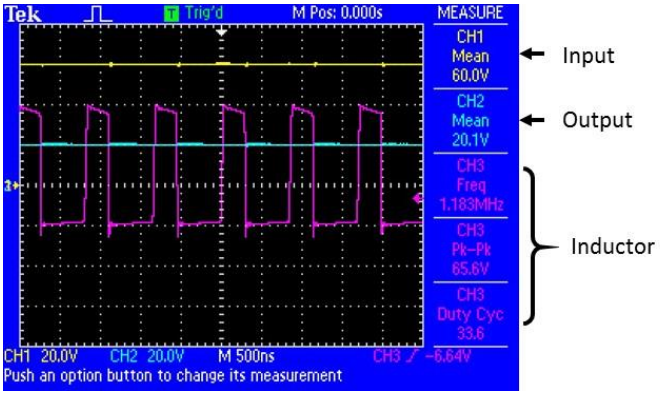


Figure 5.6 Captured waveforms from the oscilloscope.

Figure 5.6 shows an example of a captured image from the oscilloscope, demonstrating the output voltage of 20.1 V and the switching frequency of 1.18 MHz. In this figure, the converter was operated at an input voltage of 60 V.

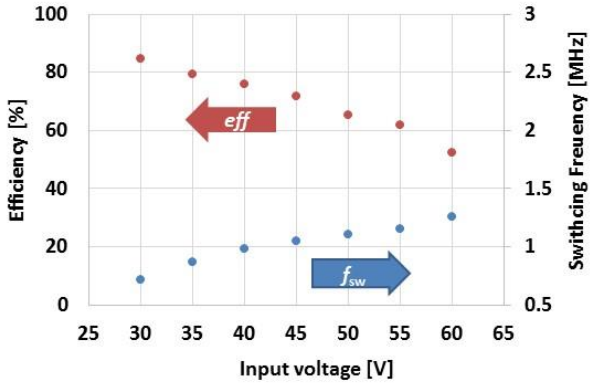


(a)

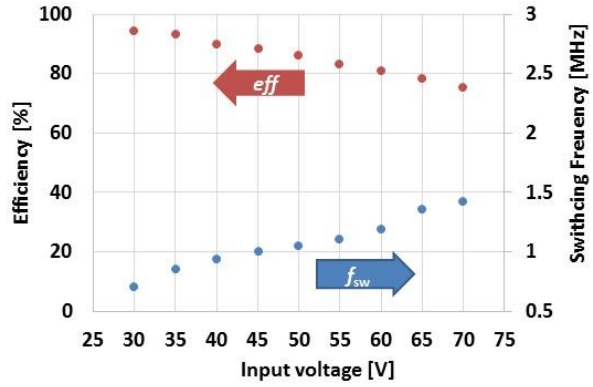


(b)

Figure 5.7 Measured efficiency and switching frequency as a function of input voltage, when the converter operated with (a) toroidal inductor and (b) bar inductor

Figure 5.7 shows the converter efficiency and the switching frequency of the ultracompact DC-DC converter as a function of input voltage. As shown in Figure 5.7 (a), the efficiency of the converter fabricated with the toroidal inductor is 84.6 % at an input voltage of 30 V. The efficiency decreases with increasing input voltage (i.e., increasing duty ratio) and 52.16 % efficiency was observed at an input voltage of 60 V. During the measurement, the switching frequency varies between 0.7 - 1.26 MHz as shown in the graph. The measured efficiency of the converter fabricated with the bar inductor is shown in Figure 5.7 (b). The efficiency of the converter is 94.25 % at an input voltage of 30 V and 75.43 % at an input voltage of 70 V, demonstrating higher converter efficiency compared to the converter fabricated with the toroidal inductor. The switching frequency varies between 0.7 - 1.42 MHz during the measurement.

In order to investigate the dependence of the converter efficiency on inductor geometry, the peak operation flux densities of the nanolaminated CoNiFe cores in each of these inductors was investigated. The peak inductor current during converter operation can be calculated from equation (1.10), which can be expressed as:

$$\Delta i_L = \frac{(V_{in} - V_{out}) \cdot D}{2 \cdot L \cdot f_{sw}} \tag{5.3}$$

Also, the peak flux density in the magnetic core during the converter operation is calculated as:

$$B_{peak} = \frac{L \cdot \Delta i_L}{N \cdot A_c} \tag{5.4}$$

where $A_c$ is the core cross-section area [$m^2$]. Note that the peak flux density is not reaching the saturation flux density of CoNiFe (i.e., the peak flux density is within the linear permeability region of B-H hysteresis loop) when the output DC current is combined ($\Delta i_L$

+ $I_{out}$). Combining equations (5.3) and (5.4), the peak flux density of the nanolaminated CoNiFe core during the converter operation becomes:

$$B_{peak} = \frac{(V_{in} - V_o) \cdot V_o}{2 \cdot f_{sw} \cdot N \cdot A_c \cdot V_{in}} \tag{5.5}$$

Using equation (5.5) and the core dimensions presented in Table 5.2, the peak operation flux densities of both toroidal core and bar core are 0.21 T and 0.11 T, respectively, verifying that both nanolaminated CoNiFe cores were operated in the regimes less than the saturation flux density of CoNiFe (1.8 T) for high power (10 W) conversion. Once the peak operation flux densities are known, the core power losses can be estimated based on the core power loss coefficients ($k_{hyst}$ for the hysteresis loss coefficient and $k_{eddy}$ for the eddy-current loss coefficient) in chapter 3.5.3 (Figure 3.21):

$$P_{core} = (k_{hyst} f + k_{eddy} f^2) \times V_{core} = (P_{hyst} + P_{eddy}) \times V_{core} \tag{5.6}$$

where $P_{core}$ is the core power loss, $P_{hyst}$ is the hysteresis core loss, $P_{eddy}$ is the eddy current loss, and $V_{core}$ is the volume of the core. Table 5.4 shows the estimated core loss using equation (5.6), compared with measured converter power losses.

Although such comparisons should be made with care due to the difference in inductor excitation waveforms between the high-flux measurement and converter measurement, it can be stated the core loss ($P_{core}$) dominates the total converter power loss ($P_{loss}$) from the table. However, as the input voltage increases (i.e., the duty ratio increases), the core loss becomes less dominant, implying that other losses (e.g., conduction loss in PCB, Joule heating, switching loss) increase rapidly with increasing input voltage.

Table 5.4 Comparison of converter power loss with estimated core loss

| | Converter performance | | | | | | Core loss estimation | | | |
|---|---|---|---|---|---|---|---|---|---|---|
| | $V_{in}$ | $V_{out}$ | $f_{sw}$ | $P_{in}$ | $P_{out}$ | $P_{loss}$ | $\Delta B_{pk}$ | $P_{hyst}$ | $P_{eddy}$ | $P_{core}$ |
| Converter with toroidal inductor | 30 | 20 | 0.71 | 10.76 | 9.11 | 1.66 | 0.201 | 1.49 | 0.04 | 1.53 |
| | 35 | 20 | 0.87 | 11.67 | 9.28 | 2.39 | 0.212 | 2.02 | 0.06 | 2.09 |
| | 40 | 20 | 0.98 | 13.40 | 10.18 | 3.22 | 0.218 | 2.43 | 0.09 | 2.52 |
| | 45 | 20 | 1.05 | 15.48 | 11.08 | 4.40 | 0.227 | 2.81 | 0.11 | 2.91 |
| | 50 | 20 | 1.10 | 17.55 | 11.44 | 6.11 | 0.233 | 3.12 | 0.12 | 3.24 |
| | 55 | 20 | 1.15 | 18.92 | 11.72 | 7.20 | 0.237 | 3.36 | 0.14 | 3.50 |
| | 60 | 20 | 1.26 | 20.40 | 10.64 | 9.76 | 0.226 | 3.36 | 0.15 | 3.51 |

| | Converter performance | | | | | | Core loss estimation | | | |
|---|---|---|---|---|---|---|---|---|---|---|
| | $V_{in}$ | $V_{out}$ | $f_{sw}$ | $P_{in}$ | $P_{out}$ | $P_{loss}$ | $\Delta B_{pk}$ | $P_{hyst}$ | $P_{eddy}$ | $P_{core}$ |
| Converter with toroidal inductor | 30 | 20 | 0.70 | 11.70 | 11.02 | 0.67 | 0.100 | 0.59 | 0.01 | 0.60 |
| | 35 | 20 | 0.85 | 12.22 | 11.37 | 0.85 | 0.106 | 0.81 | 0.02 | 0.83 |
| | 40 | 20 | 0.94 | 13.03 | 11.68 | 1.35 | 0.111 | 0.99 | 0.03 | 1.02 |
| | 45 | 20 | 1.00 | 13.59 | 11.98 | 1.61 | 0.116 | 1.15 | 0.04 | 1.19 |
| | 50 | 20 | 1.04 | 14.12 | 12.13 | 1.99 | 0.120 | 1.28 | 0.05 | 1.33 |
| | 55 | 20 | 1.10 | 14.29 | 11.90 | 2.39 | 0.121 | 1.37 | 0.05 | 1.42 |
| | 60 | 20 | 1.18 | 13.56 | 10.97 | 2.59 | 0.118 | 1.40 | 0.06 | 1.46 |

Investigation on the loss estimation also demonstrates that the lower efficiency of the toroidal inductor mainly results from the higher peak operation flux density of the toroidal core. Therefore, it should be concluded that the toroidal core enables a higher inductance density than the bar core due to the closed magnetic path; however, its higher operation flux density leads the lower efficiency of the ultracompact DC-DC converter. The properties of the ultracompact DC-DC converter are summarized in Table 5.5.

Table 5.5 Properties of the ultracompact DC-DC converter

| | With toroidal inductor | With bar inductor |
|---|---|---|
| Converter Surface area [$mm^2$] | 99.4 | 99.4 |
| Converter Volume [$mm^3$] | 198.8 | 198.8 |
| Input voltage [V] | 30 - 60 | 30 -70 |
| Output voltage [V] | 20 | 20 |
| Output current [A] | 0.5 | 0.5 |
| Output power [W] | 10 | 10 |
| Switching frequency [MHz] | 0.7 - 1.26 | 0.7 - 1.42 |
| Power density [$W/cm^2$] | 10.06 | 10.06 |
| Efficiency [%] | 52.16 - 84.6 | 75.43 - 94.25 |

## 5.5 Comparison of Ultracompact DC-DC Converter with Other Converters

In this section, the performance of the ultracompact DC-DC converter is compared with other DC-DC converters integrated with magnetic cores (i.e., PSiP and PSoC) as well as commercial DC-DC converter modules as shown in Table 5.6. Since each DC-DC converter is operated under different conditions (e.g., input and output voltages, duty ratio, power, and switching frequency), it is hard to establish simple figures of merit to directly compare them. Instead, important detailed parameters for converter performance are presented in Table 5.6.

Table 5.6 Performance of DC-DC converters with integrated magnetics

| Ref. | $P_{o\_d}$ [W/cm$^2$] | $P_o$ [W] | $\eta$ [%] | $f_{sw}$ [MHz] | $I_o$ [A] | $V_{in}$ [V] | $V_{out}$ [V] | $L_{\_density}$ [nH/mm$^2$] | L [nH] | Core material | |
|---|---|---|---|---|---|---|---|---|---|---|---|
| [41] | 6.25 | 10 | 88 | 0.5 | 3 | 5 | 3.3 | 2.26 | 880 | MnZn | ↑ Researched DC-DC converter |
| [42] | 8.16 | 1 | 83 | 1.8 | 0.2 | 3.6 | 1.5 | 89.8 | 1100 | NiZn | |
| [43] | 6.25 | 10 | 90 | 0.5 | 3 | 5 | 3.3 | 4.75 | 1900 | MnZn | |
| [44] | 1.44 | 0.36 | 91 | 2 | 0.2 | 3.6 | 1.8 | 100 | 2500 | NiZnCu | |
| [45] | 2.04 | 16 | 78 | 1.3 | 16 | 5 | 1 | 0.13 | 100 | NiZn | |
| [46] | 4 | 0.36 | 80 | 6 | 0.5 | 3.6 | 1.8 | 43.3 | 390 | NiZn | |
| [47] | 16.78 | 24 | 80 | 5 | 20 | 12 | 1.2 | 0.17 | 24 | NiZn | |
| [48] | 10.42 | 0.6 | 90 | 2.8 | 0.3 | 3.6 | 1.8 | 277.8 | 1060 | NiZn | |
| [50] | 1 | 1 | 83.3 | 3 | 0.35 | 4.5 | 3 | 60 | 960 | CoHfTa | |
| [54] | 0.32 | 0.54 | 74 | 8 | 0.45 | 3.6 | 1.2 | 38.26 | 440 | NiFe | |
| This work | 10.26 | 10.2 | 75.9 | 0.98 | 0.51 | 40 | 20 | 238 | 6100 | CoNiFe (toroid) | |
| | 10.99 | 10.9 | 75.4 | 1.2 | 0.55 | 60 | 20 | 232 | 6100 | CoNiFe (bar) | ↓ |
| [56] | 5.85 | 1.17 | 80 | 4 | 0.65 | 5 | 1.8 | | N/A | | Commercial Module |
| [57] | 9.6 | 0.72 | 94 | 2 | 0.2 | 5.5 | 3.6 | | N/A | | |
| [58] | 4.8 | 4.8 | 85 | 0.33 | 0.6 | 36 | 8 | | N/A | | |
| [59] | 10 | 0.9 | 80 | 4 | 0.5 | 5.5 | 1.8 | | N/A | | |

Based on Table 5.6, a detailed analysis on converter performance as a function of the magnetic core inductor performance has been conducted. From Table 5.6, it is demonstrated that the DC-DC converters are typically operated at the switching frequencies of 0.5 – 8 MHz. However, the switching frequency is mostly limited by the switching ICs rather than the magnetic components. Most of the inductors exhibit constant inductances and high quality factors up to tens of MHz.

For the DC-DC buck converter design, the inductance is determined by input voltage, output voltage, and ripple current for a given switching frequency as represented

in equation (1.10). Consequently, the higher inductance is desirable for high voltages, conversion ratio, and ripple current. Use of the magnetic core certainly increases the inductance density resulting in small volume for a given inductance; however, one should consider the saturation of the magnetic core that limits the output current and, therefore, the output power. Most of the converters in Table 5.6 operate with output current less than 0.5 A, which is near the saturation current of the magnetic core inductor. High permeability of the magnetic core enables high inductance density, while reducing the saturation current. Winding a greater number of turns around a given core results in the same trend (i.e., higher inductance density and lower saturation current). Increasing magnetic thickness (and volume) without laminations is also not a solution to achieve both high inductance density and high saturation current since it causes significant eddy-current losses during high-frequency operation.

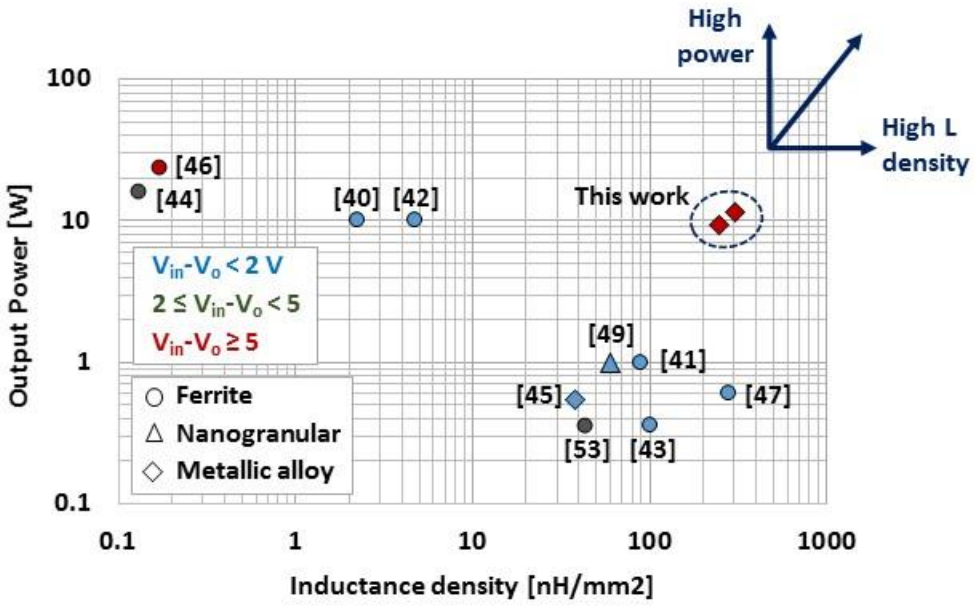


Figure 5.8 Output power versus inductance density of DC-DC converter with integrated magnetics. The color shows the input and output voltage difference ($V_{in}$ - $V_{out}$), and the shape represent the magnetic core material. Note that the commercial modules are not included due to the rack of inductor information.

In order to compare the data in Table 5.6 in graphical form, several key parameters are plotted in the following figures. Figure 5.8 shows the converter power as a function of inductance density. The shape of the data point represents the magnetic core material and the color represents the input and output voltage difference ($V_{in} - V_{out}$). Note that commercially available converter modules are not included due to lack of inductor specification. The output power ranges from 0.5 to 20 W and the inductance density varies from 0.1 to 300 nH/mm$^2$ with a switching frequency near 1 MHz. As expected, high power converters demonstrate lower inductance density and vice versa. In case of [44, 47], the inductor has 2 – 4 turns of windings with large volume of low permeability (< 10) magnetic core, resulting in high output power but low inductance density (one practical effect of this is that converters with large $V_{in}$-$V_{out}$ require large physical volumes). Microfabricated inductors with nanogranular film cores [50] or metallic alloy cores [46] show high inductance density, but the converters operated with low output power. However, it is demonstrated that use of laminated cores enables both high inductance density and high power due to its large magnetic volume and suppressed eddy-current losses.

Figure 5.9 shows the converter efficiency as a function of switching frequency. The color of the data point represents the conversion ratio ($V_{out} / V_{in}$). Commercially available converter modules are also included in the graph. The converter efficiency ranges from 74% to 94% and the switching frequency varies from 0.4 to 8 MHz. Typically, the efficiency tends to decrease with increasing conversion ratio for a given switching frequency. However, in order to perform reliable analysis on the converter efficiency, the converter losses need to be investigated, for example, by separating them into switching loss, conduction loss, and magnetic loss. It cannot be concluded that the converter

efficiency is solely attributable to the inductor performance based on Table 5.6 since each converter uses different switching chips and circuitries. It should also be noted that the switching frequency is mostly limited by the switching ICs rather than the magnetic components. The inductors in Table 5.6 show constant inductances and high quality factors up to tens of MHz.

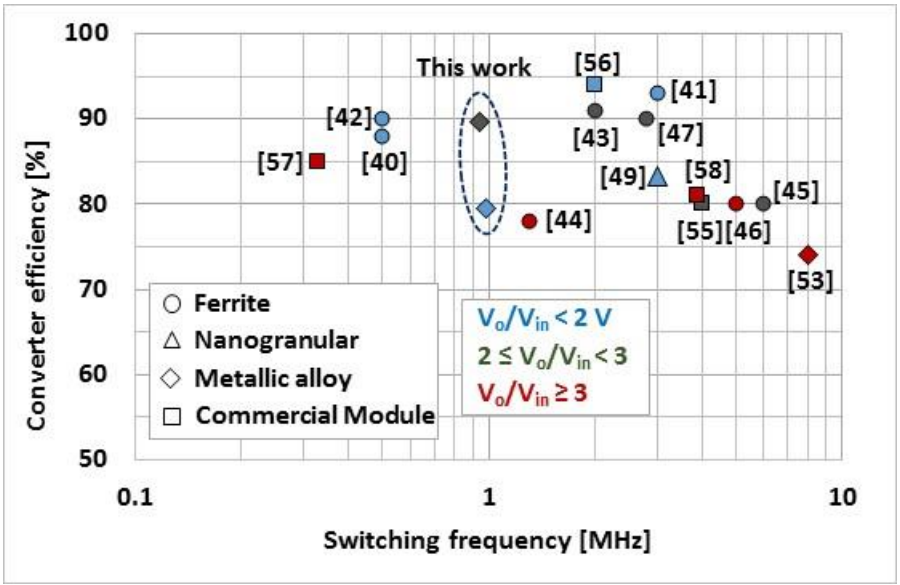


Figure 5. 9 Converter efficiency versus switching frequency of DC-DC converter with integrated magnetics. The color shows the conversion ratio ($V_{out}$ / $V_{in}$), and the shape represents the magnetic core material.

## 5.6 Conclusions

In this chapter, we demonstrated an ultracompact DC-DC converter on PCB with surface-mount-components and a nanolaminated CoNiFe core inductor. Two types of inductors (i.e., toroid inductor and bar inductor) were utilized and the converter operated with output power over 10 W at the switching frequency of 0.7 – 1.4 MHz, demonstrating conversion efficiency of 94.2 % at 30 V input and 80.8 % at 60 V input.

It was also tempting to compare the ultracompact converter with previously reported DC-DC converters integrated with magnetic components, demonstrating that the ultracompact

converter exhibited both high output power and inductance density due to the nanolaminated core (which enables high inductance density with suppressed eddy-current losses). When the converters are compared, care should be taken since the converter properties (e.g., switching frequency, converter efficiency, and conversion ratio) also depend on other components including ICs, capacitors, and conductors.

# CHAPTER 6

# CONCLUSION

## 6.1 Summary of Conducted Research

In accordance with the objective of the proposed research, nanolaminated soft magnetic metallic alloy cores for high-frequency (> 1MHz) and high-power (> 10 W) ultracompact power converters have been demonstrated.

In chapter 3, fabrication and characterization of nanolaminated soft magnetic metallic alloy cores were presented. For the metallic alloy, both permalloy ($Ni_{80}Fe_{20}$) and $Co_{44}Ni_{37}Fe_{19}$ were electrodeposited, demonstrating the superior magnetic properties (i.e., higher saturation flux density and lower coercivity) of CoNiFe over permalloy. Anisotropic CoNiFe was also electrodeposited to further improve the magnetic properties, demonstrating higher effective permeability and lower volumetric power loss at high frequency operation. The three metallic alloys utilized to fabricate as nanolaminated magnetic cores based on sequential electrodeposition of alternating layers of the metallic alloy and sacrificial copper, followed by sacrificial layer removal. Two approaches were developed for the nanolaminated core fabrication: 1) SU-8 post approach and 2) surface-tension-driven assembly. The SU-8 post approach utilized vertical support holes where insulating SU-8 photoresist is applied. Once the SU-8 was cross-linked, it anchored each magnetic layer after the sacrificial copper layer removal. Therefore, the final structure became an air-insulated nanolaminated core where each magnetic layer is supported by insulating SU-8 posts. In case of the surface-tension-driven assembly, each CoNiFe nanolamination was assembled based on surface tension at the liquid-air interface, resulting in a polymer-insulated nanolaminated core where each magnetic layer is encapsulated with

a polymeric insulating material (i.e., fluoroacrylate). Both approaches realized nanolaminated cores that consist of tens to hundreds of layers of alternating metallic alloy and insulting material. Compared to the SU-8 post approach, the surface-tension-driven assembly has advantages including achievable number of layers and ease of fabrication.

Characterization of the nanolaminated cores was also presented in chapter 3. For the reliable characterization of the nanolaminated cores, three different types of characterizations were performed consecutively: 1) low flux *in situ* characterization using impedance analyzer; 2) high flux characterization under large signal AC flux conditions; and 3) system level characterization in DC-DC converters. Through the characterization, it was demonstrated that substantial magnetic volume for high power was achieved from the stacked multiple magnetic and insulating layers, while eddy currents were suppressed in the magnetic nanolaminations. It was also observed that the superior magnetic properties of CoNiFe (i.e., higher saturation flux density and lower coercivity) result in higher operational flux density and lower volumetric power losses of the nanolaminated CoNiFe core, compared to the nanolaminated permalloy core.

In chapter 4, the nanolaminated CoNiFe cores were integrated into microfabricated inductors for on-chip power supply application. Two different microfabrication techniques were conducted for the integrated inductors with the nanolaminated CoNiFe cores: 1) core drop-in approach where pre-fabricated cores are incorporated as an intermediate step in the fabrication of inductor windings; and 2) direct winding approach where inductor windings are directly fabricated on encapsulated magnetic core. Both fabrication approaches enabled integration of a large volume core (for high power handling) into the inductor windings. Utilizing the microfabrication techniques, toroidal and bar-type microfabricated inductors

with the nanolaminated CoNiFe cores were developed, demonstrating a high inductance of 2 µH up to 10 MHz and peak quality factor of 36 at 5 MHz.

In chapter 5, an ultracompact DC-DC buck converter was developed on PCB with commercially available surface-mount-components (i.e., a regulator chip, capacitors and resistors) and a nanolaminated CoNiFe core inductor. The footprint of the ultracompact converter was 14 × 7.1 $mm^2$ and the input voltage of the converter was ranging from 30 to 70 V, while the output voltage was fixed at 20 V. The converter operated with output power over 10 W at the switching frequencies of 0.7 – 1.4 MHz, demonstrating conversion efficiency of 94.2 % at 30 V input and 80.8 % at 60 V input.

## 6.2 Suggestions for Future Research

Based on automated sequential electrodeposition followed by selective removal of sacrificial metallic layer (i.e., copper), we have synthesized a nanolaminated magnetic material of macro-scale volume, achieving both high overall energy storage capability and suppression of eddy currents at MHz operation frequencies. In concluding this thesis, this section comprises suggestions for future work based on the intellectual achievements of this research.

### 6.2.1 Applications Where the Nanolaminated Magnetic Core is the Most Suitable

This research mainly focused on fabrication and characterization of nanolaminated metallic alloy cores. Although the core was tested in a converter circuit, it is necessary to find the optimal DC-DC converter application in which the nanolaminated metallic alloy core can be fully-utilized. Table 6.1 presents several application areas where a switched-mode DC-DC buck converter is used.

Table 6.1 Applications where DC-DC converter is used

| Application | $P_{out}$ [W] | $V_{in}$ [V] | $V_{out}$ [V] | $I_{out}$ [A] | $f_{sw}$ [MHz] | *Eff* [%] | Ref. |
|---|---|---|---|---|---|---|---|
| Line-interfaced LED drivers | 3 - 12 | AC-line voltage | 10 - 45 | 0.3 - 0.7 | 0.05 - 0.1 | 64 - 80 | [93] |
| Phone charger | ~ 5 | AC-line voltage | 5 | 0.7 - 1 | ~ 0.07 | 63 - 77 | [95, 96] |
| Tablet PC Charger | ~ 10 | AC-line voltage | ~ 5.1 | ~ 2 | ~ 0.1 | ~ 70 | [97] |
| Laptop charger | ~ 60 | AC-line voltage | 12 - 25 | 3.25 | ~ 0.05 | ~70% | [98] |
| Point of Load (Processors in electronic devices) | > 10 | 2.5 - 14 | 0.6 - 5 | 0.4-5 | 0.5 – 5 | 80 - 93 | [99, 100] |
| Automotive DC adapter | 0.3 - 1 | 12 V | 3.3 – 5 | 0.3 | 0.1 – 0.5 | 83 | [101] |

A point of load converter, which typically provides a converted voltage (e.g., from 5 V to 3.3 V) to microprocessors in electronic devices, is the most widely researched area for integrated magnetic components [2, 47]. Since the point of load converter requires relatively low power (e.g., < 3W), it can benefit from integrated magnetic components. However, the nanolaminated metallic alloy core, which enables larger magnetic volume with suppressed eddy-current losses, can be used in other application areas that require relatively high power than the point of load converter.

If the nanolaminated CoNiFe core is utilized for power supply applications (e.g., line-interface LED drivers or portable device chargers), the core needs to be integrated into a transformer to achieve an isolated DC-DC converter. Currently, most chargers for electronic devices adopt a rectifier and a reservoir capacitor for AC-DC conversion (e.g.,

110 $V_{ac}$ to 155 $V_{dc}$) followed by an isolated DC-DC converter having a flyback topology (e.g., 155V to 5V). The transformer is the essential component of the flyback converter that isolates the electronic device from the high voltage input [4]. Since the power supplies for portable electronics use a switching frequency of several tens of kHz (e.g., 70 kHz for iPhone charger [95]), the required inductance of the transformer is approximately hundreds of μH, which is higher than the presented inductance in this research. However, such high inductance can be achievable by increasing magnetic volume (i.e., stacking larger number of laminations) enabled by the surface-tension-driven approach. Use of higher switching frequency is also a promising solution to reduce the required inductance value.

Recently introduced merged two-stage architecture [93] for both wide-range DC voltage and AC-line voltage can be used as an alternative for the typical power supply system. In the merged two-stage architecture, the first stage is a variable-topology switched-capacitor circuit operating at tens to hundreds of kHz, achieving high power density and efficiency since it employs only switches and capacitors. It converts the input voltage to the voltage levels (e.g., tens of volts) for which the second stage needs to operate. The second stage is designed as a high-frequency buck converter where the nanolaminated magnetic core is beneficial. In [93], it is demonstrated that the merged two-stage architecture achieved both wide-range DC-DC and AC-DC conversion with high efficiency and high power density.

### 6.2.2 More Geometries of Core and Inductor

During this research, two cores of different geometries (i.e., toroidal core and bar core) were operated in the ultracompact DC-DC converter. The toroidal core possesses a closed magnetic path, enabling higher effective permeability (resulting in higher

inductance density) than the bar core. However, the higher effective permeability of the core can result in a lower saturation current, hence a lower converter power density, resulting in lower efficiency of DC-DC converter at a given output current (and power). In contrast, the lower effective permeability of the bar core due to an open magnetic path allows a higher saturation current, resulting in higher efficiency of DC-DC converter, while the inductance density is smaller.

From the experiment with two different core geometries (i.e., closed magnetic path and open magnetic path), it is worthwhile to investigate *air-gap* toroid cores of which one can adjust the effective permeability of the core. It can enable the development of a magnetic core with an optimized effective permeability that simultaneously achieves both high inductance density as well as high efficiency and output power of the DC-DC converter. In addition, it will be also interesting to study different geometry inductors such as spiral or race-track shape inductors with the nanolaminated CoNiFe core.

### 6.2.3 Improved Magnetic Material

For energy storage/transfer applications, electrodeposited soft magnetic metallic alloys have been widely researched as shown in chapter 2. In this research, we demonstrated that electrodeposited CoNiFe is one of the most promising metallic alloys due to its high saturation flux density and low coercivity, showing its usefulness as a magnetic core for high-frequency and high-power DC-DC converter. The properties of the electrodeposited CoNiFe for the DC-DC converter application can be further improved by adjusting its relative permeability as well as electrical resistivity. A few research efforts have been reported for electrodeposited CoNiFe thin film with high resistivity by adding additives such as diethylenetriamine (DET) [102] or thiourea [103] in the electrodeposition

bath. Adopting the modified electrodeposition bath to the sequential electrodeposition system can result in high performance nanolaminated CoNiFe cores.

Since we demonstrated that a bar-shaped, anisotropic nanolaminated CoNiFe core shows improved magnetic properties in chapter 3.8, it is worthwhile to study how to realize batch fabrication of toroidal-shaped, anisotropic nanolaminated CoNiFe cores.

### 6.2.4 Surface-Tension-Driven Assembly

In order to develop highly-laminated magnetic cores, we introduced a surface-tension-driven assembly technique, resulting in more than hundreds of layers of thin CoNiFe. Chapter 3.4.2 showed characterization of the assembly technique, demonstrating a critical gap that determines the minimum gap between thin films for successful assembly. The surface-tension-driven assembly can be further improved when more investigations and characterizations are performed. For example, it is worthwhile to study the achievable minimum thickness of the nanosheet. When the thickness of a CoNiFe film with outer diameter of 5 mm is less than 500 nm, a deformation of the film was observed which results in winkled films, tangled films, or films attached to the wire. However, the thickness can be thinner with reduced film diameter since the deflection of the thin film depends on both thickness and diameter (the deflection of the rectangular thin film is proportional to $1/t^3$ and $L^4$, where $t$ is the thickness and $L$ is the length of the film [104]).

Other suggestions regarding the surface-tension-driven assembly include: 1) studying the effect of etch holes of the nanosheets in terms of film alignment; 2) performing the assembly technique with different materials (e.g., different materials and shapes of the film, different polymeric solutions) that can be applicable for different applications; 3) performing the assembly technique with different pull-up parameters (e.g., adjusting the

pull-up speed, applying vibration using ultrasonication or mechanical wobbling during the pull-up); and 4) full automation of the assembly process.

### 6.2.5 Magnetic Domain Characterization

In chapter 3.6, fabrication and characterization of the nanolaminated CoNiFe cores were presented. Although the improved magnetic properties of the anisotropic (hard-axis) core were demonstrated, an investigation on the magnetic domain orientation of the anisotropic core will help to understand the behavior of the anisotropic core. Observing the magnetic domains of the film can be enabled using Kerr-effect microscopy [105, 106] or MFM (magnetic force microscopy) [107]. It will be also interesting to compare the magnetic domain orientation of multilayer CoNiFe film with a single CoNiFe film.

### 6.2.6 Correlation between Each Characterization Stage

For the characterization of the nanolaminated magnetic cores in chapter 3.5, the cores were first operated under small signal excitation for low-flux (< 10 mT) characterization using an impedance analyzer. Then, the cores were characterized under large signal excitation for high-flux (> 100 mT) characterization using a designed LC resonant circuit because it is difficult to achieve such high flux using the impedance analyzer. However, since both characterizations were based on different principles, it is worthwhile to characterize the core within the transient range to correlate the small signal and large signal characterization. For example, the low-flux characterization can be conducted using the LC resonant circuit without use of an amplifier.

Further, the inductors are typically operated under triangular waveform current in DC-DC converters, while general characterization of the inductors was conducted by applying sinusoidal waveform. The effect of the non-sinusoidal waveforms on the eddy-

current loss of the magnetic core was studied numerically in [108]; however, the effect on the hysteresis loss requires an empirical analysis that can be performed in the future.

Also, applying DC bias current during the inductor test can enable the prediction of the effect of the output current in DC-DC converter operation.

### 6.2.7 Other Applications using Nanolaminated Metallic Alloys

Nanolaminated magnetic structures with high relative permeability can be utilized for various applications. Transformers using the nanolaminated magnetic core are a promising solution to realize an ultracompact, isolated DC-DC converter such as a flyback converter. Also, an inductive wireless power transfer using the nanolaminated magnetic core will be beneficial for realizing miniaturized power transfer systems.

# REFERENCES


[1] C. R. Sullivan, D. V. Harburg, J. Qiu, C. G. Levey, and D. Yao, "Integrating magnetics for on-chip power: a perspective," *IEEE Transactions on Power Electronics*, vol. 28, no.9, pp. 4342-4353, Sep. 2013.

[2] C. O. Mathuna, N. Wang, S. Kulkarni, S. Roy, "Review of integrated magnetics for power supply on chip (PwrSoC)," *IEEE Transactions on Power Electronics*, vol. 28, no. 11, pp. 4799-4816, Nov. 2012.

[3] Q. Li, M. Lim, J. Sun, A. Ball, Y. Ying, F. C. Lee, K. D. T. Ngo, "Technology road map for high frequency integrated dc-dc converter," *Applied Power Electronics Conference and Exposition (APEC)*, pp.533-539, Feb. 2010.

[4] D. W. Hart, "Power Electronics," New York, U.K.: McGraw-Hill, 2001. Ch. 6.

[5] R. W. Erickson, and D. Maksimovic, "Fundamentals of power electronics," London, U.K.: Springer, Jan. 2001.

[6] S. Chunlei, B. C. Walker, E. Zeisel, B. Hu, and G. H. McAllister, "A highly integrated power management IC for advanced mobile applications," *IEEE Journal of Solid-State Circuits*, vol. 42, no .8, pp. 1723-1731, Aug. 2007.

[7] D. J. Perreault, J. Hu, J. M. Rivas, Y. Han, O. Leitermann, R. C. N. P-Podgursk, A. Sagner, C. R. Sullivan, "Opportunities and challenges in very high requency power conversion," *Applied Power Electronics Conference and Exposition (APEC)*, pp.1-14, Feb. 2009.

[8] J. Lammeraner and M. Stafl, "Eddy Current," London, U.K.: Iliffe, 1966.

[9] G. Bertotti, "Hysteresis in Magnetism," London, U.K.: Academic, 1998.

[10] J. P. Barranger, "Hysteresis and eddy-current losses of a transformer lamination viewed as an application of the Poynting theorem," in NASA, Washington, DC, USA, NASA TN D-3114, 1965

[11] J. W. Park, "Core lamination technology for micromachined power inductive components," Ph.D. dissertation, Department of Electrical and Computer Engineering, Georgia Institute of Technology, Atlanta, GA, USA, Dec. 2003.

[12] D. Yao, C. G. Levey, R. Tian, C. R. Sullivan, "Microfabricated V-groove power inductors using multilayer Co-Zr-O thin films for very-high-frequency dc-dc converter," *IEEE Transactions on Power Electronics*, vol. 28, no. 9, pp. 4384-4394, Sep. 2013.

[13] K. Ikeda, K. Kobayashi, and M. Fujimoto, "Multilayer nanogranular magnetic thin films for GHz applications," *Journal of Applied Physics*, vol.92, no. 9, pp.5395-5400, Nov. 2002.

[14] P. Morrow, C- M. Park, H. W. Koertzen, and J.T. DiBene, "Design and fabrication of on-chip coupled inductors integrated with magnetic material for voltage regulators," *IEEE Transactions on Magnetics*, vol. 47, no. 6, pp. 1678-1686, Jun. 2011.

[15] Y. Fukuda, T. Inoue, T. Mizoguchi, S. Yatabe, and Y. Tachi, "Planar inductor with ferrite layers for dc-dc converter," *IEEE Transactions on Magnetics*, vol. 39, no. 4, pp. 2057-2061, Jul. 2003.

[16] I. Kowase, T. Sata, K. Yamasawa, Y. Miura, "A planar inductor using Mn-Zn ferrite/polyimide composite thick film for low-voltage and large-current dc-dc converter," *IEEE Transactions on Magnetics*, vol. 41, no. 10, pp. 3991-3993, Oct. 2005.

[17] S. Bae, Y.-K. Hong, J.-J. Lee, J. Jalli, G. S. Abo, A. Lyle, B. C. Choi, and G. W. Donohoe, "High Q Ni-Zn-Cu ferrite inductor for on-chip power module," *IEEE Trans. Magnetics*, vol. 45, no. 10, pp. 4773-4776, Oct. 2009.

[18] (online) Available: www.allstarmagnetics.com/assets/4f1.pdf.

[19] (online) Available: www.mouser.com/catalog/specsheets/5967000201.pdf.

[20] D. S. Gardner, G. Schrom, P. Hazucha, F. Paillet, T. Karnik, S. Borkar, R. Hallstein, T. Dambrauskas, C. Hill, C. Linde, W. Worwag, R. Baresel, and S. Muthukumar, "Integrated on-chip inductors using magnetic material (invited)," *Journal of Applied Physics*, vol.103, pp.07E927-6, Apr. 2008.

[21] D. S. Gardner, G. Schrom, F. Paillet, B. Jamieson, T. Karnik, and S. Borkar, "Review of on-chip inductor structures with magnetic films," *IEEE Transactions on Magnetics*, vol. 45, no. 10, pp. 4760-4766, Oct. 2009.

[22] K. Ikeda, T. Suzuki, and T. Sato, "CoFeSiO/$SiO_2$ multilayer granular films with very narrow ferromagnetic resonant linewidth," *IEEE Transactions on Magnetics*, vol. 45, no. 10, pp. 4290-4293, Oct. 2009.

[23] T. Maruyama, Y. Obinata, M. Sonehara, K. Ikeda, and T. Sato, "Increase of Q-factor of RF magnetic thin film inductor by introducing slit-patterned magnetic thin film and multiline-conductor spiral coil," *IEEE Transactions on Magnetics*, vol. 47, no. 10, pp. 3196-3199, Oct. 2011.

[24] B. Orlando, R. Hida, R. Cuchet, M. Audoin, B. Viala, D. P-Tanon, X. Gagnard, and P. Ancey, "Low-resistance integrated toroidal inductor for power management," *IEEE Transactions on Magnetics*, vol. 42, no. 10, pp. 3374-3376, Oct. 2006.

[25] D. Flynn, A. Toon, L. Allen, R. Dhariwal, and M. P. Y. Desmulliez, "Characterization of core materials for microscale magnetic components operating in the megahertz frequency range," *IEEE Transactions on Magnetics*, vol. 43, no. 7, pp. 3171-3180, Jul. 2007.

[26] D. Flynn, R. S. Dhariwal, and M. P. Y. Desmulliez, "A design study of microscale magnetic components for operation in the MHz frequency range,"*Journal of Micromechanics and Microengineering*, vol. 16, no. 9, pp. 1811-1818, 2006.

[27] R. Meere, T. O'Donnell, H. J. Bergveld, N. Wang, and S. C. O'Mathuna, "Analysis of microinductor performance in a 20-100 MHz dc/dc converter," *IEEE Transactions on Power Electronics*, vol. 24, no.9 , pp. 2212-2218, Sep. 2009.

[28] J. Y. Park, "Packaging-compatible micromachined magnetic devices: Integrated passive components and modules," Ph.D. dissertation, Department of Electrical and Computer Engineering, Georgia Institute of Technology, Atlanta, GA, USA, Dec. 1997.

[29] W. P. Taylor, M. Schneider, H. Baltes, and M. G. Allen, "A NiFeMo electroplating bath for micromachined structures," *Electrochemical and Solid-State Letters*, vol. 2, no. 12, pp. 624-626, 1999.

[30] T. E. Mastouli, J. P. Laur, J. L. Sanchez, M. Brunet, D. Bourrier, and M. Dilhan, "Micro-inductors integrated on silicon for dc-dc converters," *Micromachining and Microfabrication Process Technology*, 68820A, Feb 2008.

[31] I. Sasada, T. Yamaguchi, K. Harada, Y. Notohara, "Planar inductors using NiZn ferrite thin plates and the application to high-frequency dc-dc converters," *IEEE Transactions on Magnetics*, vol. 29, no. 6, pp. 3231-3233, Nov 1993.

[32] J. C. Mallinson, "The foundations of magnetic recording," 2nd edition. London, U.K.: Academic Press, 1993. Ch. 5.

[33] C. H. Ahn, M. G. Allen, "A new toroidal-meander type integrated inductor with a multilevel meander magnetic core," *IEEE Transactions on Magnetics*, vol. 30, no. 1, pp. 73-79, Jan 1994.

[34] T. Osaka, M. Takai, K. Hayashi, K. Ohashi, M. Saito, and K. Yamada, "A soft magnetic CoNiFe film with high saturation magnetic flux density and low coercivity," *Nature Material*, vol. 392, pp. 796-798, Apr 1998.

[35] X. Liu, G. Zangari, and M. Shamsuzzoha, "Structural and magnetic characterization of electrodeposited, high moment FeCoNi films," *Journal of the Electrochemical Society*, vol. 150, no. 3, pp. C159-C168, 2003.

[36] T. Osaka, T. Sawaguchi, F. Mizutani. T. Yokoshima, M. Takai, and Y. Okinaka, "Effects of saccharin and thiourea on sulfur inclusion and coercivity of electroplated

soft magnetic CoNiFe film," *Journal of the Electrochemical Society*, vol. 146, no. 9, pp. 3295-3299, 1999.

[37] M. Kim, F. Herrault, J. Kim, and M. G. Allen, "Monolithically-fabricated laminated inductors with electrodeposited silver windings," *IEEE 26th International Conference on Micro Electro Mechanical Systems (MEMS)*, pp. 873-876, Jan. 2013.

[38] M. F. Gillier, R. Coehoorn, J. B. A. van Zon, and D. Alders, "Structure and soft magnetic properties of sputter deposited MnZn-ferrite films," *Journal of Applied Physics*, vol. 83, no. 11, pp. 6855-3857, Jun. 1998.

[39] N. Wang, T. O`Donnell, S. Roy, P. McCloskey, C. O`Mathuna, "Micro-inductors integrated on silicon for power supply on chip," *Journal of Magnetism and Magnetic Materials*, vol. 316, pp. e233-e237, 2007.

[40] D. W. Lee, K-. P. Hwang, and S. X. Wang, "Fabrication and analysis of high-performance integrated solenoid inductor with magnetic core," *IEEE Transactions on Magnetics*, vol. 44, no. 11, pp. 4089-4095, Nov. 2008.

[41] M. J. Prieto, A. M. Pernia, J. M. Lopera, J. A. Martin, and F. Nuno, "Design and analysis of thick-film integrated inductors for power converters," *IEEE Transactions on Industry Application*, vol. 38, no. 2, pp. 543-552, Mar/Apr. 2002.

[42] Z. Hayashi, Y. Katayama, M. Edo, H. Nishio, "High-efficiency DC-DC converter chip size module with integrated soft ferrite," *IEEE Transactions on Magnetics*, vol. 39, no. 5, pp. 3068-3072, Sep. 2003.

[43] A. M. Pernia, M. J. Prieto, J. M. Lopera, J. Reilly, S. S. Linton, and C. Quinones, "Thick-film hybrid technology for low-output-voltage DC/DC converter," *IEEE Transactions on Industry Application*, vol. 40, no. 1, pp. 86-93, Jan/Feb. 2004.

[44] T. Mikura, K. Nakahara, K. Ikeda, K. Furukuwa, and K. Onitsuka, "New substrate for micro DC-DC converter," *56$^{th}$ Electronic Components and Technology Conference*, 2006.

[45] M. H. Lim, J. D. Wyk, F. C. Lee, and K. D. T. Ngo, "A class of ceramic-based chip inductors for hybrid integration in power supplies," *IEEE Transactions on Power Electronics*, vol. 23, no. 3, pp. 1556-1564, May. 2008.

[46] M. Wang, J. Li, K. D. T. Ngo, and H. Xie, "A surface-mountable microfabricated power inductor in silicon for ultracompact power supplies," *IEEE Transactions on Power Electronics*, vol. 26, no.5, pp. 1310-1315, May. 2011.

[47] F. C. Lee, and Q. Li, "High-frequency integrated point-of-load converters: Overview," *IEEE Transactions on Power Electronics*, vol. 28, no. 9, pp. 4127-4136, Sep. 2013.

[48] S. Sugahara, K. Yamada, M. Edo, T. Sato, and K. Yamasawa, "90% high efficiency and 100-W/cm$^3$ high power density integrated DC-DC converter for cellular phones," *IEEE Transactions on Power Electronics*, vol. 28, no. 4, pp. 1994-2004, Apr. 2013.

[49] T. Sato, H. Tomita, A. Sawabe, T. Inoue, T. Mizoguchi, and M. Sahashi, "A magnetic thin film inductor and its application to a MHz switching DC-DC converter," *IEEE Transactions on Magnetics*, vol. 30, no. 2, pp. 217-223, Mar. 1994.

[50] Y. Katayama, S. Sugahara, H. Nakazawa, and M. Edo, "High-power-density MHz-switching monolithic DC-DC converter with thin-film inductor," *IEEE Power Electronics Specialists Conference*, 2000.

[51] S. Iyengar, T. M. Liakopoulos, and C. H. Ahn, "A DC/DC boost converter toward fully on-chip integration using new micromachined planar inductors," *IEEE Power Electronics Specialists Conference*, 1999.

[52] J-. W. Park, and M. G. Allen, "Ultralow-profile micromachined power inductors with highly laminated Ni/Fe cores: application to low-megahertz DC-DC converters," *IEEE Transactions on Magnetics*, vol. 39, no. 5, pp. 3184-3186, Sep. 2003.

[53] P. Galle, X. Wu, L. Milner, S-. H. Kim, P. Johnson, P. Smeys, P. Hopper, K. Hwang, M. G. Allen, "Ultra-compact power conversion based on a CMOS-compatible microfabricated power inductor with minimized core losses," *IEEE 57$^{th}$ Electronic Components and Technology Conference*, pp. 1889-1894, 2007.

[54] N. Wang, T. O'Donnell, R. Meer, F. M. F. Rhen, S. Roy, and S. C. O'Mathuna, "Thin-film-integrated power inductor on Si and its performance in an 8-MHz buck converter," *IEEE Transactions on Magnetics*, vol. 44, no. 11, pp. 4096-4099, Nov. 2008.

[55] C. Feeney, N. Wang, and S. C. O'Mathuna, "A 20-MHz 1.8-W DC-DC converter with parallel microinductors and improved light-load efficiency," *IEEE Transactions on Power Electronics*, vol. 30, no. 2, pp. 771-779, Jan. 2015.

[56] (online) Available: https://www.altera.com/content/dam/altera-www/global/en_US/pdfs/literature/ds/en5312qi_04535.pdf

[57] (online) Available: http://www.ti.com/lit/ds/symlink/lm3218.pdf

[58] (online) Available: http://cds.linear.com/docs/en/datasheet/8022fd.pdf

[59] (online) Available: http://www.micrel.com/_PDF/mic33050.pdf

[60] W. Zhang, M. A. Wilkowski, J. Weld, and A. Lotfi, " A 20MHz monolithic DC-DC converter manufactured with the first commercially viable silicon magnetics technology," *IEEE 7$^{th}$ International Power Electronics and Motion Control Conference,* June 2-5, 2012, Harbin, China.

[61] S. D. Leith, S. Ramli, and D. T. Schwartz, "Characterization of $Ni_xFe_{1-x}$ ($0.10<x<0.95$) electrodeposition from a family of surfamate-chloride electrolytes," *Journal of the Electrochemical Society*, vol. 146, pp. 1431-1435. 1999.

[62] J. Kim, M. Kim, P. Galle, F. Herrault, R. Shafer, J. Y. Park, and M. G. Allen, "Nanolaminated permalloy core for high-flux, high-frequency ultracompact power conversion," *IEEE Transactions on Power Electronics*, vol. 28, no.9, pp. 4376-4383, Sep. 2013.

[63] J. Kim, M. Kim, F. Herrault, J. Y. Park, and M. G. Allen, "Electrodeposited nanolaminated CoNiFe cores for ultracompact DC-DC power conversion," *IEEE Transactions on Power Electronics*, vol. 30, no. 9, pp. 5078-5087, Sep. 2015.

[64] (online) Available: http://multimedia.3m.com/mws/media/730273O/3mtm-novectm-1700-1702-electronic-grade-coating-guidelines.pdf

[65] (online) Available: http://youtu.be/y_NBPtj4TWY

[66] J. Berthier, and P. Silberzan, "Microfluidics for Biotechnology," Artech House, Norwood, 2009.

[67] Y. Han, G. Cheung, A. Li, C. R. Sullivan, and D. J. Perreault, "Evaluation of magnetic materials for very high frequency power applications," *in Proc. IEEE Power* Electronics Special Conference, pp. 4270–4276, Jun. 2008.

[68] C. P. Steinmetz, "On the law of hysteresis", *AIEE Transactions*, vol. 9, pp. 3–64, 1892.

[69] V. M. Machado and A. L. Ribeiro, "Eddy current hysteresis losses in ferromagnetic media," *IEEE Transactions on Magnetics*, vol. 34, no. 4, pp. 1267-1269, Jul 1998.

[70] G. Bertotti, F. Fiorillo and M. Pasquale, "Measurement and prediction of dynamic loop shapes and power losses in soft magnetic materials," *IEEE Transactions on Magnetics*, vol. 29, no. 6, pp. 2496-2498, Jul 1993

[71] J. Reinert, A. Brockmeyer, and R. W. DeDoncker, "Calculation of losses in ferro- and ferromagnetic materials based on the modified steinmetz equation," *IEEE Transactions on Industry Applications*, vol.37, no.4, pp.1055-1061, Jul/Aug 2001.

[72] Y. Chen, and P. Pillay, "An improved formula for lamination core loss calculations in machines operating with high frequency and high flux density excitation," *Industry Applications Conference, Record of the 37th IAS Annual Meeting*, vol.2, pp.759-766, Oct. 2002

[73] E. Dlala, "Comparison of models for estimating magnetic core losses in electrical machines using the finite-element method," *IEEE Transactions on Magnetics*, vol.45, no.2, pp.716-725, Feb 2009.

[74] J. Li, T. Abdallah, C. R. Sullivan, "Improved calculation of core loss with nonsinusoidal waveforms," *Industry Applications Conference, Thirty-Sixth IAS Annual Meeting. Conference Record of the 2001 IEEE,* vol.4, pp.2203-2210, Sep 2001.

[75] J. Muhlethaler, J. Biela, J.W.Kolar, and A. Ecklebe, "Improved core-loss calculation for magnetic components employed in power electronic systems," *IEEE Transactions on Power Electronics,* vol.27, no.2, pp.964-973, Feb 2012.

[76] (Online) Available: http://www.ferroxcube.com/FerroxcubeCorporateReception/datasheet/3f35.pdf

[77] (Online) Available: http://www.ferroxcube.com/FerroxcubeCorporateReception/datasheet/3f45.pdf

[78] (Online) Available: http://www.thierry-lequeu.fr/data/SIFERRIT.pdf

[79] [Online]. Available: http://product.tdk.com/en/catalog/datasheets/ferrite_mn-zn_material_characteristics_en.pdf

[80] (Online) Available: http://tdgcoreen.sx47.80data.net/upload/product/2.pdf

[81] (Online) Available: http://www.ti.com/lit/ds/symlink/lm3103.pdf

[82] D. Shin, C Kim, J. Jeong, S. Bae, S. Nam, and H. Kim, "Effect of magnetic anisotropy on the current capability of thin film inductor", *Journal of Applied Physics,* vol. 87, 5852, 2000.

[83] T. Masai, and Y. Kitamoto, "Effect of slit patterning perpendicular to magnetic easy axis in thin film inductors", *IEEE Transactions on Magnetics,* vol. 44, no.11, pp.3871-3874, Nov. 2008.

[84] (online) Available: http://www.ti.com/lit/ds/symlink/lm5116.pdf

[85] J. Kim, J-. k. Kim, M. Kim, F. Herrault, M. G. Allen, "Microfabrication of totoidal inductors integrated with nanolaminated ferromagnetic metallic cores," *Journal of Micromechnics and Microengineering,* vol. 23, no. 11, pp. 114006, Nov. 2013.

[86] C. J. Kaiser, "The inductor handbook," CJ Publishing, 1996.

[87] C. H. Ahn, Y. J. Kim, M. G. Allen, "A fully integrated planar toroidal inductor with a micromachined nickel-iron magnetic bar," *IEEE Transactions on Components, Packaging, and Manufacturing Technology*, vol. 17, no. 3, pp. 463-469, Sep. 1994.

[88] E. J. Brandon, E. Wesseling, V. White, C Ramsey, L. D. Castillo, U. Lieneweg, "Fabrication and characterization of microinductors for distributed power conversion," *IEEE Transactions on Magnetics,* vol. 39, no.4, pp. 2049-2056, Jul. 2003.

[89] J.-W. Park, F. Cross, and M. G. Allen, "Planar spiral inductors with multilayer micrometer-scale laminated cores for compact-packaging power converter applications", *IEEE Transactions on Magnetics*, vol. 40, no. 4, pp. 2020-2022, Jul. 2004.

[90] N. Wang, T. O`Donnell, S. Roy, M. Brunet, P. McCloskey, and S. C. O`Mathuna, "High-frequency micro-machined power inductors", *Journal of Magnetism and Magnetic Materials*, vol. 290, pp. 1347-1350, 2005.

[91] T. O`Donnell, N. Wang, R. Meere, f. Rhen, S. Roy, D. O`Sullivan, and S. C. O`Mathuna, "Microfabricated inductors for 20 MHz DC-DC converters", *Proceeding Of Applied Power Electronics Conference and Exposition*, pp. 689-693, Feb. 2008.

[92] M. Kim, F. Herrault, J. Kim and M. G. Allen, "Monolithically-fabricated laminated inductors with electrodeposited silver windings," *IEEE International Conference on Micro Electro Mechanical Systems (MEMS)*, pp. 873-876, Jan. 2013.

[93] S. Lim, J. Ranson, D. M. Otten, and D. J. Perreault, "Two-stage power conversion architectures suitable for wide range input voltage," *IEEE Transactions on Power Electronics*, vol. 30, no. 2, pp. 5078-5087, Feb. 2015.

[94] (online) Available: http://cds.linear.com/docs/en/datasheet/3630fd.pdf

[95] (online) Available: http://www.righto.com/2012/10/a-dozen-usb-chargers-in-lab-apple-is.html

[96] (online) Available: http://www.righto.com/2012/05/apple-iphone-charger-teardown-quality.html

[97] (online) Available: http://www.righto.com/2014/05/a-look-inside-ipad-chargers-pricey.html

[98] (online) Available: https://en.wikipedia.org/wiki/AC_adapter

[99] (online) Available: https://www.altera.com/products/power/devices/powersoc-dc-dc-step-down-converters.html

[100] (online) Available: http://www.vptpower.com/vpt-products/point-of-load-dc-dc-converters/dvpl0503s-point-of-load-dc-dc-converter/#.VX92w_lVhBc

[101] (online) Available: http://pdfserv.maximintegrated.com/en/an/AN296.pdf

[102] T. Yokoshima, M. Kaseda, M. Yamada, T. Nakanishi, T. Momma, and T. Osaka, "Increasing the resistivity of electrodeposited high $B_s$ CoNiFe thin film," *IEEE Transactions on Magnetics*, vol. 35, no. 5, pp. 2499-2501, Sep. 1999.

[103] M. Takai, K. Hayahi, M. Aoyagi, and T. Osaka, "Electrochemical preparation of soft magnetic CoNiFeS film with high saturation magnetic flux density and high

resistivity," *Journal of the Electrochemical Society*, vol. 144, no. 7, pp. L203-L204, 1997.

[104] J. M. Gere, "Mechanics of materials," 6th edition, Thomason Learning, Inc., 2004.

[105] P. Kasiraj, R. M. Shelby, J. S. Best, and D. E. Horne, "Magnetic domain imaging with a scanning Kerr effect microscope," *IEEE Transactions on Magnetics*, vol. MAG-22, no. 5, pp. 837-839, Sep. 1986.

[106] J. M. Wright, D. W. Lee, A. Mohan, A. Papou, P. Smeys, and S. X. Wang, "Analysis of integrated solenoid inductor with closed magnetic core," *IEEE Transactions on Magnetics*, vol. 46, no. 6, pp. 2387-2390, Jun. 2010.

[107] H. J. Mamin, D. Rugar, J. E. Stern, R. E. Fontana Jr., and P. Kasiraj, "Magnetic force microscopy of thin Permalloy films," *Applied Physics Letter*, vol. 55, no. 3, pp. 318-320, Jul. 1989.

[108] W. A. Roshen, "A practical, accurate and very general core loss model for nonsinusoidal waveforms," *IEEE Transactions on Power Electronics*, vol. 22, no. 1, pp. 30-40, jan. 2007.